

Die approbierte Originalversion dieser Dissertation ist an der Hauptbibliothek der Technischen Universität Wien aufgestellt (<http://www.ub.tuwien.ac.at>).

The approved original version of this thesis is available at the main library of the Vienna University of Technology (<http://www.ub.tuwien.ac.at/englweb/>).



DISSERTATION

Growth of Complex Oxides: Characterization of the Metal Flux during Magnetron Deposition with Special Emphasis on the Angular Distribution

ausgeführt zum Zwecke der Erlangung des akademischen Grades eines Doktors der technischen Wissenschaften unter der Leitung von

a.o. Univ. Prof. Dipl.-Ing Dr. techn. Christoph Eisenmenger-Sittner

E138

Institut für Festkörperphysik

eingereicht an der Technischen Universität Wien

Fakultät für Physik

von

Dipl. Ing. Maximilian Horkel

e0027314

Josefstädterstraße 11/33

A-1080 Wien

Wien, am

Kurzfassung

Das Verständnis des Schichtwachstums ist ein essentieller Schritt im Design komplexer funktioneller Beschichtungen. Um das Wachstum während der Abscheidung durch Magnetron-Sputtern zu verstehen, ist ein genaues Wissen über den Teilchenfluss von der Quelle zum Substrat von großer Bedeutung. Dies gilt insbesondere für anspruchsvolle Techniken, wie beispielsweise die simultane Beschichtung durch zwei oder mehrere Quellen in reaktiver Atmosphäre. Ein wichtiger Parameter ist die Winkelverteilung der auftreffenden neutralen Teilchen, da diese die Uniformität der Schicht bzw. Effekte wie Selbstabschattung beeinflusst. Weiters kann die Bestimmung der Winkelverteilung der Teilchen Aufschluss über wichtige Aspekte der Grundlagen der Beschichtung mittels Sputtern geben. Einerseits können die experimentellen Resultate mit Simulationen verglichen werden, um den Gültigkeitsbereich der verwendeten Modelle richtig abzustechen. Andererseits können wichtige Parameter, wie beispielsweise die Winkelverteilung der von der Quelle emittierten Teilchen, dadurch bestimmt werden.

Die Bestimmung der Winkelverteilung der auftreffenden Teilchen an einem bestimmten Punkt in der Beschichtungskammer erfolgt mittels einer Lochkamera, welche die Winkelverteilung in eine Dickenverteilung umwandelt. Diese Arbeit beschreibt die Konstruktion solch einer Lochkamera, welche dazu in der Lage ist, die Winkelverteilung einer großen Anzahl von Materialien zu bestimmen, und welche einfach in die Beschichtungskammer eingebracht werden kann. Im Falle einer nicht reaktiven Beschichtung wurde die Winkelverteilung für unterschiedliche Materialien (Cu, W, Al, Ti, Mg), Geometrien (planar, zylindrisch, rotierbar) bei unterschiedlichen Parametern (Druck, laterale und vertikale Position) im Experiment bestimmt und mit Simulationen eines vor kurzem entwickelten Monte Carlo Algorithmus verglichen. Es wurde ebenfalls untersucht, ob Parameter, welche von der Winkelverteilung abgeleitet werden können, mit energieabhängigen Parametern oder mit der Winkelverteilung der emittierten Teilchen in Beziehung stehen. Auch der Einfluss eines reaktiven Gases wie z.B. Sauerstoff auf die Winkelverteilung für verschiedene Materialien und Geometrien wurde untersucht. Es stellte sich dabei heraus, dass die Zugabe eines reaktiven Gases sowohl einen Einfluss auf die Winkelverteilung der emittierten Teilchen als auch auf den Gasphasentransport der neutralen Teilchen hat.

Abstract

To understand the film growth during magnetron sputter deposition, especially for more demanding deposition techniques like reactive co-sputtering from two sources, a detailed knowledge of the flux of sputtered species from the target towards the substrate is vital. One important parameter is the angular distribution of the impinging neutral target atoms on the substrate, since it is responsible for e.g. self shadowing effects or film thickness uniformity. Additionally, the determination of the angular distribution of the metal flux can provide insight into the fundamental principles of sputter deposition. On the one hand the experimentally obtained results can be compared with simulations, thus proving whether the used models are valid or not. On the other hand, important parameters like the nascent angular distribution of the sputtered particles can be derived directly from the angular distribution of the arriving flux.

The determination of the angular distribution of the metal flux at an arbitrary point in the deposition chamber is achieved by a pinhole-camera, where the information of the angular distribution is converted into a thickness profile. This thesis describes the construction of such a pinhole-camera which is capable to determine the angular distribution for a wide variety of target materials, and which can easily be inserted into a deposition chamber. In the case of non-reactive sputtering, angular distributions of different materials (Cu; W; Al; Ti; Mg), different target geometries (planar, cylindrical, rotatable) at different parameters (pressure, lateral position, and vertical position) are experimentally determined and compared to simulations obtained from a newly developed Monte Carlo code. It was also investigated, if parameters derived from the angular distribution are related to energy related parameters of the impinging particles, or to the nascent angular distribution. Also, the influence of a reactant like oxygen on the angular distribution of the arriving flux was investigated for different materials and target geometries. It was found that the addition of the reactive gas has an impact on both, the nascent angular distribution of sputtered particles as well as on the transport of the neutral metal atoms through the gas phase.

Contents

1 Introduction	6
2 Fundamentals	14
2.1 Sputtering	14
2.1.1 Plasma surface interactions in a magnetron sputter source	15
2.1.2 Gas phase transport	21
2.2 Reactive Sputtering	31
3 Metal Flux Monitor	37
3.1 Corrections and limitations	41
3.1.1 Vignetting	41
3.1.2 Angular error	42
3.1.3 Angle dependant sticking probability	43
3.1.4 Gas phase scattering inside the MFM and the reduction of the deposition rate	43
3.2 Conversion of the thickness profile to the angular distribution	47
3.3 Thickness Determination	49
3.3.1 Metallic Layers	49
3.3.1.1 Experimental procedure	50
3.3.2 Dielectric Layers	51
3.3.2.1 Theoretical model	52
3.3.2.2. Original procedure to determine the thickness profile of a dielectric layer	55
3.3.2.3 Refined setup	64
4 Simulation of the angular distribution	68
4.1 MC Simulation SIMTRA	69
4.2 Analytical/numerical simulation	71
4.2.1 Geometric considerations	71
4.2.2 Analytical simulation of the angular distribution for basic target geometries	72
4.2.3 Numerical approach	76
5 Experimental Setup	82
5.1 Deposition chambers	82

5.1.1 LAB I	84
5.1.2 LAB II	84
5.1.3 LAB III	85
5.2 Magnetron types	86
6 Results and Discussion	88
6.1 Systematical investigation of the angular distribution of the metal flux during non reactive sputtering	89
6.1.1 100 mm planar magnetron	89
6.1.2 2" Magnetron	96
6.1.3 Cylindrical Magnetron	99
6.1.4 Rotatable Magnetron	104
6.2 Influence of a reactive atmosphere on the angular distribution of the metal flux	108
7 Conclusion and Outlook	127
References	129
Acknowledgements	132
Appendix	133
Technical Drawings	136
List of experiments	142
Bibliography	154
Curriculum Vitae	156

1 Introduction

Multi component oxides, so called complex oxides are a topic of intense research in the last years. Because of their fascinating properties and wide tunable range of conductivity (superconductors, conductors, semi conductors, and insulators) they can be applied as thin films in several devices as ferroelectric, piezoelectric, magnetic, optical, infrared, data storage and microwave devices. There are several deposition techniques used to deposit these interesting films. One of them is magnetron sputter deposition, a physical vapor deposition method for fabricating thin films. It has the advantages, that it is easy controllable, widely used and, due to the existence of large targets, it has a great potential for up scaling. For conductive complex oxides like TCO's, large sintered multi component targets are available and the films can be deposited by dc reactive sputtering.

A different approach is to deposit complex oxides from different single element targets via reactive dc magnetron deposition. This approach would give better control over the film properties like microstructure, stoichiometry and crystallographic orientation. However, this is a very difficult task, due to the high complexity of the deposition process. All the relevant parameters are interrelated which makes it very difficult to forecast the film properties. Because of this, research generally focuses only on specific aspects of the deposition process. As such, the conducted research is limited and the results are only applicable in a narrow parameter range. This has the disadvantage that the experience from the deposition process of one type of complex oxides is only applicable in a limited way for the deposition process of another type of complex oxide.

Therefore, a global approach is advisable. It should map all the relevant parameters involved in the deposition of complex oxides, from the sputtering process itself to the growth of the film with the desired microstructure. Since this task would be overwhelming for a single research group or company, the project "Growth of complex oxides" was started under the lead of the group DRAFT of the Ghent University. This group has a great expertise in reactive sputter deposition, and recently investigated the deposition of biaxially aligned oxides [1-4]. Biaxially aligned films have both, an out of plane and an in plane alignment of the crystallites. For small misorientation angles (below 15°) these polycrystalline films have the same

interesting properties of a single crystal. For the deposition of these biaxially aligned films, a full characterization of the deposition process is needed.

The aim of the project is to combine the knowledge and expertise of several Flemish research groups, reinforced with the expertise of non-Flemish groups, if needed, to master the controlled deposition and complete characterization of complex oxides. This will be done by mapping as much as possible parameters and by simulating/modeling the deposition process in all its aspects. The vision is to know the influence of the deposition parameters on the film properties and thus to prevent the trial and error approach for the deposition of complex oxides in the future. As mentioned above, this approach allows a more flexible deposition method, namely reactive magnetron co-deposition. In fact, it has several advantages in comparison to using a multi component target. Single material targets are more economical than multi component targets and the use of two targets gives a better control over the properties of the deposited layer, e.g. the stoichiometry or micro-structure, as the stoichiometry of the thin film deposited from a multi component target is predetermined by the stoichiometry of the target. Furthermore, the use of a reactive gas with a metallic target to deposit the wanted oxidic film circumvents the problem of oxidic targets.

The final goal of the project “growth of complex oxides” is the controlled deposition of complex oxides via reactive co-sputter deposition. Controlled deposition means control over the microstructure, the crystallographic orientation, and the stoichiometry of the deposited layer. There are several examples illustrating the influence of this microstructure on the properties of complex oxide films.

- The properties of a photovoltaic cell improve when these photovoltaic films are deposited on a TiO_x buffer layer which consists of tilted columns. The higher the column tilt, the better the photovoltaic properties [5].
- The transmission for optical wavelengths of $\text{In}_x\text{Zn}_y\text{O}_z$ depends on the microstructure and surface morphology [6].
- Optical properties of $\text{Mg}_x\text{Al}_y\text{O}_z$ depend on the microstructure [7].
- The grain size influences the electrical properties (the charge carrier density and the Hall mobility) of $\text{Zn}_x\text{Al}_y\text{O}_z$ [8].
- The catalytic properties of ZnAl_2O_4 improve with increasing porosity [9].

- The barrier properties of TiN depend on the microstructure [10].

Also very illustrative are the following references which report the effect of the crystallographic orientation on some thin film properties:

- Pyroelectric properties of $\text{PbZr}_x\text{Ti}_{1-x}\text{O}_3$ ($0 < x < 0.7$) depend on the out-of-plane orientation and are best for (111) out-of-plane orientation because this results in the highest possible degree of polarization perpendicular to the substrate [11].
- In developing plasma display panels, MgO is an important material. Secondary electron emission is higher for MgO (111) than MgO (100) and MgO (110) [12]. Also the resistance against ion bombardment depends on the crystallographic orientation, i.e. MgO (111) has the highest resistance.
- The degree of crystallinity effects the microwave dielectric properties of ZrTiO_4 [13].
- The barrier properties of TiN depend on the out-of-plane orientation and are the best for (111) out-of-plane oriented films [10].
- The hardness of (111) out-of-plane oriented TiN is higher than the hardness of other out-of-plane oriented TiN films [14].
- The elastic modulus of TiN (100) is higher than the elastic modulus of TiN (111) [15].

Very important is also the control over the stoichiometry and therefore the homogeneity in the deposition rate of the various materials, as there are several examples for the influence of the stoichiometry on the properties of the deposited complex oxide films:

- The bandgap of $\text{Zn}_{1-x}\text{Mg}_x\text{O}_y$ and $\text{Y}_x\text{Al}_y\text{O}_3$ depends on x [12] and on Y/Al ratio [16] respectively.
- The transparency and the conductivity of $\text{Cu}_x\text{Al}_y\text{O}_z$ depend on the Cu/Al ration [17].
- Optical properties of $\text{Mg}_x\text{Al}_y\text{O}_z$ depend on the stoichiometry [18].

Of course, the knowledge gained in this project is not only limited to the deposition of complex oxides. Due to its global approach, the gathered information will also be valuable of other, simple or complex, materials.

To achieve this goal a deep and comprehensive knowledge of the process in all relevant areas is necessary. Therefore, and because of its global approach, the project was split in several work packages. These work packages and their titles are:

WP1: METAL FLUX; The metallic flux towards the substrate: characterization, simulation, and optimization.

WP2: REACT; Characterization and simulation of the reactive sputtering process.

WP3: PLASMA; Interaction plasma-target and plasma substrate.

WP4: GROWTH; Deposition of the biaxially aligned complex oxide films.

WP5: SIMULATION; Simulation of the growth process.

WP6: PROPERTIES; Relationship between film characteristics and selected properties of the complex oxide films.

WP7: VALORISATION; Coordination and valorization of the achieved results.

As indicated in *figure 1.1*, these work packages (for WP1 to WP6) follow the logical way in the deposition process from the target up to the correlation of film growth to film properties.

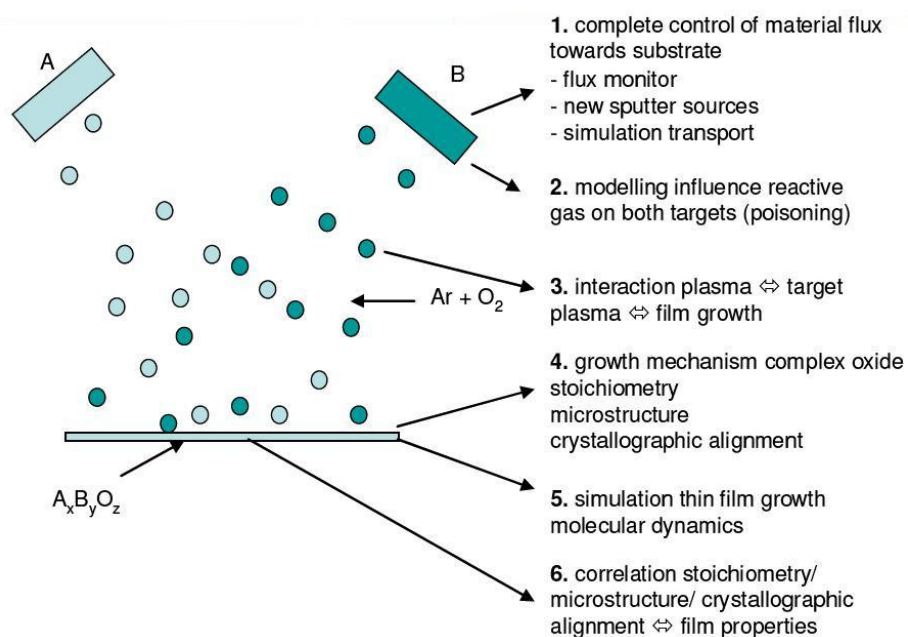


Figure 1.1 Overview of the reactive co-sputtering process and the areas of interest of the different work packages.

The scientific work described in this thesis is located in WP1: METAL FLUX. Since the metallic fluxes from different magnetrons have a distinct impact on the film properties (stoichiometry of the complex oxide, energy flux towards the oxide, microstructure and crystalline orientation of the film) this work package plays a key role in this project. Every attempt to simulate the growth of such complex structures is futile, when the properties of the impinging particles are unknown.

This work package itself is subdivided into three tasks. The first task is the experimental characterization of the properties of the impinging particles. Several properties were investigated. The energy and the momentum flux towards the target, and the angular distribution of the impinging metal flux, which will be the main topic of this thesis. The second task is the simulation of the metal flux arriving at the substrate. A Monte Carlo (MC) code was developed to simulate the metal flux. The simulated results are verified by the experimental results of the measurements of the angular distribution. Also, an accurate simulation of the metal flux will be beneficial for the other work packages. The third and last task, optimization, will be the development of a new sputter source with a low angular spread. This is important, since a low angular spread is essential for the deposition of biaxially aligned layers [19].

All the tasks of WP1 mentioned above will be conducted at the research group DRAFT of the Ghent University , except the experimental determination of the angular distribution of the incoming metal flux, which will be conducted at the “Thin Film Group” at the Vienna University of Technology, which besides is the only non-Belgian research group involved in this project. This group was assigned with this task, as it has already developed a flux monitor which enables the measurement of the angular distribution of the incoming particles in the past [20, 21].

In general, this work package has a special emphasis on the angular distribution of the metal flux for several reasons. First, the angular distribution has a general influence on the micro-structure of the deposited film, which is qualitatively summarized by the well known structure zone diagram by Thornton [22] (*figure 1.2*). Structure formation is caused by known effects like self shadowing [23, 24], or mound formation [25]. For deposition techniques with an incidence angle close to 90° relative to the substrate surface like glancing angle deposition [26], or the formation

of biaxially aligned complex oxide films [3], not only the mean incidence angle is of importance, but also the angular spread of the impinging particles.

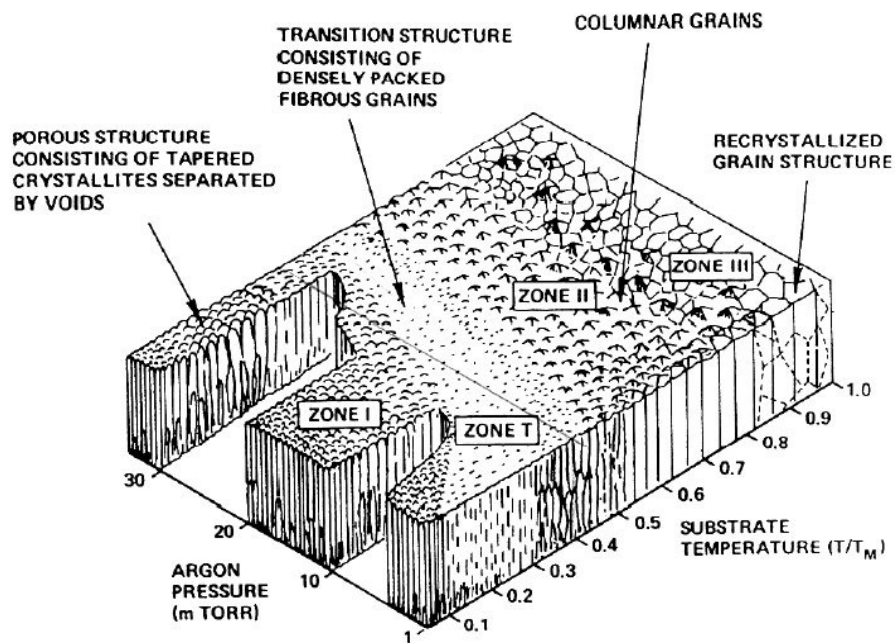


Figure 1.2 Structure zone diagram by Thornton [22]

Second, a detailed study of the angular distribution can provide insight into the fundamental principles of magnetron sputter deposition, such as the nascent angular distribution of the sputtered particles, the shape of the local sputter rate and transport of the sputtered particles through the gas phase as these all influence the angular distribution. In this context, a key aspect of magnetron sputter deposition is the energy of the particles arriving at the substrate which may be substantially higher than thermal energy. Of course this later has its impact on thin film growth [1, 3], and hence the degree of thermalization of the arriving flux is an important issue. The degree of thermalization is the percentage of the particles which have lost their initial kinetic energy due to collisions with the background gas, compared to the total amount of particles. As the angular distribution is influenced, together with the energy of the particles, by the gas transport, measurements of the angular distribution can give insight in the thermalization process.

A third aspect is that it is a more complex task for a simulation to reproduce the angular distribution of the impinging particles, as this distribution is heavily influenced by gas phase scattering. Therefore a sophisticated model of gas phase scattering and its relevant parameters like the interaction potential of the colliding species is necessary in the simulation for a correct and accurate reproduction of the

experimental results. Therefore the results can be used to check if the assumptions made in the simulation code were correct.

To measure the angular distribution of the impinging particles, a device called Metal Flux Monitor (MFM) has been constructed. It is a pinhole camera [20, 21, 27-30], which converts the angular distribution of the arriving flux into a thickness profile of a layer on a substrate behind the pinhole. This information can briefly be described as an image of the local sputter rate folded by the nascent angular distribution, which is then blurred by gas phase scattering. One difference of the MFM to the pinhole cameras described in previous papers [20, 21] is that it can be inserted via a load lock system and is not fixedly mounted in the deposition chamber. This allows a swift change of the position of the MFM, and a high experimental throughput. In fact, this was another goal of the work package 1, to design a ready to use plug in tool for the PVD industry, since this MFM is not restricted to sputter deposition only, but can be used for every vacuum deposition process. The methods to analyze the thickness profiles were also designed in respect to the high experimental throughput and allow a large variety of materials (not only metallic but also transparent materials) to be measured. While the method to measure the thickness profile of a metallic layer (via absorption) was well established, a new method to measure the profile of transparent layers needed to be developed, as all the established methods would lack lateral resolution, or be otherwise too expensive or time consuming. This novel method, based on optical interferometry, can be seen as a spin off of this work package, as its utilization is not restricted to this project and its simplicity and cost effectiveness may be valuable for other applications, either scientific or economic.

The conducted experiments can be classified as follows:

- 1: The systematical investigation of the angular distribution of the metal flux of dc-magnetron sputter deposition under pure Ar atmosphere. These experiments were performed for various target materials (Cu; W; Al; Mg; Ti), and target geometries (10 cm planar target, 2" planar target, cylindrical target, rotatable target) at different parameters (lateral position; distance magnetron-MFM; pressure). The results were compared to simulations by the Monte Carlo (MC) code SIMTRA [31] to give a better understanding of the sputtering process. It was also checked if some physical parameters (degree of thermalization or nascent angular distribution) could be derived from the results.

2: The investigation of the influence of a reactive gas addition on the angular distribution. These experiments were conducted for selected parameters (target geometry, materials etc.). These experiments were of great interest, since the reactive sputtering process is of growing importance, but not well understood.

2 Fundamentals

2.1 Sputtering

Magnetron sputtering is one of the important Physical Vapor Deposition (PVD) processes. It is widely used in industry due its versatility and its potential for up-scaling. It is used for coating of architectural glass (e.g. thermal management), in optics (e.g. antireflection coating), microelectronics (e.g. interconnects), production of solar cells, tribological coatings, magnetic storage media and many other applications.

Sputtering has several advantages. The substrate can be kept at a low temperature during the deposition process, which is an advantage when compared to a CVD process, where the substrate has to be at high temperatures to trigger the chemical reactions [32]. A large variety of materials can be used for deposition, e.g. conductors, insulators (with RF or pulsed DC sputtering) and compound materials. The sputtered particles reach the substrate usually at a higher than thermal energy, which is in most cases advantageous for the film properties, like adhesion. Finally, magnetron sputtering is an easy controllable process.

In a brief overview the sputter deposition process can be described as follows (see *figure 2.1*). In an inert gas atmosphere (typically 0.1 to 10 Pa of Argon) an electric discharge (in this case a glow discharge) is ignited in the region adjacent to the material that should be deposited, called the target. The target itself is on a negative potential, therefore the cathode, while the rest of the chamber is on ground potential. The substrate is located opposite to the target and usually also on ground potential, but it can also be biased to modify the properties of the growing film. In the plasma in front of the target that is caused by the discharge, Ar ions are produced and accelerated towards the target within the cathode fall. At their impact, atoms and positively charged ions are ejected from the target because of momentum transfer. While the ions are caught by the cathode fall, the neutral particles travel through the plasma and the background gas, where they might be subjected to collision processes. When they hit a chamber wall or the substrate these particles will condensate and a film will form.

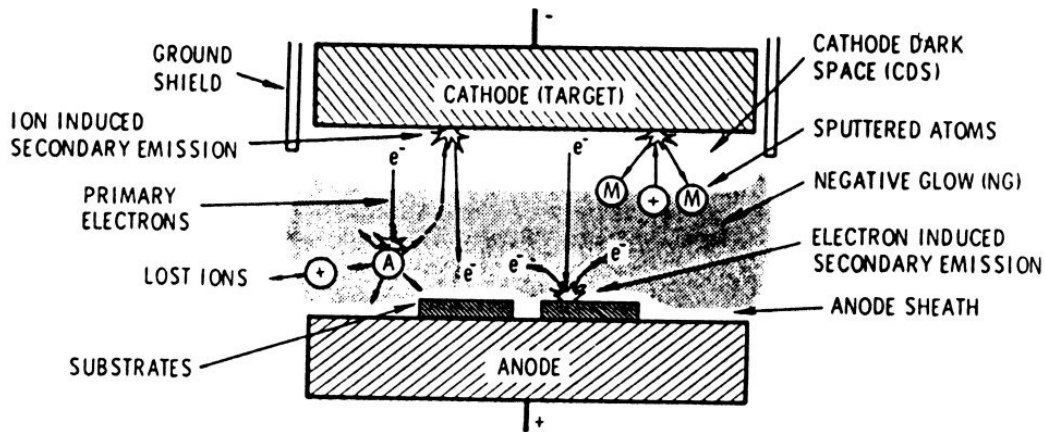


Figure 2.1 Schematic of a diode dc sputter process [32].

2.1.1 Plasma surface interactions in a magnetron sputter source

In a magnetron sputter source, the density of the charge carriers in the plasma is increased due to a magnetic field generated by permanent magnets located behind the target (see figure 2.2a). This arrangement allows sputtering at lower gas pressures, compared to the classic diode sputtering design. While the electrons are forced to cyclotron movement paths, and therefore are magnetically confined, the positive Ar ions, produced by collision events in the plasma, are accelerated in the cathode fall towards the target. Due to their high mass, compared to the electrons, they “ignore” the magnetic field.

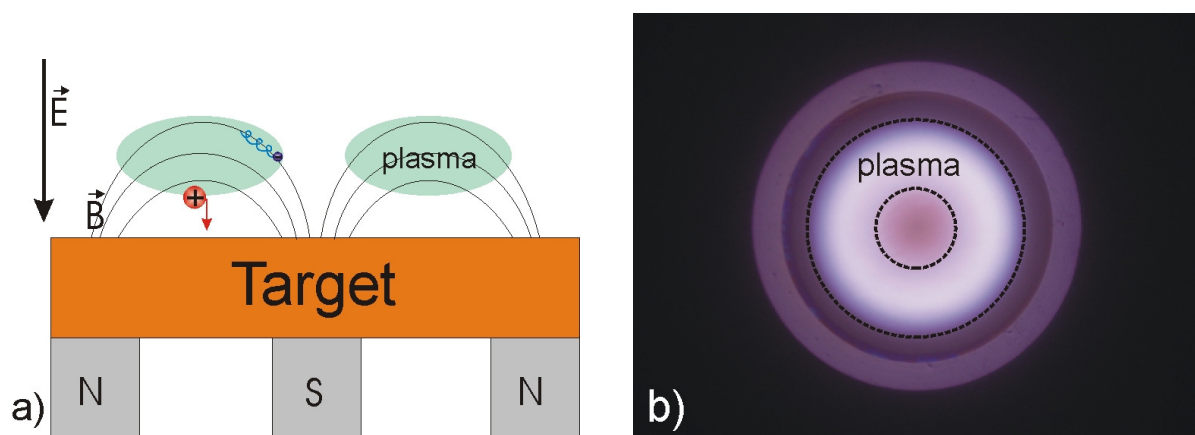


Figure 2.2 a) Schematic of a magnetron sputter source. b) Top view on the plasma of a cylindrically shaped planar magnetron (bright areas correspond to high plasma density). Because of the annular shape of the plasma it is often referred to as the “race-track” of the electrons.

The energy distribution (figure 2.3a) and the angular distribution (figure 2.3b) of the incident ions have been simulated by a MC code [33]. It is obvious, that most ions

reach the surface without any collisions, therefore a distinct peak at the discharge voltage and at 0° impact angle is observed.

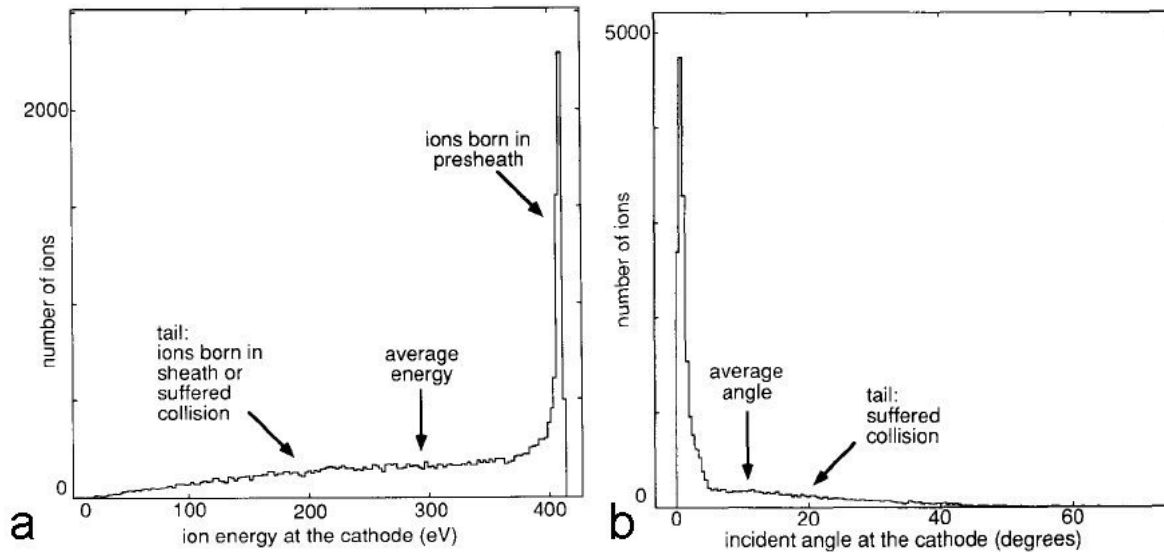


Figure 2.3 a) Energy distribution of ion impact at the cathode. A large fraction of the ions are born in the sheath or lose energy in a collision; these strike the cathode with less than the maximum energy. The mean impact energy is 293.02 ± 1.34 eV for a cathode bias of -400 V. [33]

b) Angular distribution of ion impact at the cathode. Most of the ions strike almost perpendicular to the cathode surface. The mean impact angle, defined with respect to the surface normal, is $7.95^\circ \pm 0.14'$.

At the impact of the ions, secondary electrons and target atoms are ejected from the surface. The secondary electrons contribute as charge carriers and are therefore necessary to sustain the plasma. Each impinging ion is ejecting Y neutral target atoms in average. Y is called the sputtering yield and it is one of the advantages of sputtering, that this sputtering yield (sputtered atoms per impinging ion) Y is only varying by an order of magnitude for all elements [32]. A part of the incident ions may also be neutralized and reflected at the surface and are contributing to the energy flux towards the substrate [34-36]

Important for the angular distribution at the substrate is the distribution of the local sputter rate

$$S(R) \propto J_i(R) \cdot Y \quad \text{Eq. 2.1}$$

where $J_i(R)$ is the local ion flux, Y is the sputter yield and R is the position on the target. For magnetron sputtering $J_i(R)$ is inhomogeneous, as the magnetic field above the target is inhomogeneous. For a cylindrically shaped planar magnetron $J_i(R)$ is

radial symmetric (see *figure 2.2b*). The sputter yield is influenced by the ratio of the masses of the ion and the target material, and is highest when they match. This is the reason why Ar is often used as working gas. $Y(E_0)$ increases linearly with the Energy of the impinging ion at low energies.

One way to estimate the distribution of the local sputter rate is to calculate $J_i(R)$ [37, 38]. Another approach is to measure the erosion profile $E(R)$ (*figure 2.4*) of a worn target, since the sputter rate and the erosion rate are closely related to each other. $E(R)$ can also be described as the probability that a particle will be ejected from this part of the target.

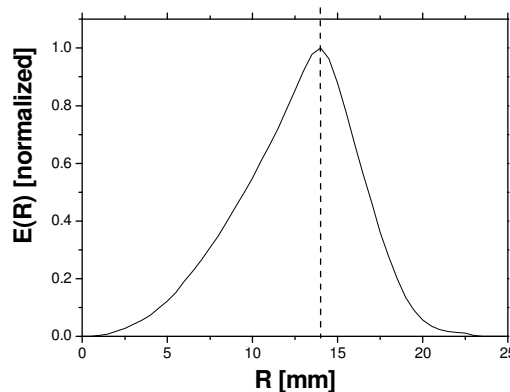


Figure 2.4 Distribution of the erosion rate (normalized to 1) of a planar target with a radius of 25 mm. The maximum of the racetrack is at 14 mm (indicated by the dashed line).

Another important influence on the angular distribution of the particles at the substrate is given by the nascent angular distribution of the ejected particles. The collision cascade theory predicts an isotropic distribution of the recoil atoms from a well developed collision cascade in a solid, and therefore a cosine shaped angular distribution of the sputtered particles is expected, when the target is bombarded by high energy particles with a normal incidence angle [39-45]. However, a lot of experimental data and simulations indicate, that the angular distribution is highly affected by the energy of the incident particle [31, 39-45]. Different types of angular distributions are presented in *figure 2.5a*.

At a higher projectile energy (typically above 1 keV) a so called over cosine shape of the nascent angular distribution can be observed. It can be best represented [41] by $\cos^n(\theta)$ where n is a fitting parameter and θ is the ejection angle. At low energies, however, this representation may become disadvantageous, as it is not able to

describe the so-called heart shaped angular distribution at low energies. The angular distribution at low angles is caused by a not fully developed collision cascade, which causes the atoms to be ejected preferably at higher angles and not perpendicular to the target surface. The following equation [46] is better suited to describe the angular distribution at low energies:

$$Y(E, \theta) \propto \cos \theta (1 + \beta \cos^2 \theta) \quad \text{Eq. 2.2}$$

where $Y(E, \theta)$ is the differential angular dependent sputter yield and β is a fitting parameter which can be approximated by

$$\beta = B \ln \left(\frac{m_t E_0}{m_g U_s} \right) - B_c \quad \text{Eq. 2.3}$$

with U_s as the surface binding energy. For Ar^+ on Cu at 100, 600, 1000, 5000 eV, they obtained the best-fit β values of -0.611, 0.284, 0.603 and 1.25, respectively. The values of B and B_c , were respectively approximated as 0.488 and 2.44. These values are in most cases independent of the target material (46, 47). The results of Eq. 2.3 have a good match to simulations performed by TRIM (TRansport of Ions in Matter), SRIM (Stopping Range of Ions in Matter) or ACAT GAS [48] and experiments where a well defined ion beam is targeted onto a smooth surface. A more detailed equation for the calculation of the energy dependent angular distribution of the sputtered atoms for low energy incidence ions is given by Zhang *et al.* [49].

However, the target of a magnetron sputtering source is considerably roughened; therefore deviations from the simulated to the experimentally obtained angular distributions [31] may occur, as shown in *figure 2.5b*.

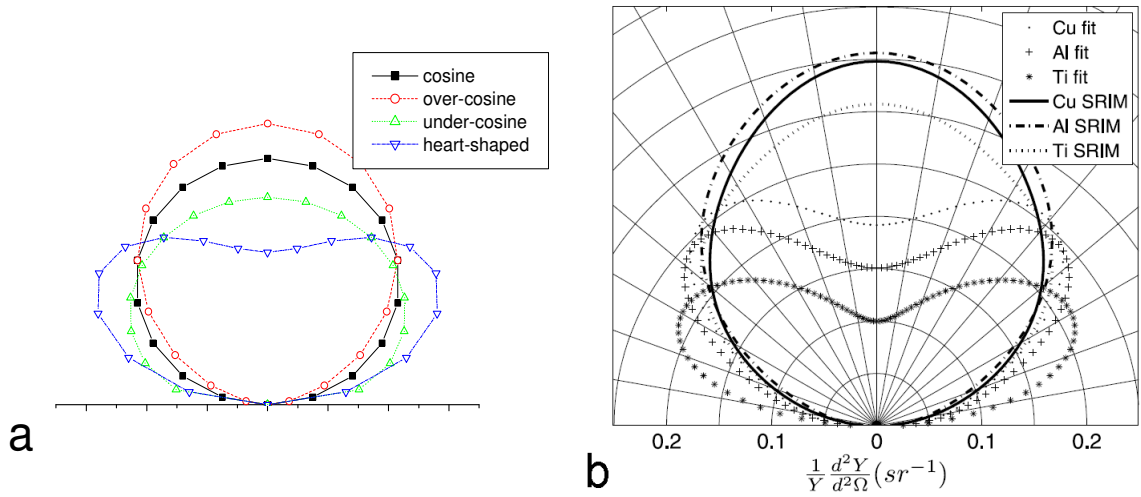


Figure 2.5 a) different types of nascent angular distributions; b) deviation of simulated and experimentally assessed nascent angular distribution obtained for magnetron sputtering

The energy distribution of the sputtered particles leaving the target has no direct geometric connection with the angular distribution of the metallic flux at the substrate. Nonetheless it is important, since the energy of the particles affects their gas scattering behavior. The energy distribution is well described by collision cascade theory and can be reproduced the Thompson formula [50]

$$f(E) = \frac{E}{(E + U_s)^3} dE \quad \text{Eq. 2.4}$$

where U_s is the surface binding energy. The energy distribution peaks at $U_s/2$ and has a high energy tail. The average energy $\langle E_{av} \rangle$ is

$$\langle E_{av} \rangle = \int_0^{E_{max}} f(E) E dE / \int_0^{E_{max}} f(E) dE \quad \text{Eq. 2.5}$$

with E_{max} being the maximum transferred energy given by [51]

$$E_{max} = k\Gamma E_o - U_s, \quad \Gamma = \frac{4m_s m_g}{(m_s + m_g)^2}. \quad \text{Eq. 2.6}$$

where m_s and m_g are the masses of the sputtered material and the incidence gas ion, respectively. The factor k in Eq. 2.6 accounts for the fact that for normal incidence of the impact atom no ejected particle can be sputtered by a head-on collision directly without further collisions. According to the results of Eckstein [51] this factor can be set to 0.4. The typical average energy for sputtered particles is about 10 eV. One interesting aspect of the Thompson formula is that the energy distribution is mainly

affected by the surface binding energy U_s , while the incidence ion energy E_0 has only a minor effect. Deviations from the Thompson formula have been observed for incident energies below 1 keV for lighter ions [52-60]. The peak shifts to lower energies, the width of the spectrum becomes narrower and a steeper fall-off of the high energy tail can be observed (*figure 2.6*). This can also be attributed to a collision cascade which is not fully developed [61].

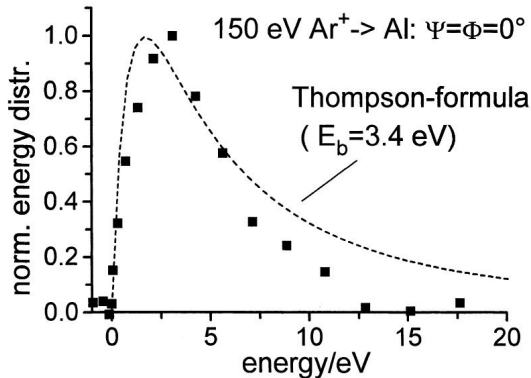


Fig. 2.6 Energy distribution of sputtered aluminum atoms at 150 eV (normal incidence). For comparison the Thompson formula is shown (dashed line) [61].

The Thompson formula (Eq. 2.3) predicts an isotropic dependence of the energy distribution of the ejected atoms, i.e. that the energy distribution is independent from the ejection angle. However, simulations with ACAT [48] and TRIM [61] showed that the energy distribution is affected by the ejection angle. In general, particles ejected perpendicular to the surface have a smaller energy than particles ejected at shallow angles, because the number of necessary collisions increases with the angle between incidence direction and ejection direction, and the angle between a particle ejected perpendicular to the surface and the incidence particle is 180° and thus the largest possible. Since this effect is again caused by a not fully developed collision cascade, the effect gets more pronounced when the incidence energy decreases (*figure 2.7 a, b*)

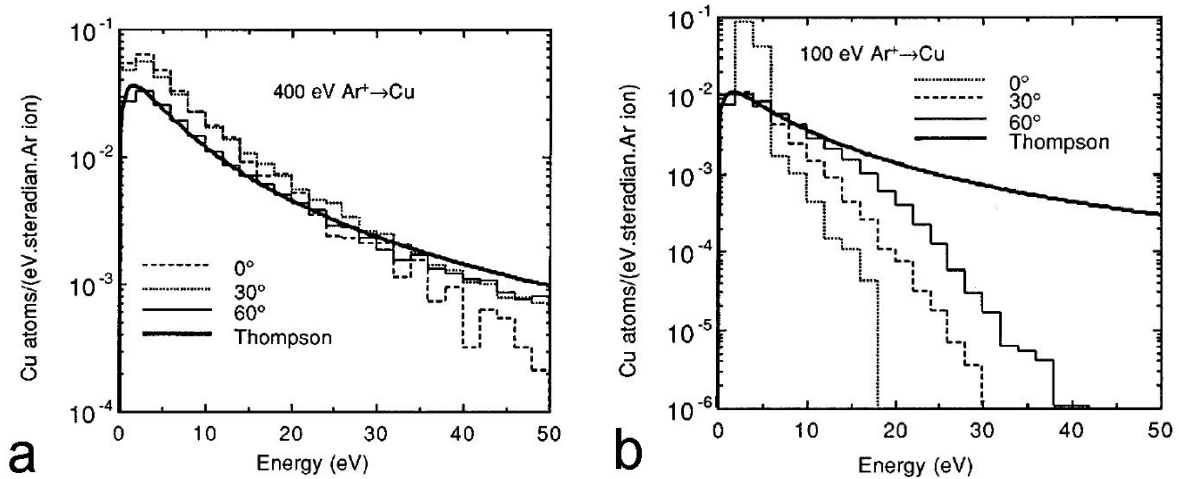


Fig 2.7 The differential sputtering yield for Ar^+ on Cu, where the energy spectra of sputtered atoms are plotted for ejection angles 0° , 30° , and 60° : a) $E_0 = 400\text{eV}$; b) $E_0 = 100\text{eV}$ [48]

2.1.2 Gas phase transport

During the transport from the target to the substrate, the sputtered particles are subjected to collisions with neutral atoms of the working gas. Collisions with ions, sputtered particles or high energy reflected gas neutrals may also occur, but due to their low density compared to the density of the working gas, these effects can be considered to be negligible [31].

By the collisions of the sputtered particles with the gas atoms, which have just thermal energies, the sputtered particles lose a part of their kinetic energy and are scattered. There are a lot of publications concerning the energy loss of the sputtered particles during gas phase transport [31, 47, 49, 62-67]. For this thesis, which studies the angular distribution of the arriving flux, the gas phase transport and the related energy loss is also of great interest, because this loss of energy and the angular distribution have a strong relation. When the particles suffered no collision, they have their initial angular distribution. As the number of collisions increases, they lose their energy and, in the same instance, the angular distribution morphs from the initial distribution to an isotropic distribution.

In general, three regimes for the gas phase transport can be considered [66-68], which are characterized by the pressure distance product pd , with p being the working gas pressure and d being the target substrate distance.

For the high pressure regime, where $pd > 50$ mTorr cm (≈ 6.7 Pa cm), the sputtered particles undergo a large number of collisions. The particles arriving at the substrate will have a near isotropic angular distribution. Their energy distribution is close to the Maxwellian energy distribution of the working gas. They have therefore lost most of their initial properties and therefore all the information of the sputter process at the target. Furthermore, the properties of the arriving particles provide no information of the scattering process, due to the high number of collisions which has randomized the scattering effects. Particles that have suffered so many collisions, that they have lost their initial energy are called “thermalized” as their energy is comparable to that of the working gas. They diffuse randomly in the gas.

In the low pressure regime, where $pd < 5$ mTorr cm (≈ 0.67 Pa cm), the number of collisions that occur are negligible. The particles arriving at the substrate therefore mostly keep their initial properties. Here, the geometry of the sputtering system also has an important effect on the arriving flux.

In the intermediate regime, where $5 < pd < 50$ mTorr cm, which is usually the case for typical magnetron sputtering processes, a small number of collisions occur on the transport between target and substrate. The distribution of the arriving flux significantly changes from the initial distributions. Nevertheless, a significant number of particles still obtain their initial properties, and the scattered particles suffered only a small number of collisions. Therefore, in this intermediate regime, the distribution of the arriving flux is sensitive to both, the initial distribution and the inter-atomic scattering potentials.

An important parameter of the gas phase transport is the mean free path of the sputtered particle λ_m

$$\lambda_m = \frac{1}{n_g \sigma} = \frac{k_B T}{p \sigma} \quad \text{Eq. 2.7}$$

with n_g the density, T the temperature, p the pressure, k_B the Boltzmann constant, and σ the collision cross section.

Although there is only one physical collision cross section, there are several mathematical methods to approximate it. The simplest one is the hard sphere approximation, where

$$\sigma = \pi(r_s + r_g)^2 \quad \text{Eq. 2.8}$$

with r_s and r_g being the atomic radius of the sputtered particle and the background gas, respectively. When taking into account the gas motion, the collision cross section according to kinetic gas theory is given by

$$\sigma = \pi(r_s + r_g)^2 \left(1 + \frac{m_s}{m_g}\right)^{1/2} \quad \text{Eq. 2.9}$$

where m_s and m_g are the masses of the sputtered particle and the background gas, respectively [69]. Due to its simplicity, the hard sphere approximation does not reproduce well the interaction between the two colliding particles [48, 63, 66]. It completely neglects the energy of the particles, thus leading to a too high deflection of high energy particles. Nonetheless it is often used, since its simplicity saves computational time and allows some equations to be solved analytical [62, 63], while more complex solutions often require a numerical approach or the use of MC-simulations.

The use of more realistic interaction potentials raises the problem, that that the range of their interaction is theoretically infinite. To overcome this problem, a maximal impact parameter b_{max} can be used. Its definition is that the deflection angle in the centre of mass system θ_{com} is equal to an arbitrarily chosen minimal deflection angle θ_{min} (figure 2.8). This value θ_{min} is usually in the range between 0.2° and 2° [19, 48, 70]. A smaller θ_{min} provides a better accuracy, but on the other hand increases computational time.

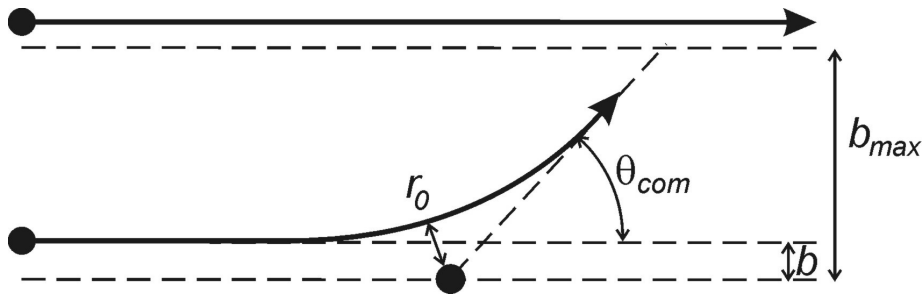


Figure 2.8 The geometry of the scattering potential in the centre of mass frame

The collision cross section can then be given as

$$\sigma = \pi b_{\max}^2 \quad \text{Eq. 2.10}$$

For a spherical atom-atom interaction potential $V(r)$ the scattering angle is given by:

$$2\theta_{\text{com}} = \pi - 2b \int_{r_0}^{\infty} \frac{dr}{r^2 \left\{ 1 - [V(r)/E_{\text{com}}] - (b^2/r^2) \right\}^{1/2}}, \quad \text{Eq. 2.11}$$

in which r_0 is determined by

$$b^2 = r_0^2 \left(1 - \frac{V(r_0)}{E_{\text{com}}} \right), \quad \text{Eq. 2.12}$$

with b being the impact parameter, r the interatomic distance, E_{com} the energy of the sputtered particle in the centre of mass system, and $V(r)$ the interaction potential between the two atoms. The interaction potential $V(r)$ is of great importance for the scattering process, and there are a lot of different approximations for this potential. The question which potential is used in a simulation is a tradeoff between accuracy and computational time. There are two different families of inter-atomic interaction potentials, those, which are repulsive only, and those, which also feature an attractive component.

The repulsive potentials can be divided into the group of screened Coulomb potentials and the empirical Born Mayer potential.

The screened Coulomb potential can be written as:

$$V(r) = \frac{Z_1 Z_2 e^2}{r} \Phi(r/a) \quad \text{Eq. 2.13}$$

where $\Phi(r/a)$ is the screening function and a the screening length. There are several screening functions, like Molière, Kr-C, Ziegler-Biersack-Littmark or Lenz-Jensen. [71] gives a good overview of the different functions. The second repulsive potential is the Born-Mayer or Abrahamson potential [72] which is given by:

$$V(r) = A_{BM} e^{-B_{BM} r} \quad \text{Eq. 2.14}$$

with A_{BM} being an energy parameter and B_{BM} a screening length.

The attractive potentials also take into account the long range attractive force between two atoms, which are approaching at intermediate energies. On the side of the attractive potentials there is the often applied Morse potential given by:

$$V(r) = D[\exp(-2\alpha(r-r_0)) - 2\exp(-\alpha(r-r_0))] \quad \text{Eq. 2.15}$$

where D , α , and r_0 are parameters given in [71]. Another often used attractive potential is the Lennard-Jones potential, which is given by:

$$V(r) = \lambda_6 r^{-6} - \lambda_{12} r^{-12} \quad \text{Eq. 2.16}$$

Also combinations of two potentials, like an attractive and a repulsive [48] are often used. New models use quantum-chemical interaction potentials, utilizing the Kohn-Sham density functional theory [73]. These potentials feature an attractive and repulsive part.

The question which potential is used is also often influenced by the energy range of the collisions which should be simulated. For high energy collisions, repulsive only potentials are often sufficient. When the energy of the sputtered particle decreases, the importance of the attractive nature of the inter-atomic force increases. At low energies (thermal energies) the hard sphere approach is often sufficient, or the particle as can even be considered as moving randomly. Because of this, most MC-simulations use different scattering processes for different particle energies.

The remaining energy E' in the laboratory frame after an elastic collision is expressed by

$$E' = E \left(1 - \frac{2(1 - \cos \theta_{com}) m_g m_s}{(m_s + m_g)^2} \right) \quad \text{Eq. 2.17}$$

where E is the initial particle energy. Westwood [62] calculated the average scattering angle, using the hard sphere model, as a function of the ratio $M = m_g/m_s$ as:

$$\langle \cos \theta \rangle = 1 - M^2/3 \quad \text{for } M < 1 \quad \text{and} \quad \text{Eq. 2.18}$$

$$\langle \cos \theta \rangle = 2/(3M) \quad \text{for } M > 1$$

The average scattering angle $\langle \theta \rangle$ and the average retaining energy $\langle E'/E \rangle$ as a function of M is shown in figure 2.9.

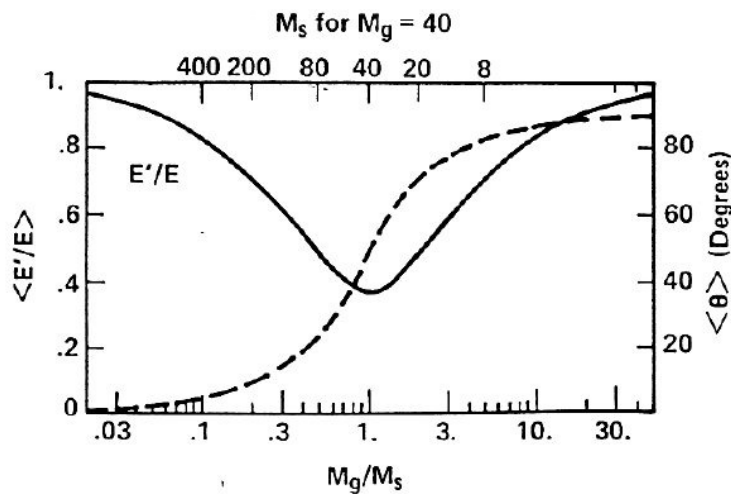


Figure 2.9 The average fraction of energy retained (solid line) by an atom of mass m_s in collision with an atom of mass m_g and the average angle of deviation (dashed line) due to the collision [Westwood1978].

Atoms that are lighter than the working gas retain a lot of their initial energy but are scattered to large angles. Atoms with equal masses lose the most energy in the collision. Heavy atoms are suffering just a small deviation in direction and energy/impulse in a collision. This effect is called velocity persistence and describes the degree of conservation of the original impulse [62, 67]

Today, the sputtering process and the gas phase transport in particular are simulated via MC-algorithms. Nonetheless, there were also approaches in the past [47, 62, 63,

67, 74] to calculate the mean energy or degree of thermalization of the arriving flux analytically with different approaches.

Westwood [62] estimated the energy loss for sputtered particles suffering hard-sphere collisions with the working gas. He considered that the atom is scattered with the average angle and is therefore moving in a zigzagged trajectory, and calculated the average distance the atoms traveled before being thermalized. His model did not take into account the initial spread of energy. The number of needed collisions η for an atom starting with E_0 to be reduced to the energy E_g of the working gas is given in his model by

$$\eta = \ln(E_0/E_g) / \ln(E'/E) \quad \text{Eq. 2.19}$$

where E'/E is the fraction of retained energy (see *figure 2.9*).

Gras Marti and Valles-Abarca [63] used a continuous slowing down (c.s.d.) approach of the sputtered particles, hence they travel at straight trajectories (neglecting scattering) and continuously lose their energy. They used the Thompson distribution (Eq. 2.4) as their starting energy distribution and applied a velocity proportional energy loss per unit path length on their path through the working gas. The degree of thermalization P_{therm} is then given by:

$$P_{therm} = \frac{x^2}{R(U)^2 + x^2} \quad \text{Eq. 2.20}$$

where x is the distance from the target and $R(U)$ (Eq. 2.20) is the path length of a particle with initial energy U_s until thermalization is reached.

$$R(U_s) = A \cdot U_s^{1/2}. \quad \text{Eq. 2.21}$$

The energy independent coefficient A is given by

$$A \cong \frac{0.012}{m_g^{1/2}} \left(1 + \frac{1}{M}\right)^{1/2} (1 + M^{2/3})^{3/4} \frac{T(K)}{p(Pa)} \quad \text{Eq. 2.22}$$

Another very interesting approach which is using the thermalization of the sputtered particle is the Keller-Simmons formula [47, 67, 74-76] which calculates the arriving flux $\Phi(pd)$ at the substrate as a function of the pressure distance product pd and a so called characteristic pressure distance product $(pd)_0$. The model considers a flux of fast ballistic atoms Φ_b that decreases exponentially with pd :

$$\Phi_b(pd) = \Phi_0 \exp\left(-\frac{pd}{(pd)_0}\right) \quad \text{Eq. 2.23}$$

The atoms of the ballistic flux that suffered a collision are assumed to lose all their energy in one collision and switch to a diffusive motion. Their flux Φ_d at the substrate is then given by:

$$\Phi_d(pd) = \Phi_0 \left[\frac{(pd)_0}{pd} - \left(1 + \frac{(pd)_0}{pd}\right) \exp\left(-\frac{pd}{(pd)_0}\right) \right] \quad \text{Eq. 2.24}$$

with a total flux of:

$$\Phi(pd) = \Phi_b + \Phi_d = \Phi_0 \frac{(pd)_0}{pd} \left(1 - \exp\left(-\frac{pd}{(pd)_0}\right)\right). \quad \text{Eq. 2.25}$$

Although the Keller-Simmons formula makes use of the oversimplified assumption that there are just two distinct states of atoms, un-scattered particles at fast velocities and ballistic motion and scattered particles at thermal energies and diffusive motion, its result on the deposition rate is well reproduced by experiments. It also gives an easily understandable way, how the flux changes from ballistic to diffusive particles (*figure 2.10*)

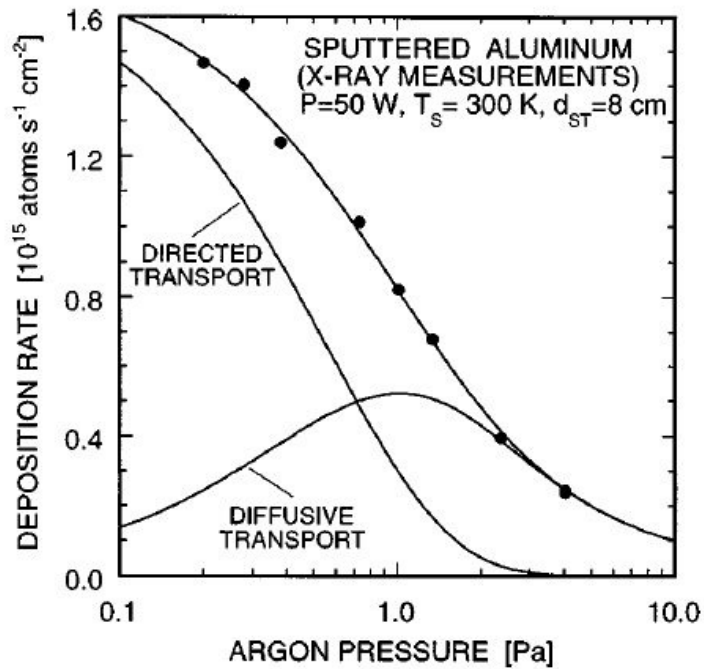


Figure 2.10 Atomic deposition rate as a function of argon pressure for aluminum. The experimental results (dots with fit curve) for the total flux can be interpreted by a distinction between directed and diffusive transport according to the Keller Simons formula [67]

One disadvantage of the KS-formula is the characteristic pressure distance product $(pd)_0$, as it is an empiric parameter, and its dependency on different sputter parameters is not well understood, and it has to be measured individually for different sputter deposition setups. Nonetheless Drüsedau (see figure 2.11) showed a clear dependency between $(pd)_0$ and the velocity persistence v , given by Westwood [62].

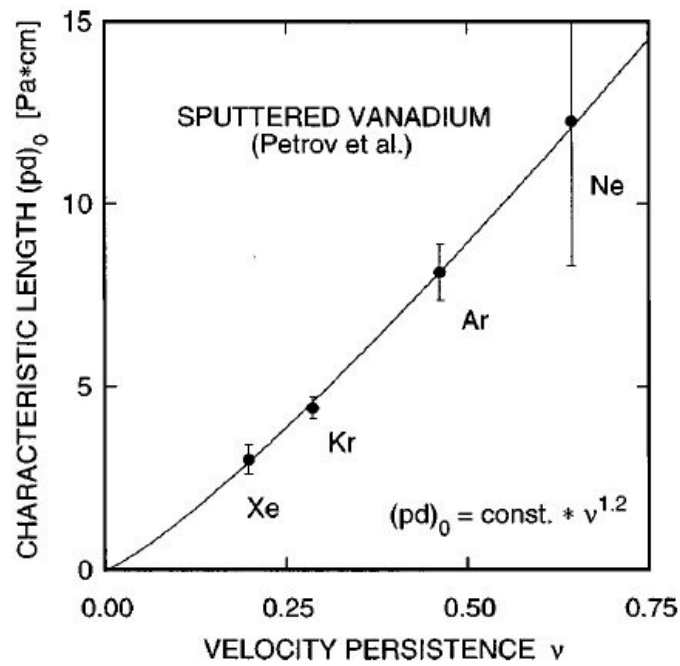


Figure 2.11. Characteristic pressure-distance product $(pd)_0$ as a function of the calculated velocity persistence for sputtering of Vanadium in different noble gases [67]

2.2 Reactive Sputtering

It was a part of this thesis to study the influence of a reactive gas on the angular distribution. Therefore it is necessary to try to understand the important mechanics in reactive sputter deposition. Unlike non-reactive sputter deposition, which is usually easy to control, the reactive sputter deposition process is much more complex, as the state of the target is influenced by the working gas. This may even lead to avalanche-like transitions between different sputtering regimes, which is a difficulty for process control. A model to describe and predict the behavior of the reactive sputter deposition process is the so called “Berg’s model” [78-84]. Despite its simplicity, it is in good agreement with experimental results. It will be briefly described below.

Berg’s model assumes that a fraction of the target and the substrate surface forms a compound with the reactive gas. The metal and the metal-reactant compound have different physical properties, like e.g. the sputtering yield, which is usually higher for a metal than for a compound. To explain what happens if a reactive gas, in this case oxygen, is added to the sputtering process an example is given in *figure 2.12*.

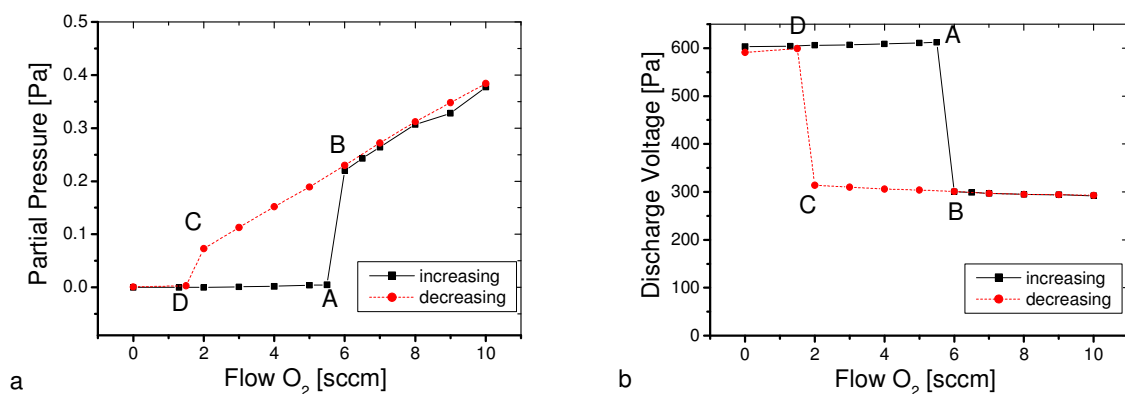


Figure 2.12. a) oxygen partial pressure and b) discharge voltage of Al sputtered with 0.3 Pa (6 sccm) Ar and variable oxygen flow.

The starting point is sputtering Al with 0.3 Pa Ar (Ar partial pressure is kept constant). As we start adding an oxygen flow to the Ar base pressure, the voltage and the total pressure remain constant, therefore there is no relevant oxygen partial pressure in the deposition chamber, until the point A in *figure 2.12* is reached. The deposition mode until point A is called the “metallic” mode. The sputtered Al at the substrate or the chamber walls is getting the complete oxygen flux, hence acting basically as a vacuum pump. The compound on the target that is formed by the small oxygen

partial pressure is instantly removed; the surface of the target stays metallic. The stoichiometry of the deposited Al at the chamber walls changes with increasing oxygen flux, from pure aluminum at the starting point up to alumina (Al_2O_3) at the point A. As soon as stoichiometric alumina is formed at the chamber walls, the gettering process disappears and the oxygen partial pressure rises. The oxygen in the chamber now reacts with the target and is forming a compound on the target surface. Since the compound has a smaller sputtering yield than the metal, the sputter rate of Al in the chamber decreases, leading to a higher oxygen partial pressure and thus to the formation of a higher fraction of the target to be oxidized. This avalanche like effect leads to a sudden change in the process characteristic (point B in *figure 2.12*), hence an increased oxygen partial pressure and a different discharge voltage, which represent the different secondary electron yields of the compound compared to the pure metal. This deposition mode is called “reactive mode” or, since the target is oxidized, often also is referred to as “poisoned mode”.

A further increase in the oxygen flux leads to an increased oxygen partial pressure, but has no distinct influence on the sputtering process. When we decrease the oxygen until point B is reached the deposition mode is not switching back to metallic mode. In fact we have to decrease the oxygen flux even further until 2 sccm (point C) to have the same avalanche like transition from poisoned to metallic mode (point D). This effect is due to the reduced sputter rate in the poisoned mode. There is not enough sputtered metal to getter all the oxygen at 5.5 sccm (point A), which is the case in metallic mode with its higher sputtering and deposition rate. Therefore the further decrease of the oxygen flow is needed to switch back to metallic mode. This hysteresis behavior makes process control in reactive sputtering difficult, especially, as the highest deposition rate for oxidic layers from a metallic target is close to point A.

Berg was able to describe this effect with steady state equations, and also to identify different parameters that have an impact on the hysteresis behavior of a reactive sputter process. It is also necessary to say that not all materials have such an abrupt transition as in the example with Al described above, and that the oxygen flow / discharge voltage diagram may have a very complex shape.

Following material properties or process parameters are known for influencing the process condition and hysteresis behavior [85-88]

- **Reactivity:** The value of the sticking coefficient α of the reactive gas on the sputtered material indicates the reactivity of the deposited specimen. The hysteresis process will be less pronounced for low reactivity processes.
- **Sputtering yield:** The ratio of the sputtering yield of the metal and the compound has also a distinct effect. The hysteresis is less pronounced, if there is just a low deviation between these two sputter yields.
- **Pumping speed:** One parameter influencing the hysteresis behavior which can be controlled externally is the pumping speed of the vacuum system. *Figure 2.13* shows the discharge voltage behavior of the same system as shown in *figure 2.12*, with the difference, that the pumping speed is 140 l/s instead of 35 l/s. The reason for this behavior is that with increased pumping speed the gettering effect is less pronounced.
- **Target size:** Another material independent parameter is the size of the sputtered target surface. The smaller the target surface the less pronounced the hysteresis effect.

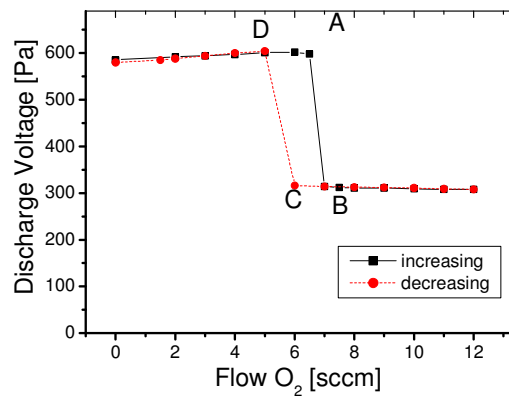


Figure 2.13: Discharge voltage of Al sputtered with 0.3 Pa (24.4 sccm) Ar and variable oxygen flow. The pumping speed is approximately four times higher compared to figure 2.12.

Taking into account the above mentioned influences, the hysteresis might not even appear for a setup with the right parameters (e.g. low reactive material combined with high pumping speed).

Additional to “Berg’s model” another interesting effect which might influence the angular distribution of the arriving flux is known [89]. It describes, that due to the inhomogeneous local sputter rate of planar magnetrons, the target is preferentially poisoned at the edge of the race-track. Therefore most particles are sputtered preferentially from a small ring in the center of the racetrack where the target is still in a metallic condition. The size of this metallic area diminishes with increasing oxygen flow.

Another question is the gas phase transport of particles ejected from a compound surface. Snyders et al [90-93] investigated the composition of the magnetron plasma for Ti, Sn and Ag, where Ti was the most reactive material. The composition of the plasma of the Ti sputter process can be seen in figure 2.14. The transition from metallic to reaction mode is located between $2 \cdot 10^{-2}$ to $6 \cdot 10^{-2}$ Pa introduced oxygen partial pressure. During the transition, the amount of atomic Ti in the plasma diminishes completely and TiO is formed (figure 2.14a). When the oxygen partial pressure is further increased, the amount of TiO₂ increases at the cost of TiO (figure 2.14b).

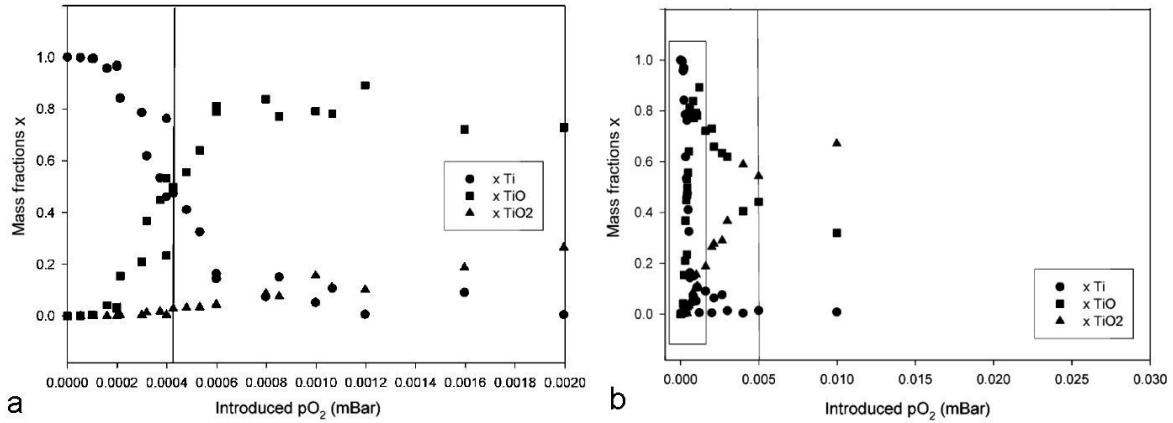


Figure 2.14: The composition of the sputtered specimen in the discharge plasma measured by glow discharge mass spectroscopy for Ti sputtered in an Ar/O₂ atmosphere. a) The transition between metallic and reactive mode. The amount of atomic Ti decreases with the oxygen partial pressure while the amount of TiO increases sharply. b) When the oxygen pressure is further increased, TiO decreases and the amount of TiO₂ increases [91].

Besides the fact, that the sputtered specimen in reactive mode is transported as a compound, there are also other effects that might influence the gas phase transport of the sputtered particles. For example, a part of the oxygen molecules dissociates in the plasma to a high amount. The dissociation level of oxygen can be estimated to be 11% [93]. As the binding energy of the compound is higher than that of the pure metal, it can also be estimated that the average energy of the sputtered specimens is higher from a compound surface, according to the Thompson formula [Eq. 2.4].

As even the scattering between an atomic specimen and a noble (atomic) gas atom is not trivial (see section 2.1.2.), the scattering process between a compound and a noble gas atom or an oxygen molecule is quite complex.

Since the reactive sputter deposition was widely investigated over the last years, a vast amount of papers have been published about different aspects of the reactive sputter deposition process, and a total description of this process would be beyond the scope of this thesis. For further literature that might be interesting in the context of this thesis, the author refers to the work of Kubart *et al* [94-97] which describes the modeling of the reactive sputter process, and the work of Möller *et al* [98, 99] who have studied the plasma target interaction. Further the author wants to refer to recent publications of other parts of the project "Growth of complex oxides" which e.g. investigated the sticking coefficient or the incorporation of the reactive gas in the film [100, 101], the momentum flux towards the substrate [102], the influence of the magnetic field configuration during reactive sputtering [103], the simulation of the

reactive deposition from a rotating cylindrical magnetron [104], or the compositional effects on the growth of Mg[M]O films [105].

3 Metal Flux Monitor

The Metal Flux Monitor (MFM) is a pinhole camera which converts the information of the angular distribution of the metal flux at the position of the pinhole into a thickness profile on the substrate, either planar or cylindrical, behind that pinhole.

The pinhole camera is the simplest form of a camera and its principle is known for centuries. Even some animals (e.g. the Nautilus) are using eyes with a pinhole instead of a lens. The pinhole camera doesn't use a lens to focus the light rays from the object to form an image. Instead the light rays pass a very small aperture (pinhole) to form an inverted image of the object on the screen. The resolution of the image is determined by the ratio between the radius of the pinhole and the distance between pinhole and screen. Hence, the ideal pinhole camera would have an infinitely small pinhole and a great distance between the pinhole and the screen. On the other hand the needed exposure time would also increase to infinity with increasing resolution. Hence, there is a tradeoff between resolution and exposure time. Another limiting factor is diffraction which may be neglected when using particles instead of electromagnetic radiation.

The principle of the camera was chosen for the MFM, as it is simple and requires no sort of lenses. The pinhole camera which is used to detect particles (*figure 3.1*) is the same for optical imaging, with the following analogies. The angular distribution of the particle flux at the pinhole corresponds to the light rays at the pinhole that were emitted from an object, hence the projected image at the screen represents the inverted angular distribution of the flux at the pinhole, either as light rays or particle beam. The light intensities on the screen are captured by photosensitive material for visualization. Neutral particles are simply collected on a substrate, with the thickness profile $T(x)$ representing the intensity distribution of the flux and therefore the angular distribution $\Phi(\varphi)$ of the metal flux at the pinhole.

In the present thesis, the thickness profile $T(x)$ along a strip of approximately 0.5mm is measured and converted into the angular flux $\Phi(\varphi)$ of impinging particles at the pinhole.

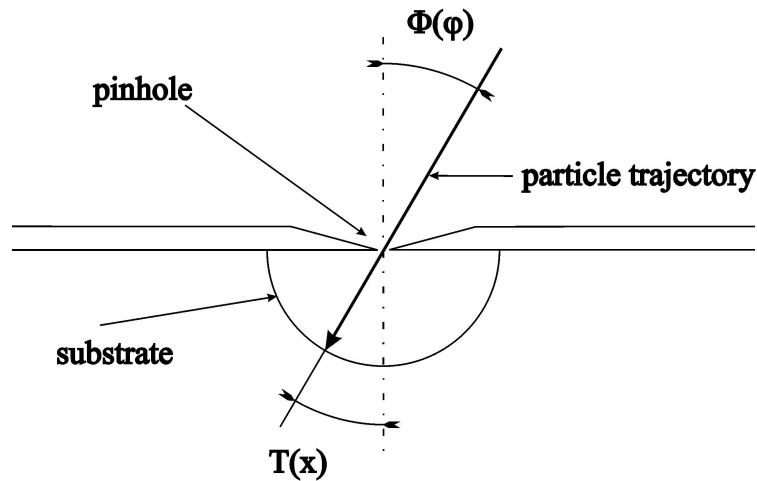


Figure 3.1: Sketch of the working principle of the pinhole camera for measuring the angular distribution of the impinging particles with a cylindrical.

The MFM itself is a sealed (except the pinhole) cylindrically shaped chamber, which is connected to a stainless steel pipe with a KF40 linear feed-through.

There is a MFM with the pinhole located perpendicular to the feed-through axis, which can hold a cylindrical (MFM1d *figure 3.2a*) or a planar substrate holder (MFMplan *figure 3.2b*), and one with the pinhole located parallel to the feed-through axis, which can only hold a planar substrate holder (MFMZ *figure 3.2c*). A MFM with a cylindrical substrate, where the collectable area is not restricted to a small strip (MFM2d *figure 3.2d*) has also been constructed, but not used as the large substrates proved to be cumbersome in data analysis.

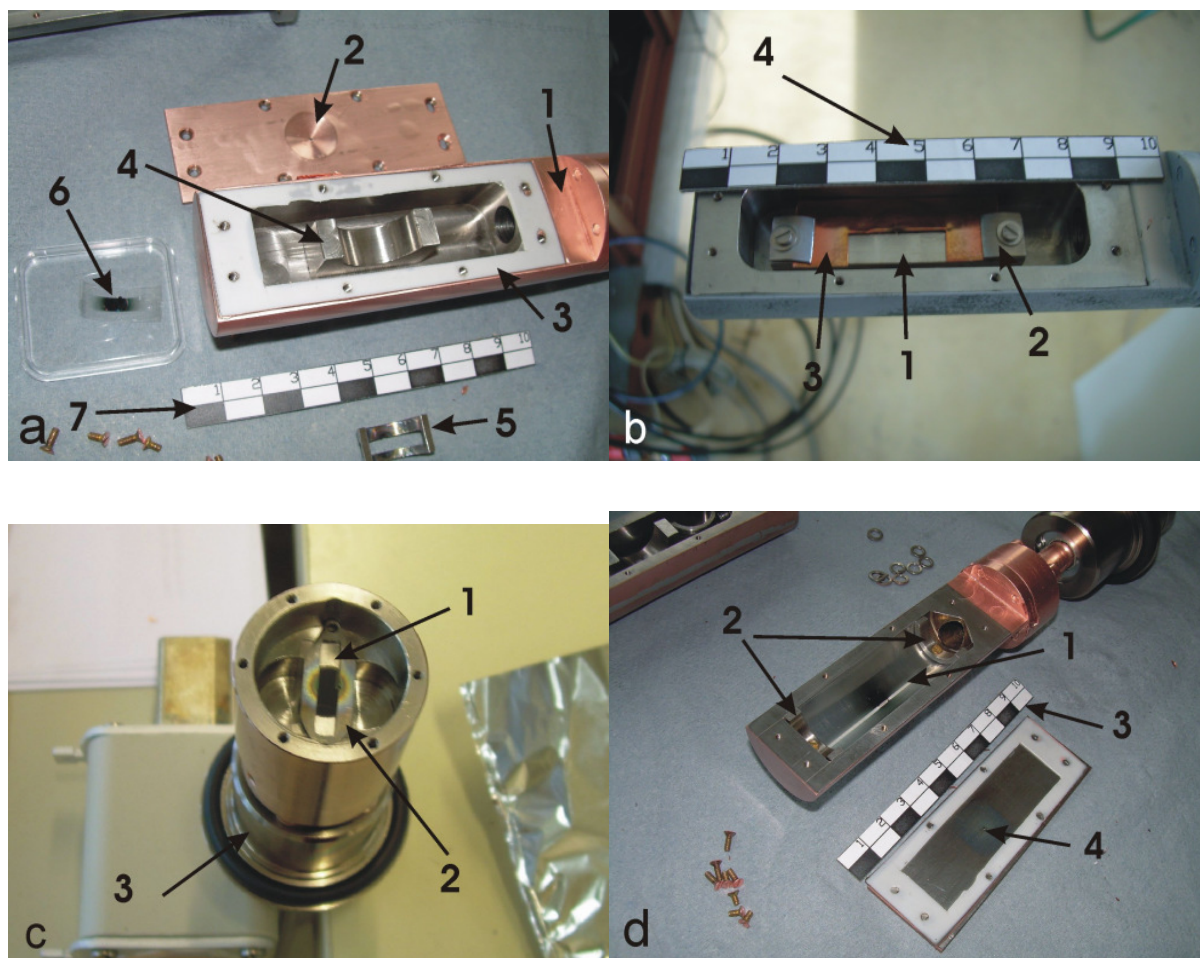


Figure 3.2: The different types of MFM a) image of the MFM with pinhole located perpendicular to the feed-through axes (MFM1d), indicated parts are 1: housing, 2: pinhole, 3: gasket, 4: cylindrical substrate holder, 5: cylindrical bracket, 6: coated slide, 7: measuring bar of 10 cm. b) Same MFM as figure 3.2a but with planar substrate holder (MFMplan), indicated parts are: 1: planar substrate holder, 2: fixing clamps, 3: mask made of copper, 4: measuring bar. c) MFM with pinhole located parallel to feedthrough axis (MFMZ), indicated parts are: 1: coated substrate, 2: fixing mask, 3: KF-40 linear feed-through. d) MFM with large cylindrical substrate (MFM2d), indicated parts are: 1: coated transparent substrate, 2: fixing clamps, 3: metering bar, 4: pinhole.

The direct connection of the MFM to a pipe and a linear feed-through enhances its flexibility, as it can be mounted to any type of deposition chamber with a KF40 flange, and its position can be changed quickly. It also enables differential pumping of the MFM via the pipe (to increase the mean free path of particles inside the MFM), and the inlet of reactants directly into the MFM from outside the recipient. Some important data is given in *table 1*.

radius pinhole r	0.5 mm
length pinhole d	0.2 mm
Maximum angular error $\Delta\varphi$	2.9°
Cover plate thickness	2 mm
Radius cylindrical substrate holder	10 mm
Distance pinhole to planar substrate	10 mm
Acceptance angle cylindrical	75°
Acceptance angle planar	45°

Table 3.1 Technical Data MFM

The pinhole was cut mechanically into the cover plate, at the bottom of a cone (angle 75°). The length of the pinhole d (0.2 mm) was the limit of this production method, as a further decrease would pose the threat of a mechanical deformation during the production process. The advantage of this production technique is the high mechanical stability of the pinhole.

A potential problem of the pinhole could be that it is subjected to the metal flux during the experiment and that the deposited material could be disadvantageous for the properties of the pinhole camera, i.e. it decreases r or increases d over time. The radius of the pinhole was occasionally monitored via a light microscope, but no distinct variations could be observed. To clean the cover plate and the pinhole from the deposited material, it was sufficient to lift off the entire coating when its thickness was high enough to guarantee mechanical stability. With this technique, the coating could be completely removed, without subjecting the pinhole to mechanical forces or chemical agents.

3.1 Corrections and limitations

3.1.1 Vignetting

To convert the thickness profile $T(x)$ on the substrate into the angular flux $\Phi(\varphi)$ of impinging particles at the pinhole site, one has to take into account the geometry of the pinhole. The effective area of the pinhole decreases with increasing angle, an effect called vignetting ($V(\varphi)$) (figure 3.3), thus also decreasing the number of passing particles.

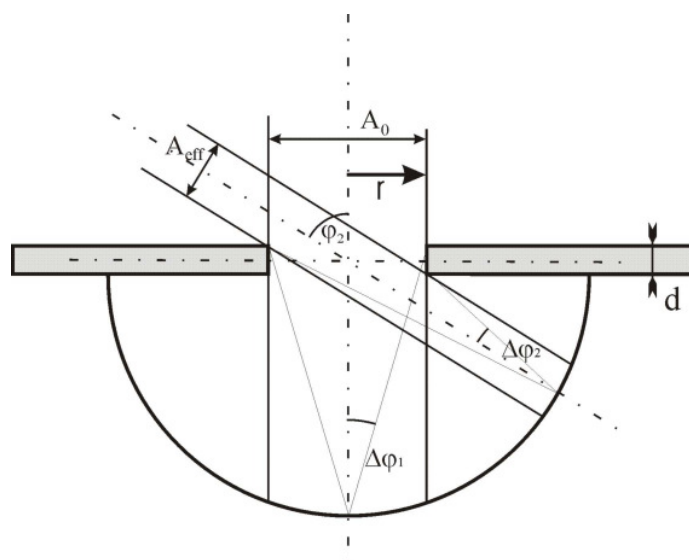


Figure 3.3: Vignetting: Two particles are entering the MFM at different angles φ ; one perpendicular ($\varphi_1 = 0^\circ$; aperture A_0 of $r^2\pi$) and the second one at an angle φ_2 with a smaller aperture of A_{eff} . The angular error $\Delta\varphi$ decreases at higher angles because of the decreasing aperture.

For a cylindrical pinhole (length d ; radius r) $V(\varphi)$ is described as the ratio of the effective area A_{eff} seen by the tilted beam to the area of the pinhole A_0 . A_0 can be expressed as $r^2\pi$. The effective area of the cylindrical pinhole approached by a particle with an incident angle φ is sketched in figure 3.4.

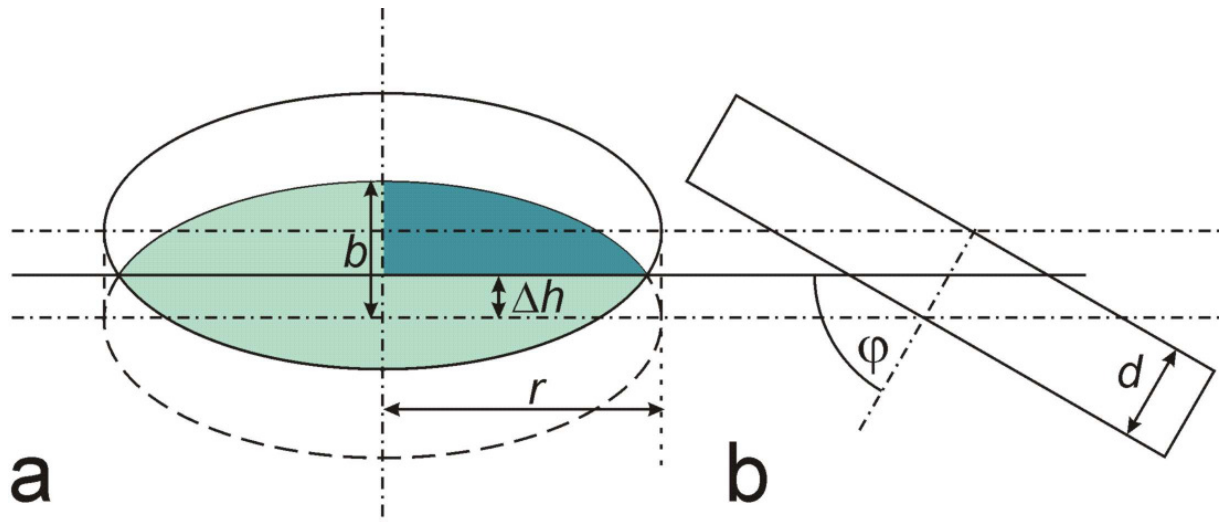


Figure 3.4: The effective area A_{eff} of a cylindrical pinhole (length d ; radius r) seen by a particle with an incidence angle of φ (a: top view; b: side view). It can be described as the cross-section (highlighted by light blue) of two ellipses shifted by $2\Delta = d \cdot \sin\varphi$. The length of the major-axis is r and the length of the minor-axis is $b = r \cdot \cos\varphi$. The effective area consists of 4 equal parts (highlighted by dark blue).

As sketched in figure 3.4 A_{eff} can be calculated (complete derivation is given in the appendix) according to

$$A_{eff} = 2r^2 \cos\varphi \left[\frac{\pi}{2} - \arcsin\left(\frac{d \tan\varphi}{2r}\right) - \left(\frac{d}{2r} \tan\varphi \cdot \sqrt{1 - \left(\frac{d \tan\varphi}{2r}\right)^2}\right) \right]. \quad \text{Eq. 3.1}$$

Taking into account that this equation is only valid for the absolute value of φ , $V(\varphi)$ can be expressed as

$$V(\varphi) = \frac{A_{eff}}{A_0} = \frac{2 \cos(\varphi)}{\pi} \left[\frac{\pi}{2} - \arcsin\left(\frac{d \tan(|\varphi|)}{2r}\right) - \left(\frac{d \tan(|\varphi|)}{2r} \sqrt{1 - \left(\frac{d \tan(|\varphi|)}{2r}\right)^2}\right) \right]. \quad \text{Eq. 3.2}$$

3.1.2 Angular error

The resolution of the pinhole camera is limited, as the pinhole has a finite diameter r , therefore the incidence angle φ of a particle may have a small deviation. To calculate the maximal angular error $\Delta\varphi$ (see figure 3.3) we take the point right below the pinhole ($\varphi = 0$) with a distance R to the pinhole. The maximum angular error is can be expressed as:

$$\Delta\varphi_0 = \arctan\left(\frac{r}{R}\right) \quad \text{Eq. 3.3}$$

For the values given in *table 3.1* the corresponding $\Delta\varphi_0$ is 2.9° . When the angle increases the angular error decreases due to the vignetting effect.

3.1.3 Angle dependant sticking probability

Another limiting factor is that only those particles which stick contribute to film growth and can therefore be measured. The sticking probability is determined by energy and incidence angle [106]. For the cylindrically shaped substrate the incidence angle is always perpendicular, therefore the sticking probability can be assumed to be 1, even at higher energies [106]. As mentioned above, the incidence angle on the planar substrate is not perpendicular. The sticking probability, however, becomes angle dependant only at higher angles [106] (above 45° , which is the maximum acceptance angle of the MFM). Moreover, in the described experiments the particles which are not scattered, and therefore have higher energies, have typically incidence angles of 20° and below. Therefore, even for the planar substrate the sticking coefficient can be assumed to be 1.

3.1.4 Gas phase scattering inside the MFM and the reduction of the deposition rate

Gas phase scattering of the sputtered particles does not only take place on the way from the target to the pinhole, but of course also inside the MFM, where it limits the resolution. Therefore it seems reasonable to limit the working gas pressure inside the MFM. Another problem is the residual gas inside the MFM.

Due to the pinhole geometry, the deposition rate on the substrate is drastically reduced (by a factor of approx. 0.01 and lower), thus increasing problems with residual gas incorporation. The reason is that the ratio of the impingement rates of the residual gas molecules v_g [107] and of the sputtered particles v_d , given in Eq. 3.4, increases with decreasing deposition rate.

$$\frac{v_g}{v_d} = \frac{m_d \cdot p}{a_w \rho \sqrt{2\pi m_g k_B T}} \quad \text{Eq. 3.4}$$

where p [Pa] is the residual gas pressure, m_g [kg] is the molecular or atomic mass of the residual gas, m_d [kg] is the molecular or atomic mass of the sputtered material, k_B is the Boltzmann constant, T [K] is the temperature of the gas, a_w [ms^{-1}] is the deposition rate, and ρ [kgm^{-3}] is the density of deposited material.

If one assumes a residual oxygen pressure of 10^{-5} Pa and a deposition rate of $5 \cdot 10^{-12} \text{ ms}^{-1}$ of Al inside the MFM the ratio v_g/v_d would be approximately 1. Knowing that the oxygen incorporation coefficient during sputter deposition of reactive metals like Al and Mg can reach values up to 0.1-0.25 [100, 101], the formation of oxide layers seems unavoidable, even for a low residual gas pressure.

To overcome these problems a differential pumping system has been added to the MFM. As stated above, the pinhole camera is connected to a stainless steel pipe (length 110 cm, inside diameter 1 cm) leading outside of the vacuum chamber through the linear feed-through. At this side of the pipe an Adixen ATH 31 turbomolecular pump (performance 20l/s) is installed, which is backed by a diaphragm pump (*figure 3.5*). A Pirani Penning combination vacuum gauge (Alcatel Adixen ACC2009) is added to monitor the pressure. The differential pumping has the additional advantage that reactants can be directly fed into the MFM through the pipe, thus avoiding the poisoning of the target.

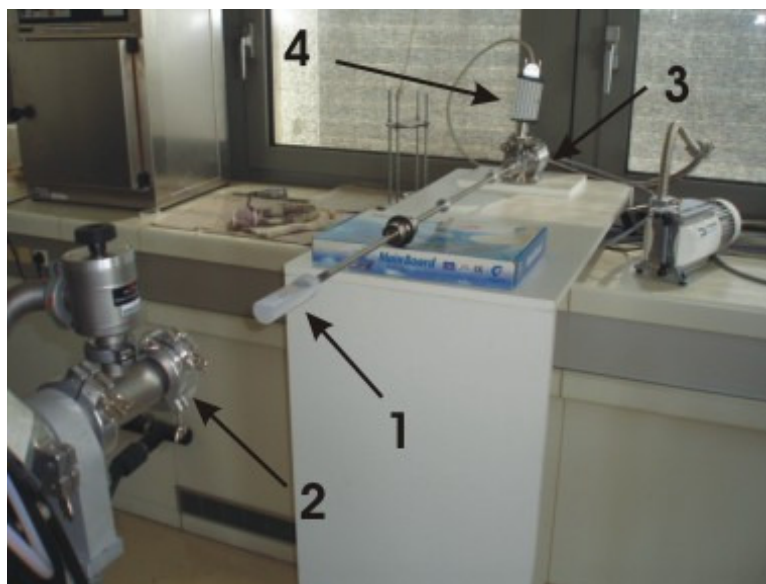


Figure 3.5: The differential pumping system of the MFM. Indicated are: 1: pinhole camera; 2: load lock system of the vacuum chamber; 3: turbo molecular pump backed with a diaphragm pump; 4: pressure gauge.

To calculate the efficiency of the pumping system we compare the pressure in the recipient p_1 with the pressure inside the MFM p_2 , assuming free molecular flow and a system sketched in *figure 3.6*.

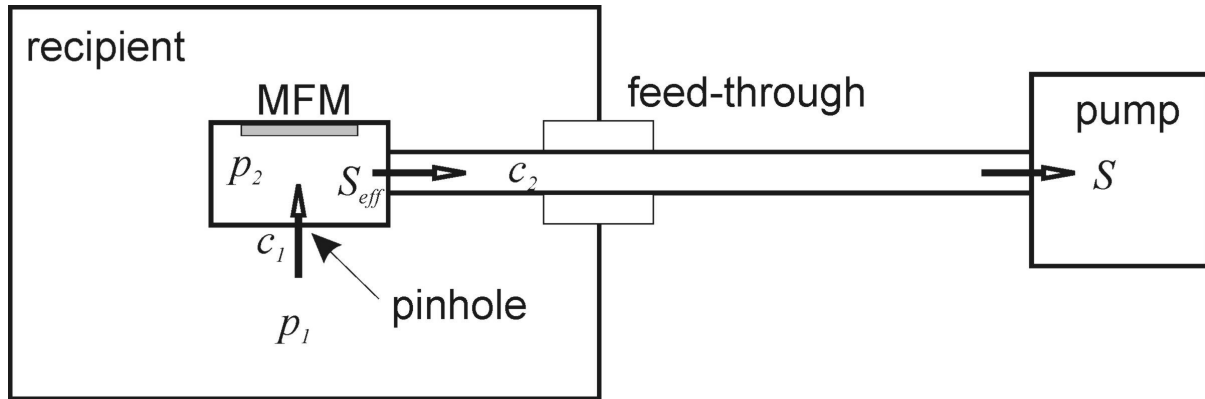


Figure 3.6: Sketch of the differential pumping system of the MFM.

The gas flow Q (indicated by the arrows) is constant and is given by two equations (Eq. 3.5; Eq. 3.6):

$$Q = c_1 \cdot (p_1 + p_2) \quad \text{Eq. 3.5}$$

$$Q = S_{eff} \cdot p_2 \quad \text{Eq. 3.6}$$

$$\Rightarrow p_2 = p_1 \cdot \frac{c_1}{(c_1 + S_{eff})} \quad \text{Eq. 3.7}$$

where c_1 [Pa·l/s] is the conductance of the pinhole, S_{eff} [Pa·l/s] is the effective pumping speed, p_1 [Pa] is the working gas pressure inside the recipient, and p_2 [Pa] is the pressure inside the MFM. S_{eff} can be calculated by:

$$S_{eff} = \frac{c_2}{1 + \frac{c_2}{S}}, \quad \text{Eq. 3.8}$$

where S is the pumping speed of the turbo-molecular pump [20 l/s], and c_2 is the conductance of the pipe. The conductance of a tube or pipe can be calculated by [108]:

$$c = \frac{\bar{c} r^2 \pi}{4} \cdot \frac{14 + 4 \frac{l}{d}}{14 + 18 \frac{l}{d} + 3 \left(\frac{l}{d} \right)^2} \quad \text{Eq. 3.9}$$

where \bar{c} is the mean particle velocity (for Ar 397 m/s), l is the length, and d is the diameter of the tube. The conductance c_1 of the pinhole (length 0.2 mm; diameter 1 mm) is $6.5 \cdot 10^{-2}$ l/s, and the conductance c_2 of the pipe (length 110 cm; 1 cm) is $9.2 \cdot 10^{-2}$ l/s. Since c_2 is much smaller than S (20 l/s), S_{eff} can be approximated by c_2 ($S_{eff} \approx c_2$), hence the effective pumping speed is determined solely by the conductance of the pipe (see Eq. 3.7). The calculated p_2 is 41% of p_1 , thus doubling the mean free path of the particles inside the MFM.

The influence of the scattering inside the MFM on the thickness profile was simulated via SIMTRA (see section 4.1) for Cu at pressures of 0.3 Pa and 1 Pa, respectively. The simulations were carried out with $p_2 = 0$ (assumed ideal case), $p_2 = 1/2 p_1$ (differentially pumped), and $p_2 = p_1$ (no differential pumping). The simulations showed, that there was a visible, but quite minor influence, although a considerable amount of particles is scattered at finite pressures in the chamber. A difference can occur at higher angles, as the amount of non-scattered flux diminishes here, due to the vignetting effect, leading to an overweighting of the particles scattered inside the MFM.

Since differential pumping complicates the test array, and reduces its flexibility, without having a distinct influence on the angular distribution, it was only used for a few measurement series. There its main purpose was to decrease the amount of residual gas atoms and to enable the controlled inlet of reactants into the MFM.

3.2 Conversion of the thickness profile to the angular distribution

As stated in section 3.1.1 different substrates and substrate holders (see *figure 3.2*) were used.

At first, cylindrical substrate holders were used, with flexible substrates. The flexible substrate (in this case a transparent overhead slide, HP Single Sheet PaintJet Film) was put between the holder and the bracket to be coated. The bracket has a slit (4 mm wide, acceptance angle from -75° to $+75^\circ$) with a notch in the middle to mark the centre of the substrate for later investigations.

The cylindrical holder has the advantage that every point of the substrate has the same distance to the orifice (this was considered to be important, because scattering between sputtered atoms and gas may take place even within the camera). Also the incidence angle between the sputtered particles and substrate is always 90° .

The relation between the position on the substrate and the incidence angle can easily be determined with

$$\varphi[^\circ] = x \cdot \frac{360}{2\pi R} \quad \text{Eq. 3.10}$$

where x is the position on the substrate and R is the distance substrate/center of the pinhole (in this case 10 mm).

The disadvantage of the cylindrical substrate holder is the need for flexible substrates, like transparent slides, which are limiting the possible methods of surface analysis.

With the vignetting function $V(\varphi)$, $\Phi(\varphi)$ can be calculated from $T(x)$ of a cylindrically shaped substrate according to:

$$\Phi(\varphi) \propto \frac{T(\varphi(x))}{V(\varphi)} \quad \text{Eq. 3.11}$$

where $\varphi(x)$ is a linear function for a cylindrical substrate (Eq. 3.10).

Aside from cylindrical substrates, also planar substrates were used. They were necessary, since the flexible substrates needed for the cylindrical substrate holder prohibit certain surface analysis techniques (e.g. thickness profile determination of

oxides; see below). Compared to the cylindrical substrate, planar substrates do have the disadvantage that the distance between pinhole and substrate is angle dependant, and that the incidence angle on the substrate is not perpendicular anymore.

For planar substrates $T(x)$ can be converted into $\Phi(\varphi)$ according to

$$\Phi(\varphi) \propto \frac{T(\varphi(x))}{V(\varphi) \cdot \cos^3(\varphi)} \quad \text{.Eq. 3.12}$$

The difference to the cylindrical substrate is a factor of $\cos^{-3}(\varphi)$, which is caused by two geometric reasons. First the coated area is tilted towards the particle flux, thus reducing the deposition rate by a factor of $\cos(\varphi)$, and the distance pinhole to substrate increases with the angle, thus decreasing the deposition rate by $\cos^2(\varphi)$. The dependence between angle and substrate position is given by

$$\varphi = \arctan\left(\frac{x}{R}\right) \quad \text{Eq. 3.13}$$

where x is the position on the substrate and R is the distance substrate/center of the pinhole (in this case 10 mm).

As substrates for the planar holder, microscope slides were used for metallic layers and polished single crystal silicon wafers for dielectric layers. The substrate holder of the MFMplan configuration is capable of holding flat substrates with a maximum length of 40 mm and a width of 20 mm. The distance between holder and orifice is 11 mm (at a substrate thickness of 1 mm, the distance substrate-orifice amounts to 10 mm). A mask is included to prevent the coating of a part of the substrate, which is needed as reference. The substrate holder of the MFMZ configuration has the same properties, except that the maximum length was 22 mm.

3.3 Thickness Determination

The MFM converts the information of the angular distribution of the metal flux into a thickness profile of a substrate behind the pinhole. It was therefore necessary to find methods capable to determine this thickness profile with good accuracy and lateral resolution. On the other hand the thickness determination must not be too time consuming nor expensive, because of the desired high experimental throughput. Two different methods were used, as the deposited layer can be metallic or dielectric. If a metal film is deposited, its thickness can be measured using the absorption of light. For dielectric layers, the thickness is measured using the interference of light.

3.3.1 Metallic Layers

Thin metal layers are decreasing the intensity of a passing light ray exponentially [109] according to the equation (Beer-Lambert law)

$$T = \frac{I}{I_0} = e^{-\alpha d} \quad \text{Eq. 3.14}$$

where T [%] is the transmission, I_0 and I are the initial and the weakened light intensities, respectively, d [nm] is the film thickness and α [nm^{-1}] is the extinction coefficient. When a ray passes several materials (e.g. substrate and coating), the transmission T is a product of the transmission through the substrate T_s and the transmission through the metal T_m . Therefore T_m can be expressed as

$$T_m = \frac{T}{T_s} \quad \text{Eq. 3.15}$$

And the thickness of the metal can be expressed according to Eq. 3.14 as

$$d = -\frac{\ln(T_m)}{\alpha} \quad \text{Eq. 3.16}$$

Therefore, the determination of the thickness requires a known extinction coefficient α , either from literature [110] or by experimental determination, and the measurement of T_s .

3.3.1.1 Experimental procedure

To measure the transmission, a commercial slide scanner model Reflecta CrystalScan 7200 with a maximum resolution of 7200dpi (= 2835 dots per cm; pixel length 3.5 μm) was used. A slide frame with the glass removed served as the sample holder. The scanning software was Silverfast AFL-SE from LaserSoft Imaging. It supports the 48bit HDR (High Dynamic Range) format that allows obtaining the raw scan data without any adjustments. This is of importance, since in this format the information from the CCD chip of the scanner represents the true light intensity. The image (initially a RGB image) was color split to the RGB channels in Paint Shop Pro 6, because only one of the three colors was used for the analysis. Green (550 nm) was chosen, as it is in the center of the visible spectrum. The blue and red images were discarded. The image with the information from the green channel, with each pixel having a brightness value (B) between 0 and 255 was then opened with Digital Micrograph from Gatan to finally register the brightness values of the pixels.

It should be noticed, however, that owing to the imperfection of the CCD chip of the scanner, the maximum value of 255 is not automatically registered if there is no object between the light source and the CCD chip. The same holds for the the minimum of 0 if the light path is completely blocked. Therefore, in order to determine the true values, scans were made with no objects between light source and the chip for the absolute transmission (white; $T = 1$) and with a completely covered scan area for zero transmission (black; $T = 0$). The maximum value for the green channel is 249.45 (B_w) for white and the minimum 0.97 (B_b) for black. The real transmission of the scanned object can then be described as:

$$T = \frac{(B - B_b)}{(B_w - B_b)} \quad 3.17$$

The transmissions of coated substrates were measured with the method described above, in order to determine the extinction coefficient for Cu and W. First the transmission of an uncoated transparent substrate was measured to determine T_s . Then the transmission of several samples with known but different coating thicknesses of the used metal was measured and plotted. This graph was then fitted with a curve of an exponential function in Microcal Origin to get the extinction

coefficient α , which was finally determined experimentally to be $6.02 \times 10^{-2} \text{ nm}^{-1}$ for Cu and 0.151 nm^{-1} for W.

As the extinction coefficient is known, the thickness profile of the coated substrates from the MFM can be determined. After deposition, the substrates are scanned with the following settings:

Format: 48 bit HDR tiff format

Resolution: 900 dpi (= 35.4 pixels per mm → pixel length 28 μm , which corresponds to 0.16° for MFM1d, which is higher than the physical resolution of the MFM)

The scanned images (*figure 3.8*) are then analyzed with the procedure described above. To obtain the brightness values for each pixel, the program digital micrograph was used.

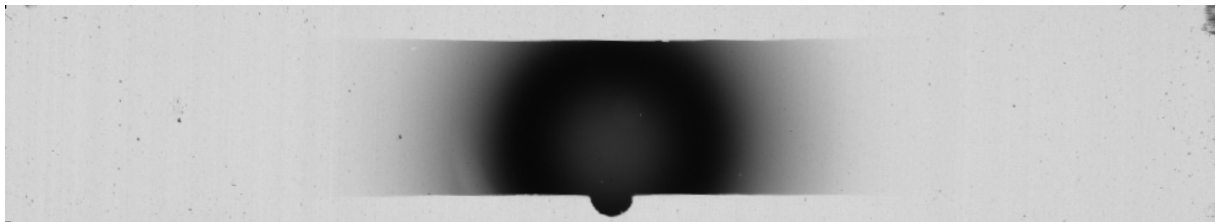


Fig.3.8: Greyscale image of the transmission (green) values of the scanned substrate. The small semicircle at the bottom is created by a small notch on the bracket which holds the substrate to mark the middle of the sample.

3.3.2 Dielectric Layers

As the oxidization of some deposited films was unavoidable, and also films deposited in a reactive atmosphere should be characterized, it was necessary to find a suitable method to determine the thickness profile of dielectric layers. There are commercially available methods like confocal microscope, spectro-photometers, or spectroscopic ellipsometers, but none of these meet all the desired requirements. These are e.g. the desired spatial resolution (ellipsometers or spectrometers) or that the method would be too expensive and time consuming. Therefore a novel method had to be developed to determine the thickness profile of these films.

When the dielectric layers are deposited on a reflective substrate (silicon wafer) the interference patterns are clearly visible. It was therefore obvious to image these interference patterns with a digital camera to evaluate the thickness profile. Due to the fact, that this novel method was developed and modified in the whole duration of

the project, the different states of development will be described here. As this method proved to be flexible, powerful, and reliable, it can be seen as a spin-off of the project.

3.3.2.1 Theoretical model

The physical theory used to describe and calculate this problem is the model of “two beam interference” on a thin and coplanar film. Multiple reflected beams are neglected (assumption: their intensity is too low) as well as the slopes present in the film (usually only 100 nm over several mm). The problem can be described as a superposition of two beams with the same wavelength but with different amplitude and phase (due to the different optical path-length, see *figure 3.8*).

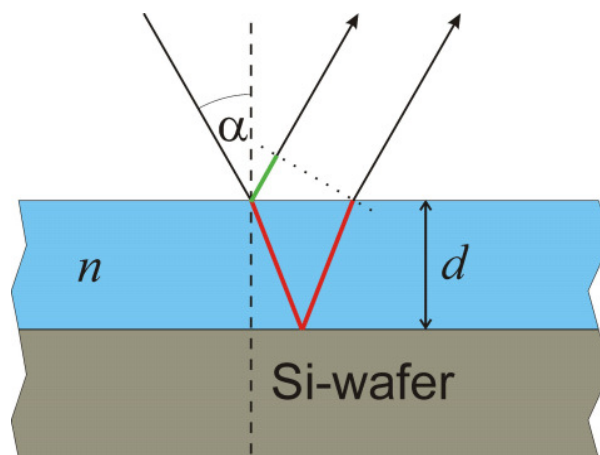


Figure 3.8 Two beam interference. The phase shift is due to the different optical path-length between the beam that is reflected at the interface air-layer (green) and the beam which is reflected at the interface layer-substrate (red).

The difference in the optical path-length Δs , with the law of refraction already included, is:

$$\Delta s = 2d\sqrt{n^2 - \sin^2 \alpha} \quad \text{Eq. 3.18}$$

where d is the thickness, n is the refractive index, and α is the incidence angle.

The difference of the phase $\Delta\varphi$ for a given wavelength λ is:

$$\Delta\varphi = \frac{2\pi\Delta s}{\lambda} = \frac{4\pi d\sqrt{n^2 - \sin^2 \alpha}}{\lambda} \quad \text{Eq. 3.19}$$

There is also a phase jump of π at reflections on materials with higher refraction index, but both beams are reflected once at a material with higher refraction index

compared to the medium they emerge from, therefore there is no additional phase shift.

Interference is simply a superposition of two beams with their wave functions B_1 (Eq. 3.20; the one reflected at the air-layer interface) and B_2 (Eq. 3.21; reflected at the Silicon Surface).

$$B_1(t) = a_1 \cdot \sin(\omega t) \quad \text{Eq. 3.20}$$

$$B_2(t) = a_2 \cdot \sin(\omega t + \Delta\varphi) \quad \text{Eq. 3.21}$$

with a_x being the amplitudes of the wave functions, ω the frequency and t the time.

The superposition of those beams yields the beam with the wave function B (Eq. 3.22) and the Intensity I (Eq. 3.23).

$$B(t) = \sqrt{a_1^2 + a_2^2 + 2a_1a_2 \cos(\Delta\varphi)} \cdot \sin(\omega t) \quad \text{Eq. 3.22}$$

$$I = |B(t)|^2 = a_1^2 + a_2^2 + 2a_1a_2 \cos(\Delta\varphi) \quad \text{Eq. 3.23}$$

As the amplitude of the wave function is not easily accessible, it is substituted by the maximum intensity I_{max} (constructive interference) and the minimum intensity I_{min} (destructive interference) of the reflected beam.

$$\begin{aligned} I_{max} &= a_1^2 + a_2^2 + 2a_1a_2 \\ I_{min} &= a_1^2 + a_2^2 - 2a_1a_2 \\ \frac{I_{max} - I_{min}}{2} &= 2a_1a_2 \\ \frac{I_{max} + I_{min}}{2} &= a_1^2 + a_2^2 \end{aligned} \quad \text{Eq. 3.24}$$

With the substitution of the amplitudes with I_{max} and I_{min} Eq. 3.23 can be written as

$$I = \frac{I_{max} + I_{min}}{2} + \frac{I_{max} - I_{min}}{2} \cdot \cos\left(\frac{4\pi d \sqrt{n^2 - \sin^2 \alpha}}{\lambda}\right) \quad \text{Eq. 3.25}$$

Finally, the thickness d can be expressed as a function of the intensity I :

$$d = \arccos\left(\frac{2I - (I_{\max} + I_{\min})}{(I_{\max} - I_{\min})}\right) \cdot \frac{\lambda}{4\pi\sqrt{n^2 - \sin^2 \alpha}} \quad \text{Eq. 3.26}$$

In our special case, where the normalized profile of the thickness is important and not the total value of the thickness, the second term of the equation (the fraction with λ , n and α) is of minor importance, as it just a constant factor. The profile of the thickness, and thus the associated angular distribution is solely defined by the term which contains the arccosine. The arccosine itself has the disadvantage that it is the inverse of a periodic function, and thus not unequivocally defined. The range of the usual principle value is limited to $\{0 \text{ to } \pi\}$, but actually it can have multiple values (e.g. $\arccos(0) = \pi/2$; but also $3\pi/2$; $5\pi/2$; $7\pi/2$). Eq. 3.27 has therefore to be expanded to:

$$d = \left\{ m\pi + \frac{\pi}{2} (1 - (-1)^m) + (-1)^m \arccos\left(\frac{2I - (I_{\max} + I_{\min})}{(I_{\max} - I_{\min})}\right) \right\} \cdot \frac{\lambda}{4\pi\sqrt{n^2 - \sin^2 \alpha}} \quad \text{Eq. 3.27}$$

with m being a natural number $\{0, 1, 2, \dots\}$ called the order. As the determination of the order m is not trivial, it will be explained in the next chapter by means of an example.

The procedure of thickness determination itself can be briefly described as follows. To capture the intensity of the reflected light, and I_{\min} and I_{\max} as well, requires an uncoated area of the substrate next to the strip of the coated substrate, where the thickness profile should be determined. The intensity of the light reflected from the coated surface is divided by the intensity from the uncoated substrate (called reference) for each color channel (RGB-splitting). This has the advantage that most errors, like uneven lightening, are cancelled out at the beginning. There is also no need for a special light source. The thickness profile is then determined for each color separately, just for the determination of the order m , the profiles of the three colors are compared to each other.

Theoretically, the interference patterns could also be imaged with the transmission scanner. Unfortunately in this case the refractive index of the transparent substrates and the deposited dielectric layers are quite similar. Just a small amount of intensity is reflected at the substrate-layer interface, which causes a very bad signal to noise ratio.

3.3.2.2. Original procedure to determine the thickness profile of a dielectric layer

As stated above, the experimental setup to determine the thickness profile using the interference patterns was continuously developed during the project. In this section the first and most simple setup will be described, along with the procedure of the data analysis. Although the setup itself was very basic, the results were in good agreement with measurements conducted with a profilometer. This proves that the method itself is very stable and reliable.

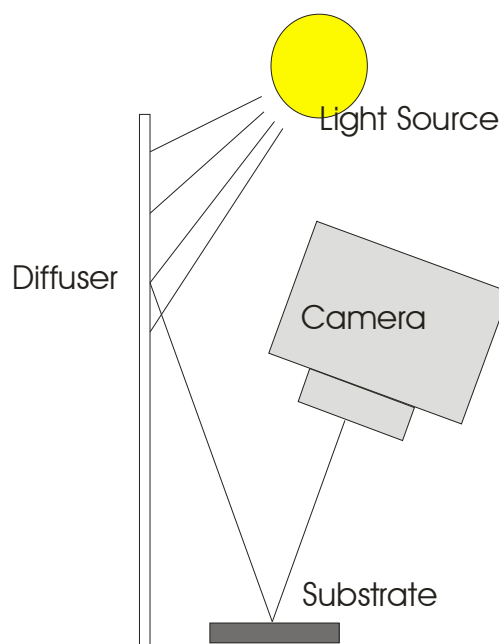


Figure 3.9 Lay-out of the first experimental setup to capture the interference patterns.

As shown in the lay-out of the experimental setup for measuring the film thickness on the substrate, presented in *figure 3.9*, a light ray passes 4 stations:

a) Light Source: The exact spectrum of the light source is not relevant for the calculation of the film thickness, since each color is analyzed individually. Therefore the intensity distribution in the spectra is no criterion for the choice of the light source (although it should not have too great differences in the intensity of each color). On the other hand it is advantageous if the light is emitted from a larger area and if the lighting conditions are easy reproducible for comparison. A circular shaped fluorescent lamp was used for the first measurements.

- b) Diffuser: The diffuser is very important, because the camera actually captures a reflection of the diffusers surface due to the high reflectivity of the substrate. A perfect diffuser would be white with no texture and high diffuse reflectivity. Also the diffuser should be evenly lighted. A sheet of white paper is sufficient for this purpose.
- c) Substrate: The interference colors are created on the surface as described above.
- d) Digital Camera: After experimenting with different cameras, an Olympus Stylus 760 was used. The camera was mounted on a small tripod; the distance objective to sample was 97 mm and the tilt angle between camera and substrate was 20° (where 0° means that the camera looks normal onto the substrate surface).

The technical specifications of the camera are:

- Image pickup device: 1/2.33" CCD (primary color filter), 7,380,000 (gross)
- Lens: Olympus lens 6.5 to 19.5 mm, 3.4 to 5.7

The following camera settings were used:

- Flash: off.
- Image Quality: SHQ 3072x2304 Low compression (JPEG)
- Color adjusting: Auto
- ISO Sensitivity: AUTO or 80
- Super Macro mode (allowing shooting range down to 8 cm)
- Self timer

The photographs (example *figure 3.10*) are saved as a jpeg file.

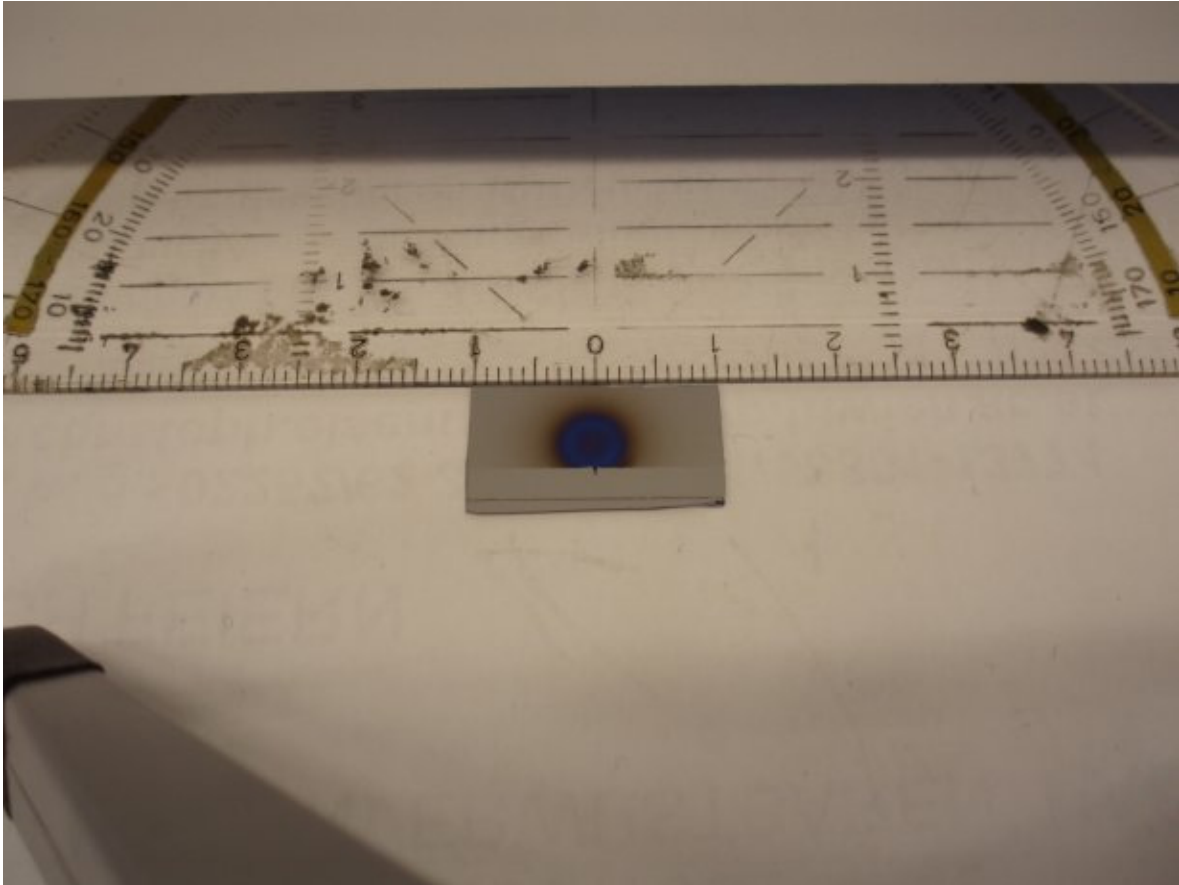


Figure 3.10 Photograph of a sample used for measurements of the thickness profile. The sample has been sputtered 1h30min with aluminum at 0.5 Pa at a discharge current of 0.3 A. The image is color-split into three color channels (blue, green, and red) with “paint shop pro 6” and the picture of each color channel is saved as a grayscale bmp image (*figure 3.11*).

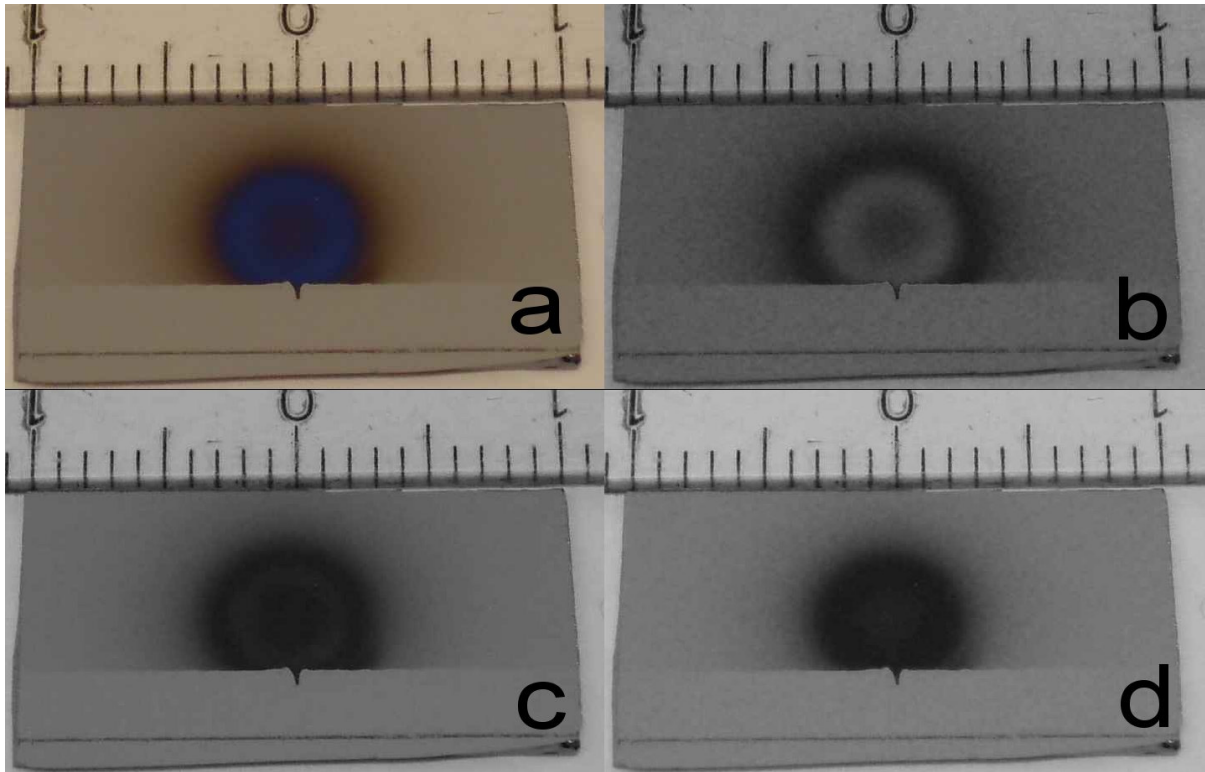


Figure 3.11 Detail of fig. 3.10 a) The RGB image; b) grayscale image of the blue channel; c) grayscale image of the green channel; d) grayscale image of the red channel

Afterwards each image is opened with DigitalMicograph from Gatan. A profile with a length of 630 pixels in the x axis is then taken through the middle of the dielectric film (which has a spherical symmetry); the given value for each point was the mean value of 20 pixels in the y axis. The same profile is taken from the uncovered Si-Surface beneath the covered area and then smoothed for the use as a reference. The profile of the film is then divided by the smoothed reference. It should have values between 1 (the reflectivity is as high as the uncoated Si surface) and 0 (no reflected light at all). Each step is shown in *figure 3.12*

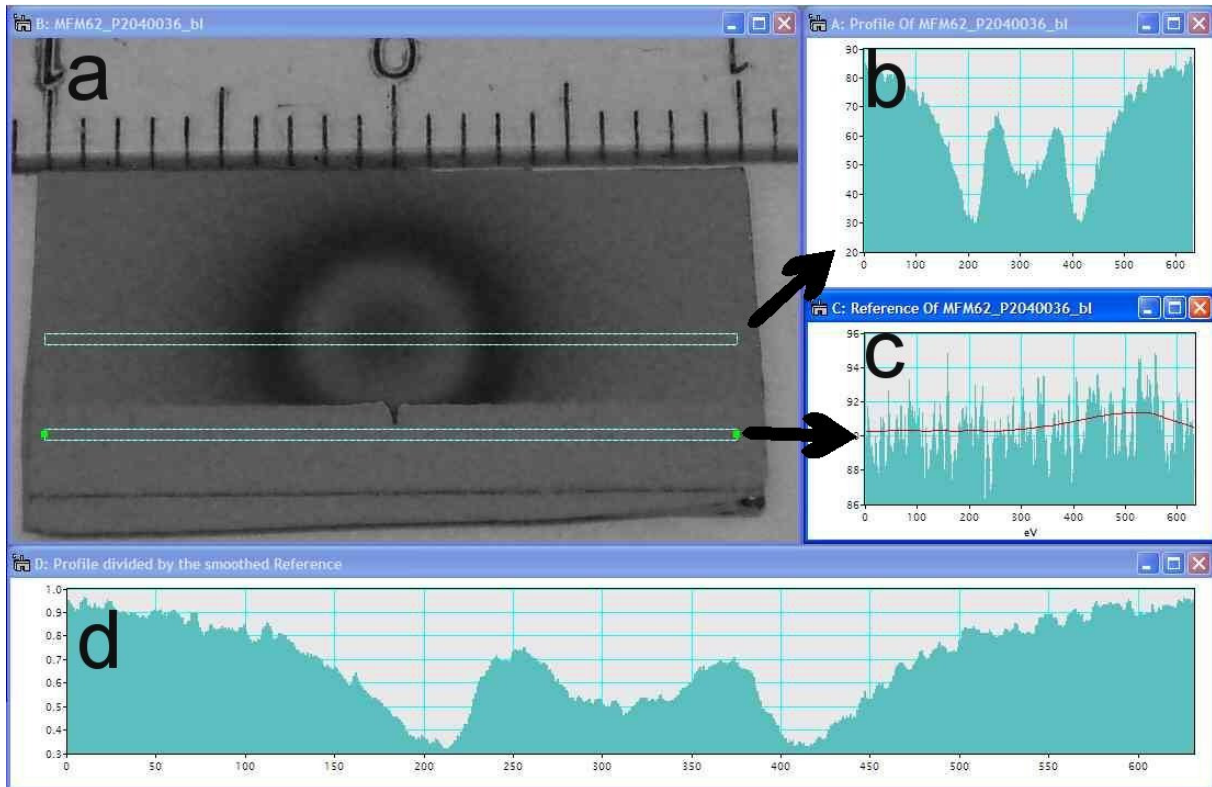


Figure 3.12 Method for reading the profile information with digital micrograph: a) the image (blue channel) with the marked areas of the two profiles. The upper one is the profile of the film; the lower one is the reference. b) The profile of the film. c) The reference measurement (the line-plot is the smoothed reference). d) The profile of the film divided through the smoothed reference. This data is taken for further thickness determination.

The advantage of this method is the canceling out of numerous error sources, such as uneven lighting, uneven color brightness or the necessity of a special lamp (needed for a defined spectral distribution), since each profile is corrected by its own reference.

The profile is then exported to a Microsoft excel sheet, where the thickness of each point is calculated with Eq. 3.27 using following values:

- I_{max} : Actually, two values can be used for I_{max} . For interference with $m = 0$ (thickness between 0 and the first minimum), I_{max} is 1, the reflectivity of the uncoated substrate. For higher order ($m \neq 0$), I_{max} can be greater than 1 (maximum measured value used, can be up to 1.1). This effect is caused by the fact, that the reflectivity at constructive interference can be higher than the reflectivity of the uncoated substrate.
- I_{min} : If a minimum exists, the lowest value is taken. If there is no minimum available, the value should be taken which gives the same thickness

information for a color where a minimum is available (it often happens that there is no minimum for the red channel, but one for the blue channel)

- n : As mentioned above, the exact value of n is not needed for normalized profiles. To give an idea of the film thickness, the following approximated values have been used: 1.75 (Al_2O_3); 2.8 (TiO_2); 1.35 (MgO). The reason why the values are called approximated is that the refractive index of a sputtered film and the crystalline bulk material may be different.
- λ : 450 (blue); 550 (green); 650 (red)
- α : 0.34906585 rad (20°)

The location of each point is determined as follows:

When the profile from DigitalMicrograph is exported to Excel, the values are written in one column. Then each point is given a location (x -axis) from -315 to 315. The real position on the substrate can be calculated with

$$x(\text{mm}) = \frac{x(\text{pixel}) \cdot \text{length}(\text{mm})}{\text{length}(\text{pixel})} \quad \text{Eq. 3.28}$$

where the length of the substrate is 20.5 mm in the experiment and the image extension is 660 pixels (these values are changed if the settings of the camera or its position towards the substrate are changed).

If the intensity profile is converted into a thickness profile, neglecting the order of the interference (hence using Eq. 3.26) the obtained profile information shown in *figure 3.13*.

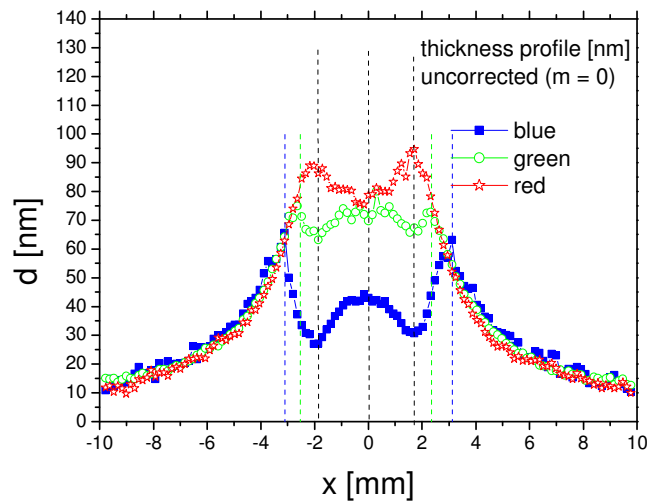


Figure 3.13 The thickness profile of the sample. The blue profile has an intensity minimum (therefore a thickness maximum) at ± 3 mm (blue dashed lines) and the green profile at ± 2.5 mm (green dashed lines). The extreme values at ± 1.8 mm and ± 0 are present in every color channel (black dashed lines). Therefore they represent genuinely existing topographic information of the film.

To evaluate the order for every m , the following algorithm is used. For our samples, the boundary condition is clear, as the thickness should be close to zero at higher angles, therefore m can be set to 0 at the boundaries. This algorithm is used for each color channel individually. m starts with 0 and increases by one for each non-topographic extreme value that has been passed. To distinguish whether an extreme value of I is caused by a change in the order or by a topographic extremum, the different color channels are compared to each other. When an extreme value occurs in just one channel, it is caused by a change of the order. If this extreme value occurs in every color channel at the same position, it is caused by a topographic extremum. It is therefore necessary for this algorithm, that more than one wavelength is used. This is demonstrated by means of the blue channel. At $x = \pm 3$ mm, the extreme value is just observable in the blue profile, thus it must be a change of the order m . At $x = \pm 1.8$ mm and ± 0 mm, the extreme value is observable in each channel, therefore these are caused by a topographic extremum. The m value between $+3$ mm and -3 mm is therefore set to 1, everywhere else it is 0. The effect of this expansion in Eq. 3.27 is that when m increases by 1, every following point will be mirrored by a line through the point where this step happens first. The result of this procedure can be seen in figure 3.14.

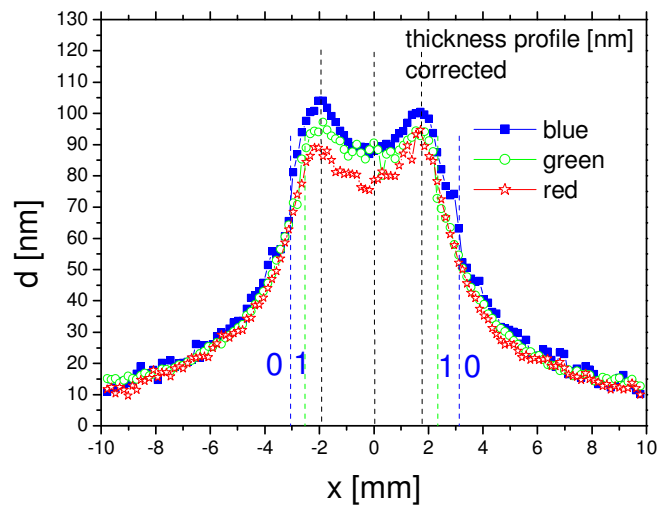


Figure 3.14 The identical profile presented in figure 3.14, with the difference that the change in the order m was accounted for. The boundary of the order is indicated for the blue profile.

The last step is to average the profiles of the three color channels (figure 3.15).

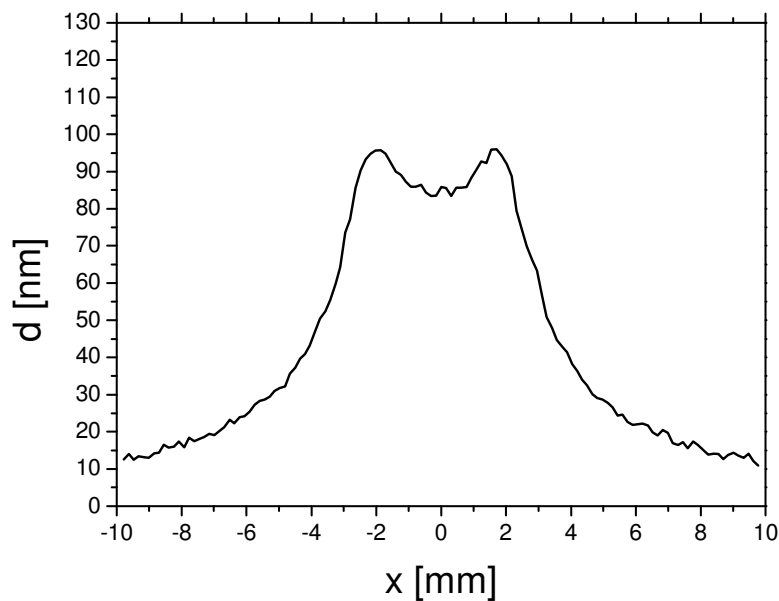


Figure 3.15 Average of the three profiles of the different colors.

As the described method to measure the thickness profile of a dielectric film was novel, it was necessary to verify the obtained results. The measurements to verify the obtained results were conducted by a Taylor/Hobson Surtronic 3+ Profilometer with the following method. The profiles taken by the profilometer were normal to the edge of the film (figure 3.16a) and the height of the step (= film thickness at this position)

was measured (figure 3.16b). This was done several times at each position, in order to be able to average the values. This procedure was repeated each 0,5 mm and the single values were composed to the final thickness-profile (which is perpendicular to the step). The settings of the profilometer were: horizontal range 1.25 mm; vertical range 10 μm ; vertical resolution 10 nm (practical resolution 40 nm, as steps below this value cannot be identified). This procedure was conducted for 13 samples in total and a general deviation of 10% of the optical data to the profilometric data could be observed. An example is given in *figure 3.17*.

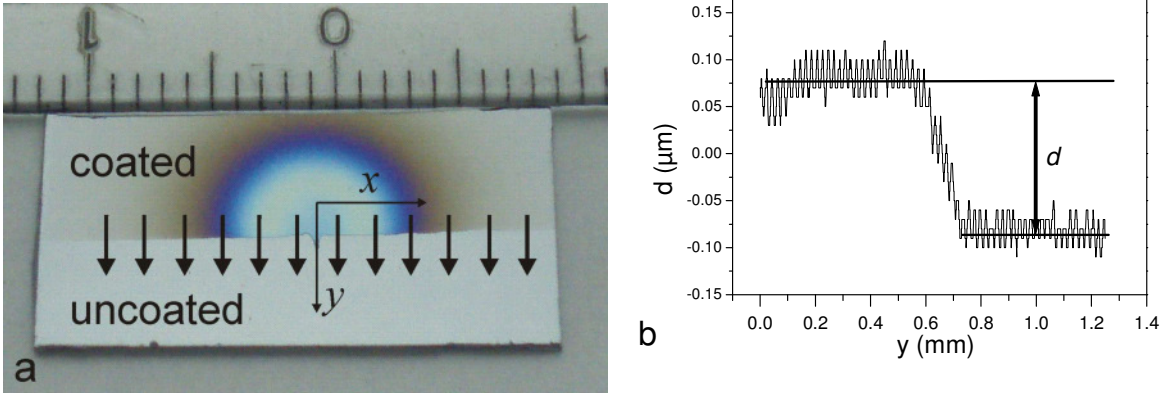


Figure 3.16 a) The profiles along the arrows (perpendicular to the edge; y - axis; from coated to uncoated area) were measured for several x -positions. b) Example of a profile; the film thickness d is equal to the step height.

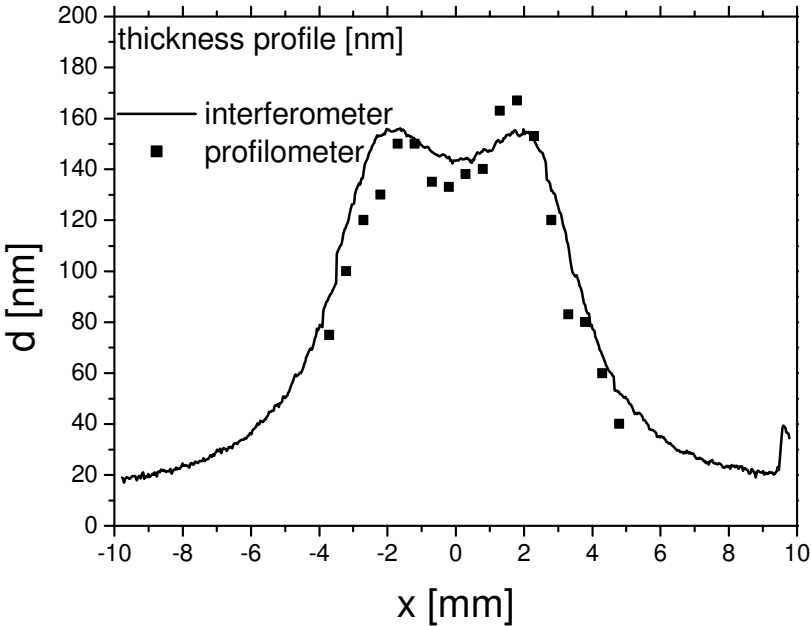


Figure 3.17 Comparison of the results of a thickness profile obtained by the interferometer method and by a profilometer. The two measurements are in good agreement.

As the two described methods depend on very different physical properties (optical vs. mechanical), this can be seen as a good verification of the described interferometric method, especially considering its simple experimental setup. Nonetheless, there are some errors that may occur due to the simplicity of the presented interferometric setup. For example, the illumination conditions change for each measurement. This may cause an offset of 10 to 20 nm, when the measured strip is slightly under-illuminated, compared to the reference strip. This offset had to be removed manually. Another problem of the first setup was that it was hard to keep the geometric properties (like distance camera to substrate) constant.

Additionally, measurements with XPS were conducted to evaluate the stoichiometry of a deposited alumina layer. The O/Al ratio of the sample (measured at different positions on the film) was found to be 1.655 with a standard deviation of 0.082. This proves that the deposited layer is fully oxidized to Al_2O_3 . Therefore the thickness profile of the deposited oxide layer is equivalent to the profile of the impinging metal flux. If the stoichiometry would be position dependant, a qualified statement of the metallic flux, concluded from the profile of an oxide layer, would not be possible.

3.3.2.3 Refined setup

As the interferometric method described above proved to be effective, a prototype of a refined experimental setup was build (*figure 3.18*) where all components were mounted on an aluminum ground plate. Additional transparent diffusers were added to have a more evenly lighted reflective diffuser. As a camera a Canon Powershot G9 is used, which is connected to a computer. The device itself is covered by a box (not shown in the *figure 3.18*) to prevent any interference from outside. Additionally, the parts of the device are covered with black felt to absorb strayed light.

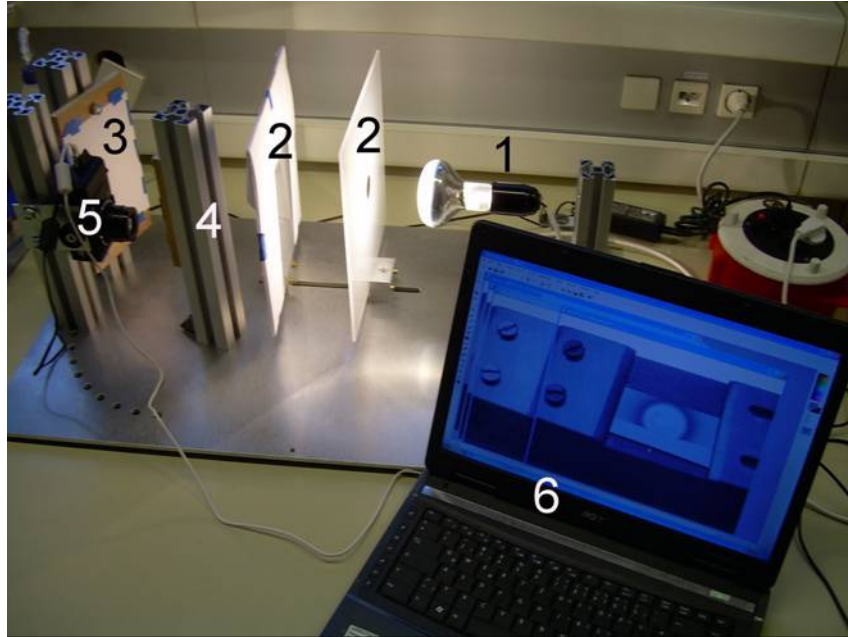


Figure 3.18 Prototype of the refined setup. 1: Lamp; 2: transparent diffusers 3: reflective diffuser; 4: sample holder; 5: camera (Canon PowerShot G9); 6 Notebook.

Beside the experimental setup, the analysis of the obtained data was improved by expert software which offers features like semi-automatic detection of the flipping points (figure 3.19).

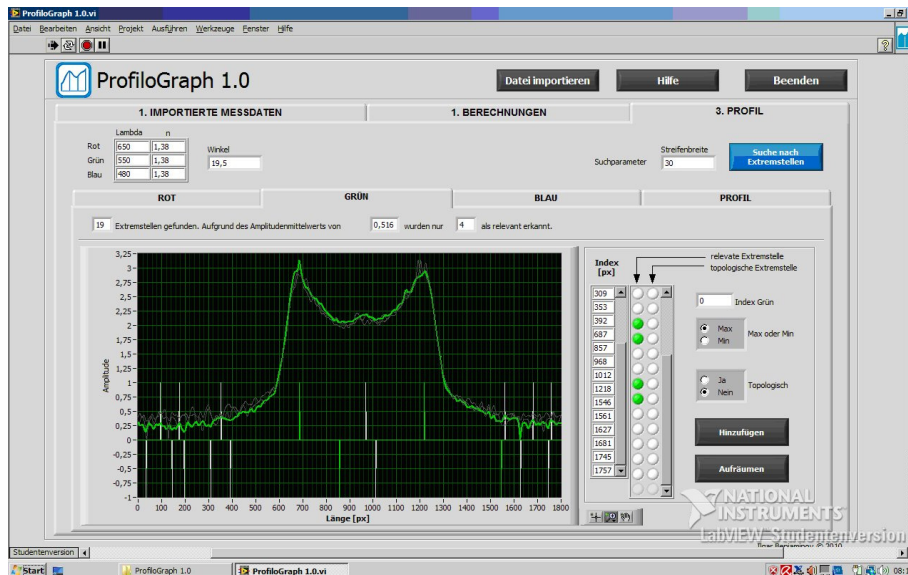


Figure 3.19 Screenshot of expert software.

The device was further developed and additional features were added which are beyond the scope of this thesis, but still worth to be mentioned. E.g. it is shown in literature [111, 112] that the thickness and the refraction index of a thin film can be simultaneously determined by rotating the sample. Therefore a $\theta/2\theta$ cog wheel gear was added to the setup (figure 2.20).

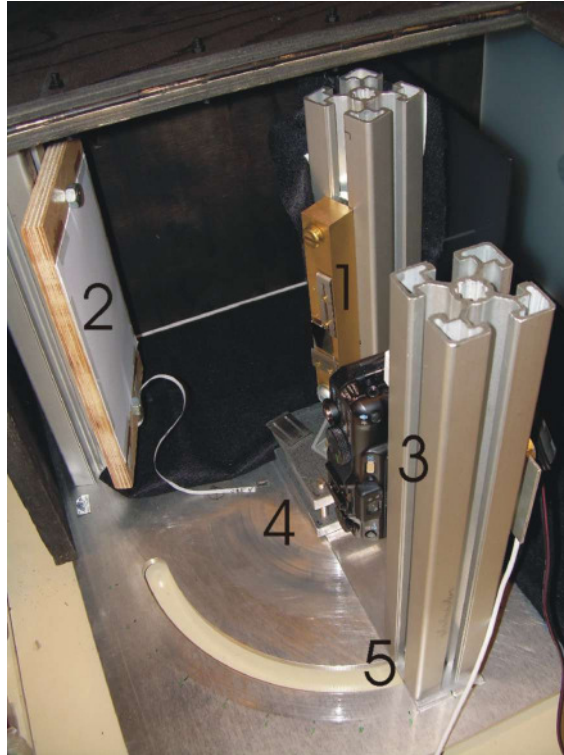


Figure 3.20 Final setup with moveable camera for adjusting the angle of incidence. 1: sample holder; 2: reflective diffuser; 3: camera; 4: cog wheel; 5: camera holder for adjustable tilt.

Unlike the method described in literature [112] which uses a spectrometer with a large spectral band width, the device described here is limited to the three wavelengths determined by the used camera. d and n can still be determined simultaneously by fitting the measured intensities with Eq. 3.30 (figure 3.21). Despite the simplicity of the setup and the use of consumer electronics, measurements showed that a good match can be achieved (see table 3.2). This method is still under development and additional features, like an automated fitting process will be implemented in the future.

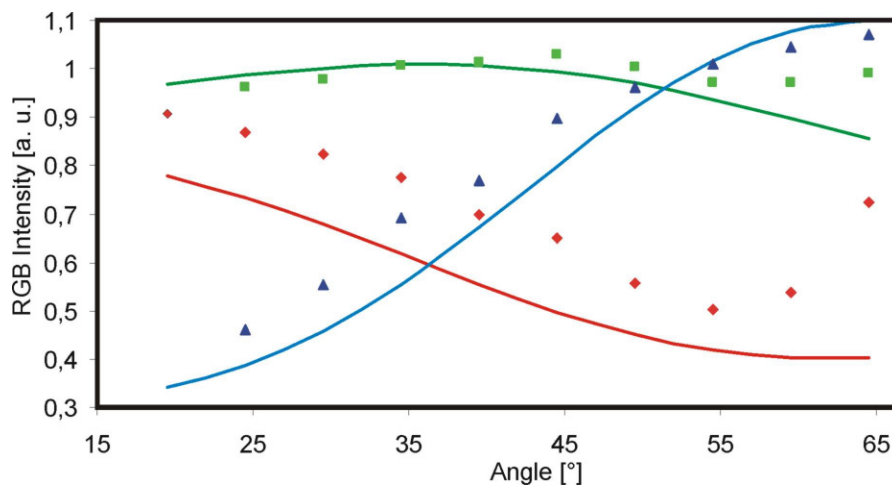


Figure 3.21 RGB intensities fitted by a two beam interference model (400nm SiO_2 on Si).

	measured value	reference value
d	400 +/- 5 nm	400 nm
n	1.52 +/- 2 nm	1.55

Table 3.2 Comparison of measured values to reference values

4 Simulation of the angular distribution

As stated in the introduction, the measurement of the angular distribution of the metal flux serves two purposes. First, it is a fundamental parameter for the simulation of the growing film. Second, it is influenced by vital parameters of the sputtering process, like the nascent angular distribution of the sputtered particles, the distribution of the local erosion rate on the target, and the scattering during the gas phase.

In this section it will be described, how these parameters influence the angular distribution of the metallic flux, and how the angular distribution can be simulated or calculated. By comparing the experimental results with the calculated or simulated data, the parameters which exert the main influence on the angular distribution can be evaluated. To determine these influences, two different approaches are used. One being a MC simulation, the other one being an analytical/numerical method.

4.1 MC Simulation SIMTRA

The metal flux towards the flux monitor was simulated using the MC-code SIMTRA [31], which tracks a representative set of individual particles in their movement through the vacuum chamber. The working principle is as follows: first a sputtered particle is generated with initial position, energy and direction, sampled from given distribution functions. Here the ejection positions were taken from a measured erosion profile, neglecting the small influence of the target material on the racetrack shape. The initial energy distribution resulted from simulations using the binary collision code SRIM [113] with a constant incident ion energy corresponding to 75 percent of the discharge voltage [33, 114]. Although SRIM also provides the nascent angular distributions, these did not reproduce the typical heart-like shape observed experimentally [48, 115-118]. Hence, as described in [31], nascent angular distributions for Cu, Al and Ti were reconstructed from deposition measurements instead, using the transport code in a reverse way. For W, on the other hand, having no data available, the SRIM nascent angular distributions were used. For Mg, a nascent angular distribution according to Eq. 2.2, with $\beta = -0.1$, was estimated. However, considering the geometry of the experimental setup, this parameter was expected and found to have only a limited influence when used for a planar target.

SIMTRA uses a nascent angular distribution according to

$$Y(\theta) \propto \sum_{i=1}^5 c_i \cos^i(\theta), \quad \text{Eq. 4.1}$$

with the following factors (*table 4.1*)

	c_0	c_1	c_2	c_3	c_4	c_5
Cu	0	2.55276	-10.8812	28.9098	-29.943	10.03786
Al	0	2.573	-10.415	29.899	-34.696	13.152
Ti	0	3.1798	-2.016665	-4.53936	6.18887	-2.42589

Table 4.1 Factors for the nascent angular distribution used by SIMTRA

In the next step of the model the collisional transport of the sputtered particle through the gas phase is described. The background gas was assumed to be homogenous at a temperature of $T = 350$ K and specified pressure p . The assumption of a homogenous temperature distribution is valid, since the heating of the gas [119] and

gas rarefaction [75, 76] are negligible at pressures below 1 Pa. Collisions were modeled based on either quantum chemical (Cu-Ar, Al-Ar [73]) or screened Coulomb interaction potentials. Also the thermal motion of the background gas atoms was included. The sticking coefficient at the substrate was assumed to be unity.

The simulated configuration mimicked the experimental set-up, including the inside of the metal flux monitor. The angular distribution can be directly constructed from the particles arriving at the pinhole. By continuing to track the particles through the MFM and following the experimental procedure, i.e. calculation of the deposition profile and applying the vignetting correction, it is possible to estimate the influence of scattering in the flux monitor and the angular error due to the aperture.

To simulate the pinhole camera the option “with substrate on backplane” was used. With this option, all important data of every individual particle hitting a defined area (which is simulating the pinhole) are recorded. In a second simulation, which simulates the inside of the MFM, the file containing these data is then used as the particle source. A separate simulation of the events outside the MFM and inside the MFM has the advantage, that different pressure inside and outside the MFM can be simulated, thus simulating a differentially pumped MFM.

Since the pinhole geometry drastically reduces the deposition rate, a large number of particles had to be generated ($> 10^9$; maximum is 2^{31}) to have a statistically significant amount of particles contributing to the thickness profile. If still an insufficient amount of particles is reaching the substrate, due to disadvantageous parameters like a high pd product, the pinhole radius is doubled. In this case, the geometric dimensions when simulating the inside of the MFM are doubled as well, and the pressure is halved to contain the same pd product.

4.2 Analytical/numerical simulation

Neglecting gas phase scattering, the angular distribution of the metallic flux can be calculated analytically, taking into account the geometry, position, and orientation of the target, the local erosion rate $E(R)$, and the differential sputter yield $Y(E, \theta)$.

4.2.1 Geometric considerations

To investigate the influences of the geometry, like orientation and distance, we will take a look at the particles which pass the pinhole at an angle φ , with an infinitesimal solid angle of $d\Omega$.

The first important geometric parameter is the distance from the center of the pinhole to the target r . It is known, that the particle density radiating from a point (or an infinitesimal target element) decreases with r^2 . On the other hand, the radiating area viewed by an infinitesimal solid angle $d\Omega$ increases with r^2 (see *figure 4.1*), thus increasing the number of particles in this infinitesimal solid angle $d\Omega$ by r^2 . Overall, these two effects cancel out each other. The intensity for an infinitesimal solid angle $d\Omega$ is not influenced by the distance from the target surface.

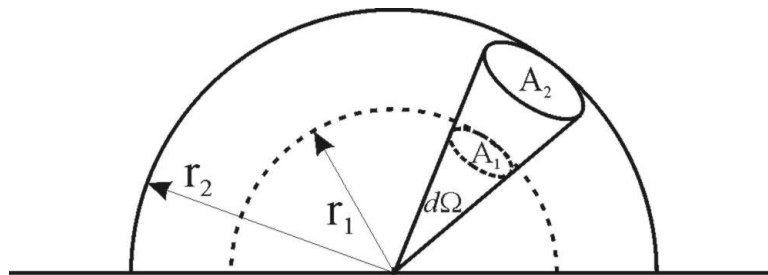


Figure 4.1 The area viewed by an infinitesimal solid angle $d\Omega$ increases with r^2 .

As mentioned above, gas phase scattering is neglected in these assumptions. Gas phase scattering decreases the intensity of the sputtered particles according to the Keller-Simons formula (Eq. 2.25).

The second geometric factor is the orientation of the radiating area towards the pinhole. If the target area is tilted by an angle θ , the area element dA viewed within the infinitesimal solid angle $d\Omega$ is increased by the factor $\cos^{-1}(\theta)$. Thus the intensity of $d\Omega$ would increase by $\cos^{-1}(\theta)$. An interesting effect can be observed, when the nascent angular distribution of the ejected particles is equal to $\cos(\theta)$, which is the

first approximation for magnetron sputtering. In this case the particle intensity is independent from the orientation of the target towards the pinhole (*figure 4.2*). This effect is also known in optics as the equal brightness effect of a Lambertian surface.

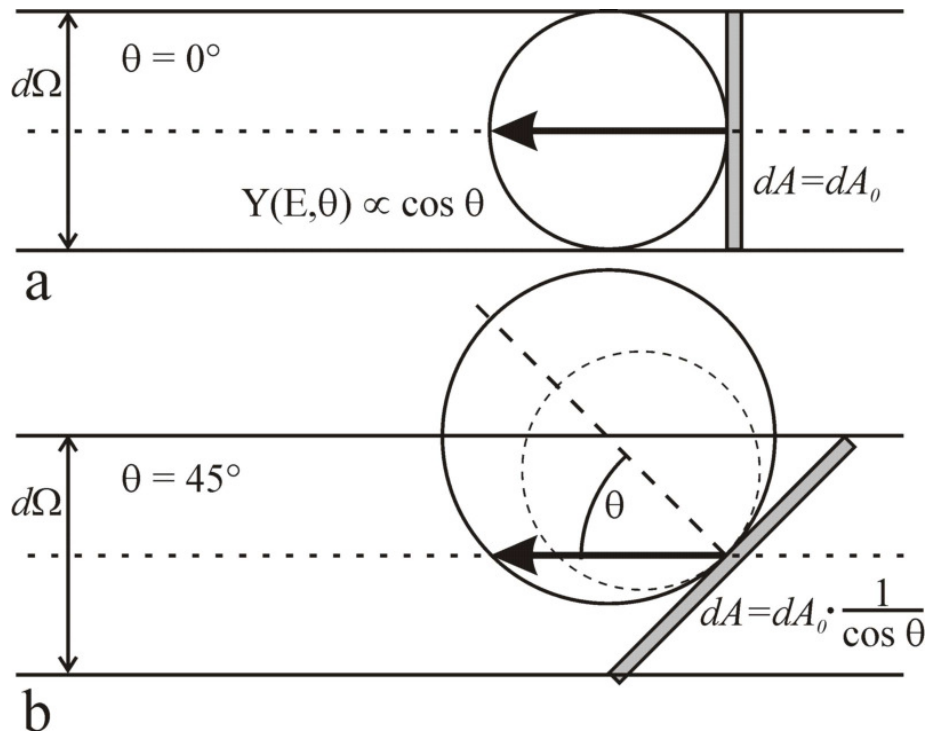


Figure 4.2 Influence of the orientation of the target towards the substrate with the assumption of a cosine nascent angular distribution.

4.2.2 Analytical simulation of the angular distribution for basic target geometries

For simple target geometries, like circular planar targets or cylindrical targets, the angular distribution can be determined analytically, when gas scattering is neglected.

The case of a disk shaped planar target is imaged in *figure 4.3*.

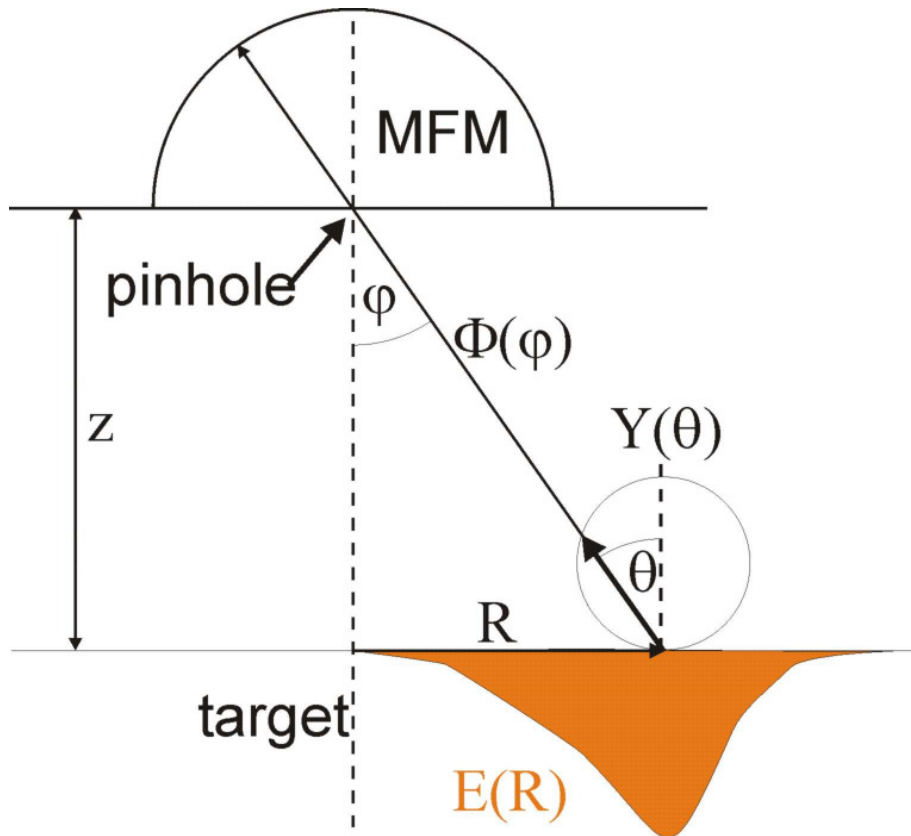


Figure 4.3 Analytical determination of the angular distribution $\Phi(\varphi)$ for a planar target. The distance target pinhole is z . The target has a symmetrical emission intensity $E(R)$ indicated by the highlighted area. The nascent angular distribution $Y(\theta)$ is considered to be cosine shaped.

The angular distribution can then be calculated according:

$$\Phi_p(\varphi) \propto E(R = z \tan(\varphi)) \cdot Y(\theta = \varphi) \cdot \cos^{-1}(\varphi) \approx E(z \tan(\varphi)) \quad \text{Eq. 4.2}$$

when the nascent angular distribution is cosine shaped in the first approximation. Even if the nascent angular distribution deviates a lot from the cosine shape, it has just a small impact, since most of the particles arrive within a narrow angular range. The angular distribution of the arriving flux is therefore mainly influenced by the shape of the erosion zone of the target.

Another possible target geometry is a cylindrical target. With a rotating magnetic system inside the target, the temporarily averaged erosion rate is completely homogenous. The geometry of this system is given in *figure 4.4*.

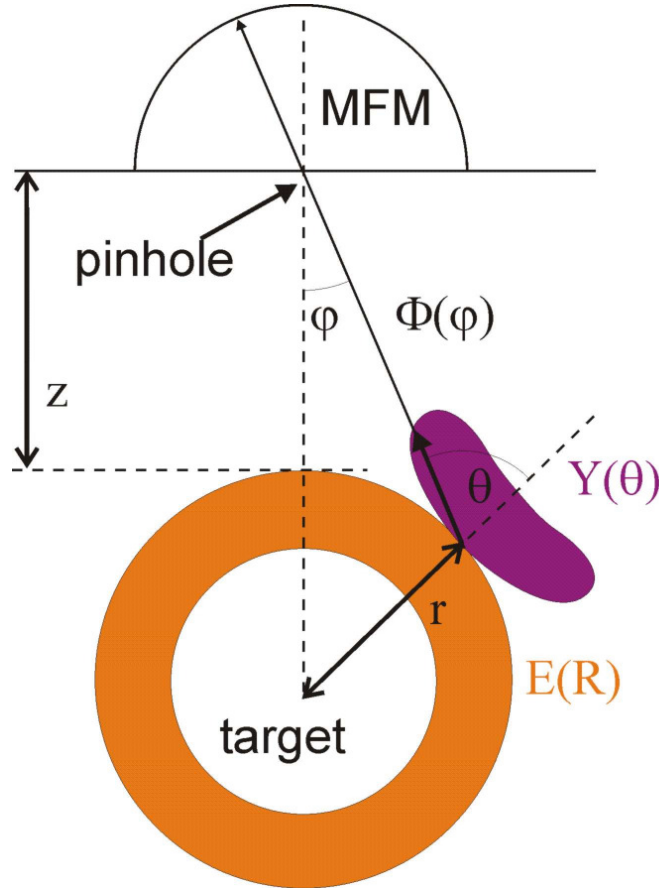


Figure 4.4 Analytical determination of the angular distribution $\Phi(\varphi)$ for a cylindrical target with a homogenous erosion rate ($E(R) = \text{const.}$). The distance target to pinhole is z . The nascent angular distribution $Y(\theta)$ is considered to be heart shaped. r is the radius of the target.

When using the relation between φ and θ

$$\frac{r}{\sin(\varphi)} = \frac{r+z}{\sin(\pi-\theta)} \Rightarrow \theta = \arcsin\left(\sin(\varphi) \cdot \frac{r+z}{r}\right), \quad \text{Eq. 4.3}$$

and constant $E(R)$ settings, the angular flux can be calculated as

$$\Phi_c(\varphi) \propto Y\left(\theta = \arcsin\left(\sin(\varphi) \cdot \frac{r+z}{r}\right)\right) \cdot \cos^{-1}(\theta), \quad \text{Eq. 4.4}$$

and $\Phi_c(\varphi)$ is therefore solely determined by the nascent angular distribution.

When $Y(\theta)$ can be expressed according to Eq. 2.2, Eq. 4.4 can be written as

$$Y(E, \theta) \propto \cos \theta (1 + \beta \cos^2 \theta) \quad \text{Eq. 2.2}$$

$$\Phi_c(\varphi) \propto 1 + \beta \cos^2\left(\arcsin\left(\sin(\varphi) \cdot \frac{r+z}{r}\right)\right) \quad \text{if } \left|\sin(\varphi) \cdot \left(\frac{r+z}{r}\right)\right| < 1 \quad \text{Eq. 4.5}$$

The results of this equation are shown in *figure 4.5* for $\beta = 0$ (cosine shaped), and $\beta = -0.5$ (heart shaped). For a cosine shaped initial distribution ($\beta = 0$, solid line) the angular distribution is a step function. For a heart shaped nascent angular distribution ($\beta = -0.5$, dashed line) the deviation at $\varphi = 0^\circ$ is given by the value of β . The angular distribution of a cylindrical target with constant $E(R)$ is therefore an image of the nascent angular distribution when gas phase scattering is neglected.

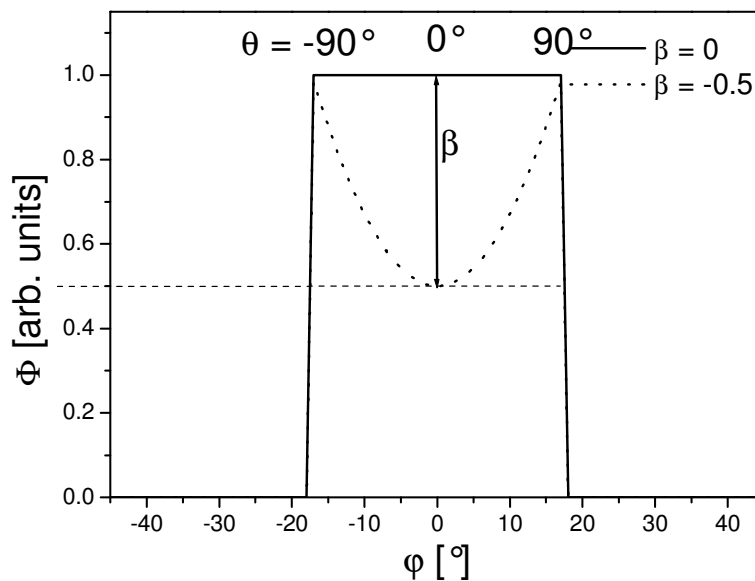


Figure 4.5 Calculated angular distribution of the metal flux from a cylindrical target according Eq. 4.4 for different β . $r = 22$ mm; $z = 50$ mm.

Other influences on the angular distribution, like the shape of the pinhole or gas phase scattering can not be included into the analytical calculation of the angular distribution easily. Therefore an additional numerical approach is needed.

4.2.3 Numerical Approach

According to the previous section, the calculated Φ_c from a cylindrical target radiating particles with a cosine shaped nascent angular distribution shows a plateau with a step like flank (*figure 4.5*), while simulations with SIMTRA at $p = 0$ Pa shows a smoother behavior at the flanks of the plateau. This is caused by the finite radius and the shape of the pinhole. The point spread function (PSF) of the circular pinhole itself, u_{pin} , can therefore be expressed as the equation of a circle with the radius $\Delta\varphi$ being the maximum angular error of 2.9° (see *table 3.1*)

$$u_{pin}(\varphi) = \begin{cases} \sqrt{1 - (\varphi/\Delta\varphi)^2} & |\varphi/\Delta\varphi| < 1 \\ 0 & other \end{cases}. \quad \text{Eq. 4.6}$$

The angular distribution $\Phi_{c,pin}$ accounting for the pinhole error can be calculated as a convolution of the initial Φ_c and the PSF u_{pin}

$$\Phi_{c,pin}(\varphi) = \Phi_c(\varphi) \otimes u_{pin}(\varphi) = \int_{-\infty}^{\infty} \Phi_c(\xi) u_{pin}(\varphi - \xi) d\xi. \quad \text{Eq. 4.7}$$

As this integral could be cumbersome, the discrete form of the convolution is more suitable

$$\Phi_{c,pin}(\varphi) = \sum_n \Phi_c(n) u_{pin}(\varphi - n). \quad \text{Eq. 4.8}$$

$\Phi_{c,pin}$ reproduces well the shape of the flanks from the simulation for a cosine shape nascent angular distribution, as can be seen in *figure 4.6*.

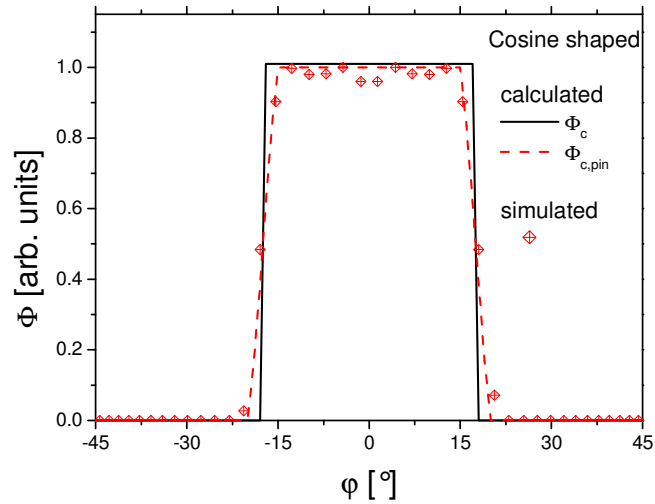


Figure 4.6 Comparison of the simulated angular distribution (with $Y(\theta) \propto \cos(\theta)$) with the calculation. $z = 50$ mm. (Φ_c is set to 1.01 in order to distinguish it to $\Phi_{c,pin}$)

As mentioned in section 2.1.1, the nascent angular distribution of the sputtered particles has a complex form and can be described by several equations, each with different fitting parameters. In the following section we will focus on two of them. First, it can be described by the polynomial model (c_i -fit) used by Simtra (Eq. 4.1) with the fitting parameters given in *table 4.1*. This model is very accurate, but cumbersome due to the large number of parameters. The second model (β -fit) is described by Eq. 2.2. It is basically a truncated version of the c_i fit with $c_1 = 1$ and $c_3 = -\beta$ (other coefficients are 0) and has the advantage that there is only one fitting parameter. In *figure 4.7*, a comparison of these two models for Ti is shown. β can be directly derived from Φ_c as the difference between the peak values and the minimum at $\varphi = 0$ and is -0.85 for Ti. This direct relation with β is not given anymore in $\Phi_{c,pin}$ as the height of the peaks shrinks due the convolution (indicated in *figure 4.7*).

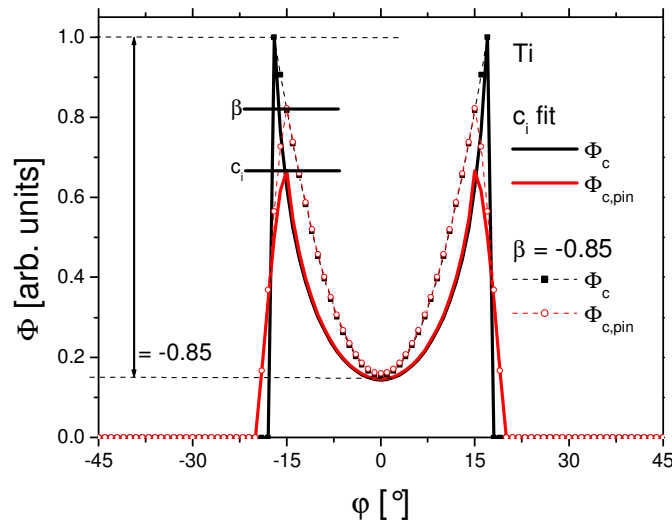


Figure 4.7 Φ_c and $\Phi_{c,pin}$ for Ti using the two models to represent the nascent angular distribution. β can be directly derived from Φ_c .

Simulations with SIMTRA (which uses c_i fit) at $p = 0$ Pa (thus neglecting scattering) were conducted and compared with the analytically calculated $\Phi_{c,pin}$ (see figure 4.8a,b). As nascent angular distributions for the calculation the c_i fit and the β fit (Ti $\beta = -0.85$; Cu $\beta = -0.5$) were used, to investigate the difference between these two possible methods. A good match between the simulated and the calculated results using the c_i fit could be observed proving that the analytical method used here is valid, since SIMTRA uses the c_i fit. The difference of the two models is only minor for Ti, while a small deviation can be observed for Cu. Therefore it can be concluded that the β fit can be used instead of the c_i fit since there is only a small deviation of the results. It should be noted that the Ti $\Phi_{c,pin}$ curve of figure 4.8a is the same as in figure 4.7, with the small difference that the Ti $\Phi_{c,pin}$ curve in figure 4.8a is normalized to unity, why the differences between c_i fit and the β fit appear to be less pronounced.

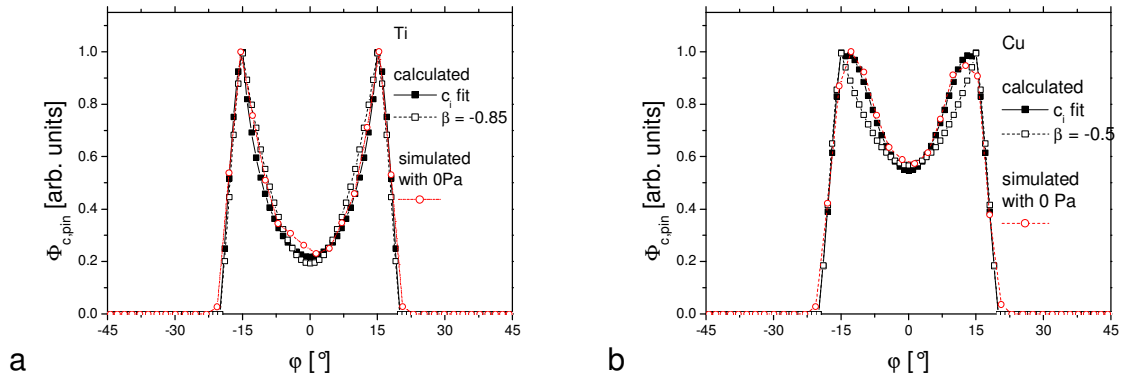


Figure 4.8 Comparison of the simulated angular distribution (at $p = 0$ Pa) with the calculation for a) Ti; b) Cu. $z = 50$ mm. The match between the simulation and the calculation using the c_i fit is very good. For Cu, a small difference of the results obtained from the two models is observable.

As it is proven that the analytical model fits well to simulations at 0 Pa, the next step is to incorporate the influence of gas phase scattering for the analytical model to calculate the experimentally accessible Φ_{cps} . When the pd product of the experiment is rather low, a basic model seems to be sufficient. It was found to be appropriate to convolve $\Phi_{c,pin}$ with a second PSF u_s with u_s being a Gaussian distribution (Eq. 4.10).

$$\Phi_{cps} = \Phi_{c,pin} \otimes u_s = \Phi_c \otimes (u_{pin} \otimes u_s) = \Phi_c \otimes u_{s+p} \quad \text{Eq 4.9}$$

$$u_s = \frac{1}{\sigma\sqrt{2\pi}} \cdot e^{-\frac{1}{2}\left(\frac{x}{\sigma}\right)^2} \quad \text{Eq. 4.10}$$

The different point spread functions are shown in figure 4.9.

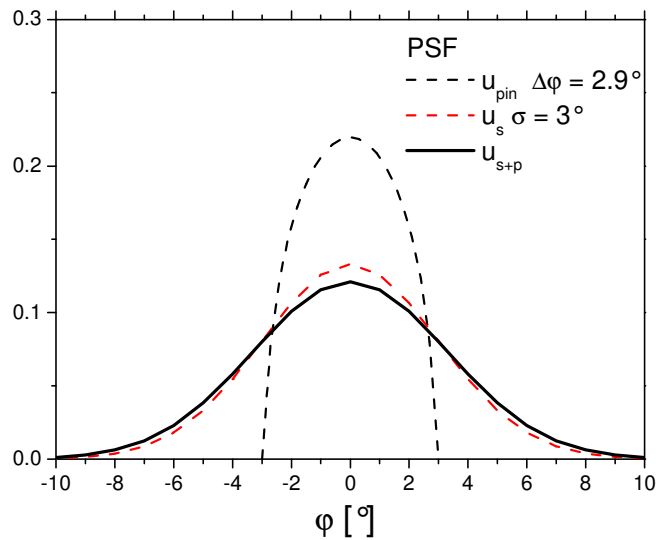


Figure 4.9 The two PSF u_{pin} and u_s and their convolution u_{s+p}

The resulting Φ_{cps} compared to the simulation is shown in figure 4.10

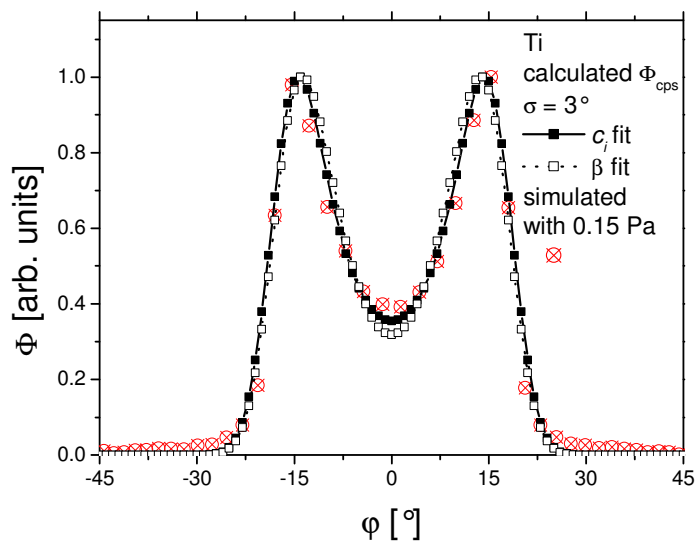


Figure 4.10 Comparison of the simulated angular distribution (at $p = 0.15$ Pa) with the calculation for Ti. $z = 50$ mm. The match between the simulation and the calculation using the c_i fit or β fit is very good.

Finally it should be noted that the pinhole error u_{pin} is caused by the pinhole itself and is therefore not actually affecting the angular distribution of the arriving flux (which is e.g. affected by gas scattering). It is included in this model as it can only be accounted for in a numerical model and thus not be included in an analytical equation.

To calculate the angular distribution of the arriving flux without pinhole error, Φ_c should be convolved with u_s instead of u_{s+p} (but according to *figure 4.9* there won't be a great difference). How this combined analytical and numerical approach can be useful will be discussed in section 6.

5 Experimental Setup

5.1 Deposition chambers

The experiments were conducted in 3 different deposition chambers (LAB I, LAB II, and LAB III). The reason for this was that different magnetron types were used, and that each chamber offered a different freedom for movement of the MFM (x or z -axis). Generally the setup of all three deposition chambers was basically the same (setup with planar magnetron sketched in *figure 5.1*). The vacuum was obtained by a high vacuum pump (either turbomolecular or diffusion pump) backed by a rotary pump. The conductance to the pump could be decreased by a valve between pump and recipient (only used for non-reactive sputtering). The base pressure was monitored via a Pirani-penning multigauge, while during the sputtering process the total pressure was monitored via a capacitance baratron gauge. The Ar gas inlet was controlled via a needle valve (non reactive only), or a mass flow controller (MKS Type 1179B 50sccm or 1259C 200sccm; controlled by a model 247c 4-channel readout). The oxygen inlet for reactive sputtering was only controlled by a MKS 1259cc mass flow controller (50sccm; 247c 4-channel readout).

The MFM was inserted via a KF40 load lock system. It consists of a pre-vacuum chamber with a separated rotary or diaphragm pump, and a gate valve. As the MFM was mounted on a quite long pipe with a linear feed-through, an important task was to align the MFM with the magnetron. An alignment of better than 1 mm could be achieved.

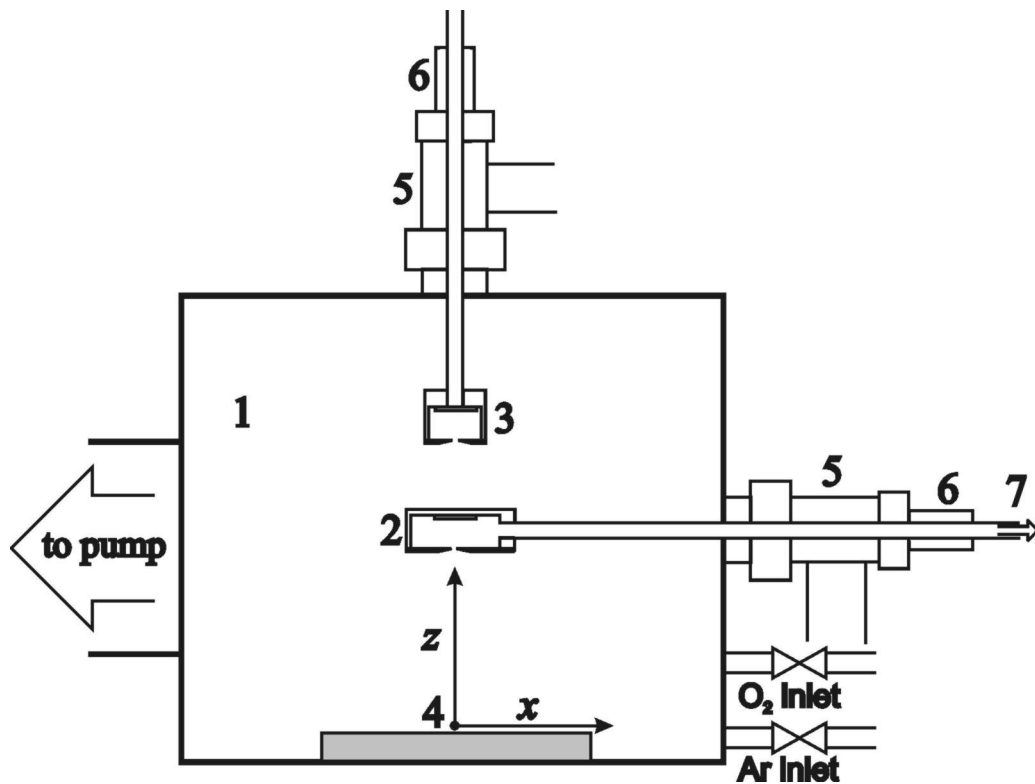


Figure 5.1: Experimental setup. Indicated parts are 1: vacuum chamber, 2: MFM (with planar substrate) movable in x-axis, 3: MFM (with planar substrate) movable in z-axis, 4: target and origin of coordinates in its centre, 5: load-lock chamber, 6: linear feed through for KF40 flange, 7: pipe of the MFM leading outside the chamber, used for differential pumping and inlet of gas into the MFM.

5.1.1 LAB I

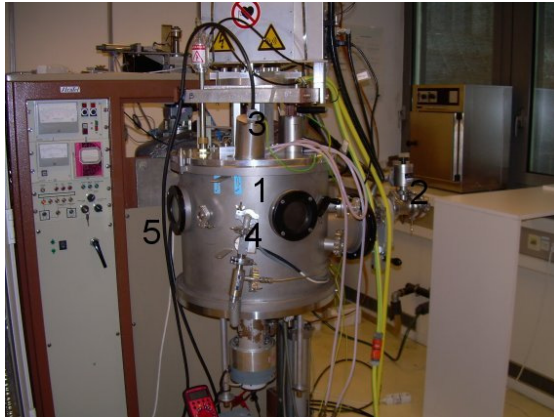


Figure 5.2: LAB I. Indicated parts are
1: vacuum chamber, 2: load lock
3-5 see table 5.1

3: Magnetrons	2 x 100 mm top 1 x 2" (50,8 mm) top
4: Gas inlet	Ar inlet via needle valve or MKS 1259C (200 sccm) flow controller (flow was slightly oscillating due to reducing armature of the Ar bottle)
5: Vacuum system	Diffusion pump (only throttled) 60 l/s MKS Baratron 690A (1 mtorr range) MKS type 270 signal conditioner

Table 5.1: Fundamental data of LAB I

The LAB I (figure 5.2, table 5.1) is a cylindrically shaped deposition chamber with a removable top. The load lock system is located at the side (thus the MFM is movable in the x -axis). A special table mechanically supports the differential pumping system of the MFM. The position of the pinhole to the target center was aligned with a plumb connected to the center of the target.

5.1.2 LAB II

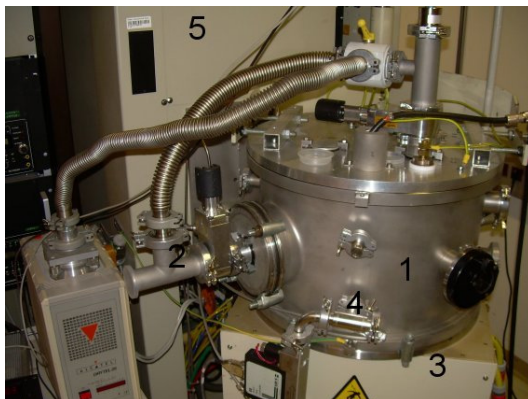


Figure 5.3: LAB II. Indicated parts are
1: vacuum chamber, 2: load lock
3-5 see table 5.1

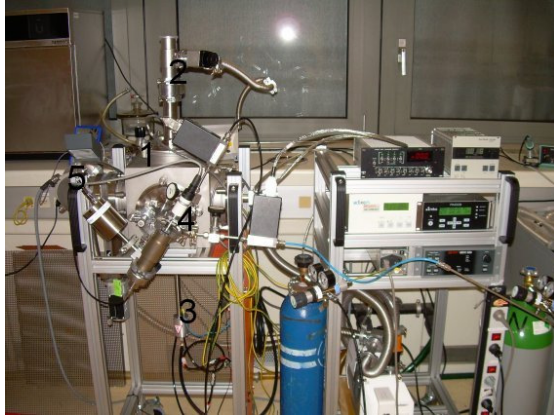
3: Magnetrons	2 x 100 mm diameter at bottom 1 x 2" (50,8 mm) bottom or side
4: Gas inlet	Ar inlet via needle valve, MKS 1259C (200 sccm) or 1179 (50 sccm) mass flow controller. O ₂ inlet via MKS 1179 (50 sccm)
5: Vacuum system	Turbomolecular pump (full) 140 l/s; (throttled) 37 l/s MKS Baratron 690A (1 mtorr range) MKS type 270 signal conditioner

Table 5.2: Fundamental data of LAB II

The LAB II (see figure 5.3, table 5.2) is a cylindrically shaped deposition chamber with removable top (like LAB I). One load lock is located above a 10 cm planar magnetron with a slight eccentricity of 5 mm. Another one is located at the side of the

chamber, opposite of the 2" magnetron. In both cases the experiments were conducted with variable z-axis distance.

5.1.3 LAB III



*Figure 5.4: LAB III. Indicated parts are
1: vacuum chamber, 2: load lock
3-5 see table 5.1*

3: Magnetrons	magnetron mounted on a KF 100 flange could be connected at every side of the chamber
4: Gas inlet	Ar inlet via needle valve or 1179 (50 sccm) mass flow controller O ₂ inlet via MKS 1179 (50 sccm)
5: Vacuum system	Turbomolecular pump (full) 68 l/s, throttled continuously MKS Baratron 627B (1 mtorr range) MKS PR4000B signal conditioner

Table 5.3: Fundamental data of LAB III

The LAB III (see *figure 5.4*, *table 5.3*) is a cubically shaped deposition chamber with 5 KF 100 flanges (one at each side, pumping system is mounted to a different flange). Due to this geometry, this chamber is very compact and flexible, as its layout (like the position of the load lock system or a magnetron) can be changed easily.

5.2 Magnetron types

As magnetron sputter deposition is used in a lot of different applications, a wide variety of different types and geometries exists. In this thesis, all experiments were conducted by DC-magnetron sputtering. For the experiments four different types of magnetrons were used (some targets are shown in *figure 5.5.*)

- cylindrical planar magnetron; diameter 2" (50.8 mm); unbalanced; Type: one AJA ST20 and one custom made by Ghent University
- cylindrical planar magnetron; diameter 100 mm; balanced
- cylindrical magnetron with rotating magnet system (diameter 45 mm)
- a rotatable magnetron provided by GHENT UNIVERSITY (diameter 50 mm)

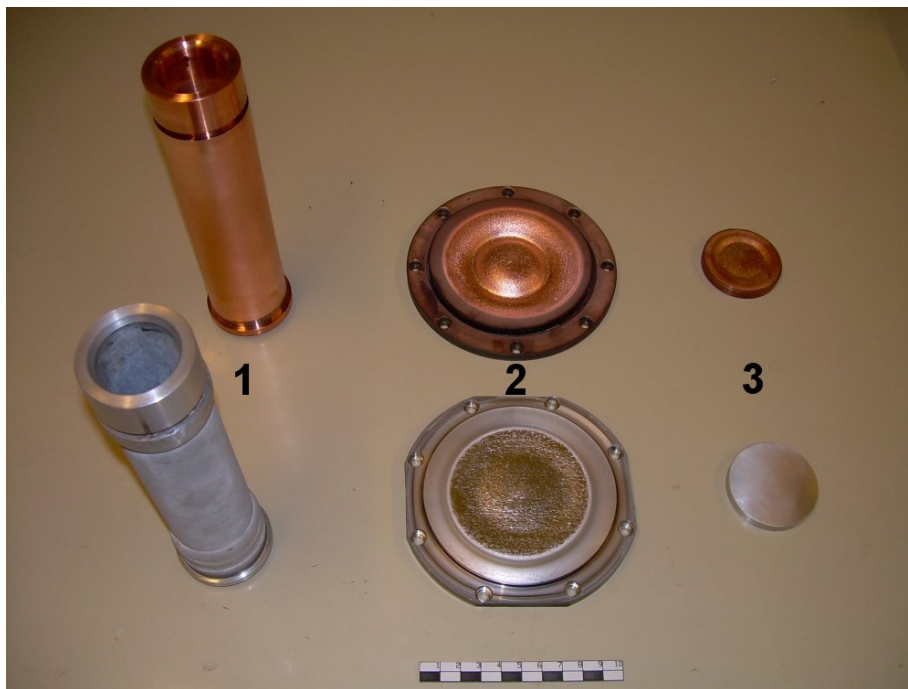


Figure 5.5: Different Al and Cu targets. 1: for cylindrical magnetron (diameter 45 mm), 2: cylindrical planar magnetron (diameter 100 mm), 3: cylindrical planar magnetron (diameter 50.8 mm)

As planar magnetrons cylindrically shaped disks with a diameter of 100 mm (for a balanced magnetron) and 50.8 mm (for unbalanced magnetrons) were used. The diameter of the racetrack (the region with the highest erosion rate) of the planar magnetrons was 46 mm (for 100 mm \varnothing), and 28 mm (for 50.8 mm \varnothing). The cylindrical magnetron had a rotating magnetic system inside, causing the plasma to circle

around the target in a confined volume. This causes the cylindrical target to be eroded uniformly. In contrast to the cylindrical magnetron, the plasma of the rotatable magnetron is static, but the target itself is rotated beneath it, thus also giving the advantage of uniform target consumption.

As the shape of the erosion rate $E(R)$ is of great importance, the erosion zone of the planar targets was determined by using optical interferometry with vertical scanning interferometry (VSI). The 3D profilometric data of a 2" Cu target is shown in *figure 5.6*.

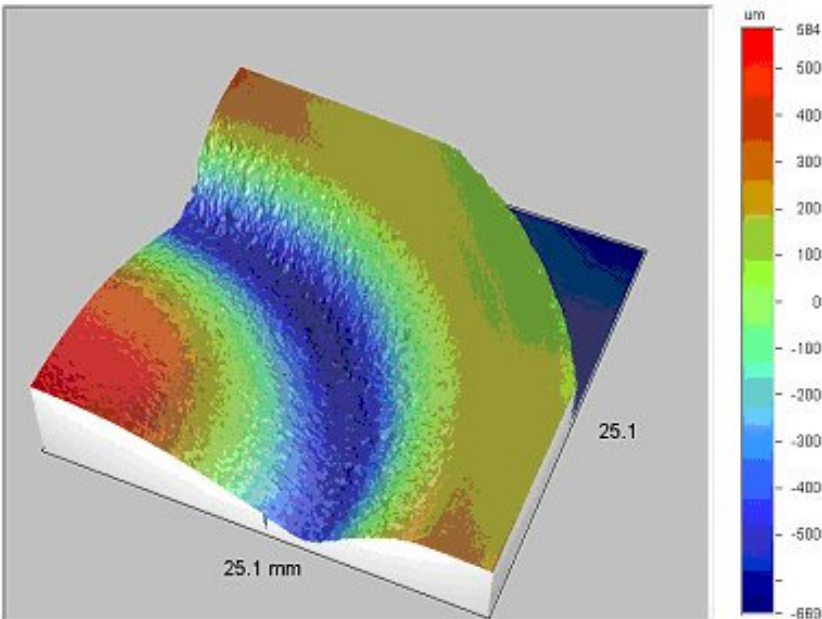


Figure 5.6: 3D image of a 2" Cu target obtained by an optical interferometer using VSI mode.

6 Results and Discussion

The experimental results of the presented work can be divided in two different categories.

First, the systematical investigation of the angular distribution of the metal flux sputtered non-reactively in pure argon. The experimental results were compared to simulations with SIMTRA, calculations with the analytical and numerical model, and the influence of the position, the pressure, and the target materials will be discussed.

Second, the influence of a controlled amount of oxygen on the angular distribution of the metal flux was determined for selected parameters. As gas phase transport during reactive sputtering is not yet well investigated, only a qualitative discussion is possible in this work.

6.1 Systematical investigation of the angular distribution of the metal flux during non reactive sputtering

The experiments were conducted for four different types of magnetrons (planar 100 mm; 50.8 mm; cylindrical; rotatable), in all 3 deposition chambers, with MFM1D (plan or cylindrical substrates) and MFMZ. To check the reproducibility of the obtained results, experiments with a defined set of parameters were conducted at the beginning, the middle and the end of a measurement series. Overall, no significant change between these experiments could be observed, thus the reproducibility of the experiments can be considered as satisfactory.

6.1.1 100 mm planar magnetron

As discussed in section 4.2.2, the angular distribution can than be approximated by Eq. 4.2

$$\Phi_p(\varphi) \propto E(R = z \tan(\varphi)) \cdot Y(\theta = \varphi) \cdot \cos^{-1}(\varphi) \approx E(z \tan(\varphi)) \quad \text{Eq. 4.2}$$

It is basically an image of the emission distribution $E(R)$, blurred by gas phase scattering. The nascent angular distribution $Y(\theta)$ has only a minor influence on the angular distribution of the arriving metal flux.

The angular distribution of the metal flux from a cylindrical planar magnetron (balanced, diameter 100 mm, racetrack diameter 46 mm) was determined systematically in order to investigate the influences of pressure, lateral position and distance for different materials. The test parameters are presented in *table 6.1*. The discharge current was kept constant at 0.3 A.

The experimental results were compared with simulations using SIMTRA, and an article on this subject was recently published by the author of this work [120].

Material	p [Pa] ($x = 0$; $z = 95$ mm)	x-positions [mm] ($p = 0,5$ Pa, $z = 95$ mm)
Cu	0.3; 0.5; 0.7; 1; 3	0; 11; 23; 35
W	0.3; 0.5; 0.7; 1; 3	
Al	0.3; 0.5; 0.7; 1	0; 11; 23; 35
Mg	0.1; 0.3; 0.5; 0.7; 1	0; 11; 23; 35
Ti	0.3; 0.5; 0.7; 1	0; 11; 23; 35
z-distances [mm] (eccentricity $x = 5$ mm; $p = 0,5$ Pa)		
Cu	25; 50; 95; 125; 150	

Table 6.1: Parameters of the experiments. pd product ranges from 10 – 300 Pa mm. Thus the experiments were conducted in the intermediate or high pressure regime.

Cu and W were deposited as metallic layers. Al, Mg and Ti were deposited as dielectric layers, owing to their higher reactivity with oxygen and the resulting oxidation during deposition.

During the experiments with Al, Mg, and Ti the MFM was also differentially pumped with a turbomolecular pump (pumping speed 60 l/s), to increase the mean free path inside the MFM, and to eliminate the residual gas. However, simulations with SIMTRA indicated, that differential pumping has only limited influence on the angular distribution. Since differential pumping complicates the test array, and reduces its flexibility, the subsequent experiments with Cu and W were carried out without differential pumping.

Figures 6.1 a-e present the influence of the deposition pressure on the angular distribution $\Phi(\varphi)$ of W, Cu, Ti, Al and Mg on substrates positioned at $z = 95$ mm and $x = 0$ mm. The results were normalized by the area beneath the curves. Experiments were conducted in LAB I. The calculated angular distribution is plotted for W with neglected gas phase scattering ($p = 0$ Pa). *Figure 6.1* distinctly shows the broadening of the angular distribution with increasing pressure, which is predicted by theory and by the simulations with SIMTRA. With some exceptions, this trend depends also on the choice of target materials, as the lighter elements are on the average scattered over larger angles, which leads to an increase of the fraction of the flux arriving at higher incident angles. A good parameter to quantify the amount of gas scattering is the ratio R_{min}/R_{max} of the local minimum at the centre of the target and the maximum at the racetracks (indicated in *figure 6a* for 0.3 Pa). For $p = 0$ Pa the R_{min}/R_{max} value

would be 0, since no particles are sputtered from the center of the target. For a completely isotropic angular distribution of the arriving metal flux the R_{min}/R_{max} value would be 1. It can therefore be considered that this value is correlated to the amount of scattering during the gas phase transport. In general a good match can be observed, except for Mg. Here, the simulation underestimated the scattering of the particles. The experiment with $p = 3 \text{ Pa}$ was not simulated due to the high computation time.

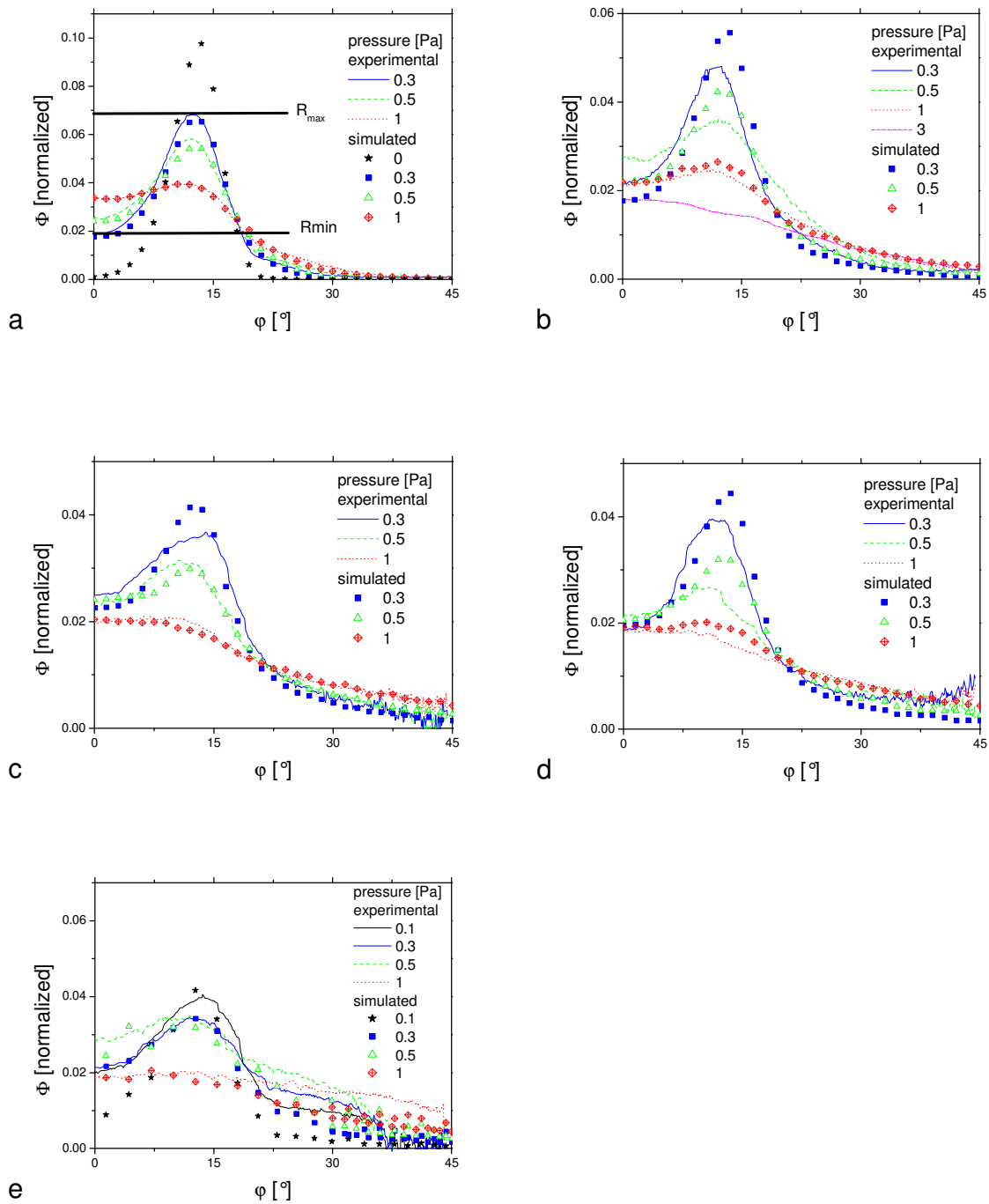


Figure 6.1: Angular distribution $\Phi(\varphi)$ of the metal flux at a substrate 95 mm above the target surface as function of the discharge pressure for a) W, b) Cu, c) Ti, d) Al, e) Mg. For W the angular distribution at $p = 0$ Pa (no gas phase scattering) is also shown.

Figure 6.2 shows the influence of the x (lateral) position on the angular distribution of the arriving metal flux for Cu at an Ar pressure of 0.5 Pa as example. The experiments were conducted in LAB I. The angular distribution shifts and becomes asymmetric. Other materials showed the same behaviour. Although the effect is mainly geometrical, an accurate quantification can help in improving for instance the

uniformity of films deposited under conditions were the arriving angular distribution influences the microstructure. Again, the experimental results match the results obtained with SIMTRA.

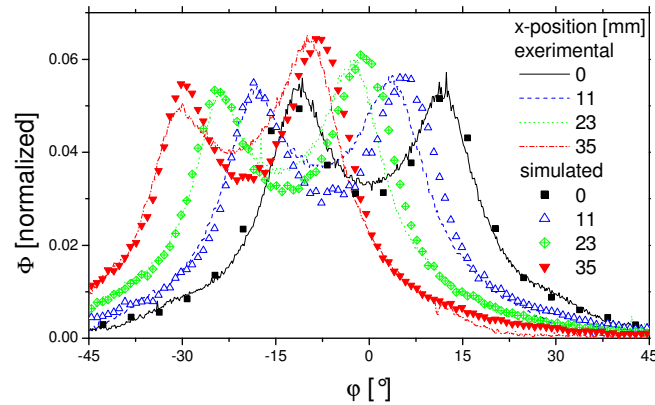


Figure 6.2: Angular distribution $\Phi(\varphi)$ of the metal flux at a substrate 95 mm above the target surface as function of the x (lateral)-position for Cu sputtered at a pressure of 0.5 Pa.

The results of the series with different z -distances (conducted in LAB II, with a constant lateral eccentricity $x = 5$ mm) are provided in Figure 6.3 with the MC-simulation for comparison. As expected, R_{min}/R_{max} increases with the distance due to the blurring of the maxima and minima by increasing the number of scattering events.

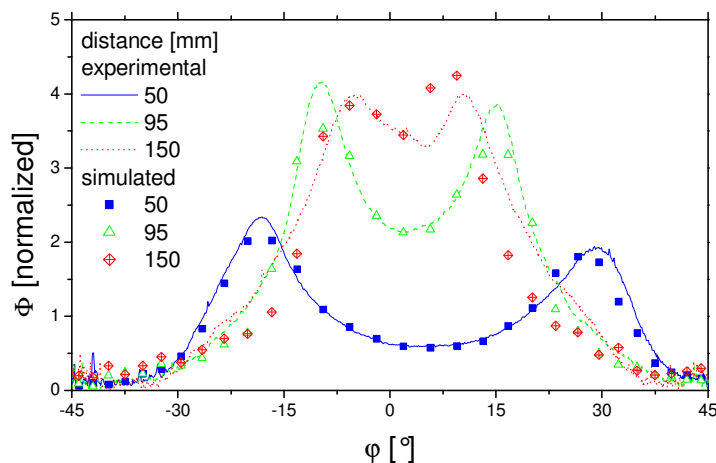


Figure 6.3: Angular distribution of copper as function of the distance z of the substrate from the target. Pressure $p=0.5$ Pa, $x=5$ mm (eccentricity).

As mentioned above, the ratio of R_{min} to R_{max} is a useful parameter for quantifying an angular distribution. A comparison of this parameter (figure 6.4a for variable pressure

and figure 6.4b for comparison pressure distance) with the degree of thermalization provided by Eq. 2.19 showed a good match. This indicates that this parameter can be used to estimate the energy loss or the average number of collisions. Simulations of the energy loss and the degree of thermalization performed by SIMTRA did not confirm the results obtained by Eq. 2.20, because the model of Eq. 2.20 is a simple analytical approximation. W best fits the continuously slowing down approximation used by Eq. 2.20, as it is the heaviest investigated material. Nonetheless, the relation between the parameter R_{min}/R_{max} to energy related values (energy loss, degree of thermalization, number of collisions) is a topic of current research.

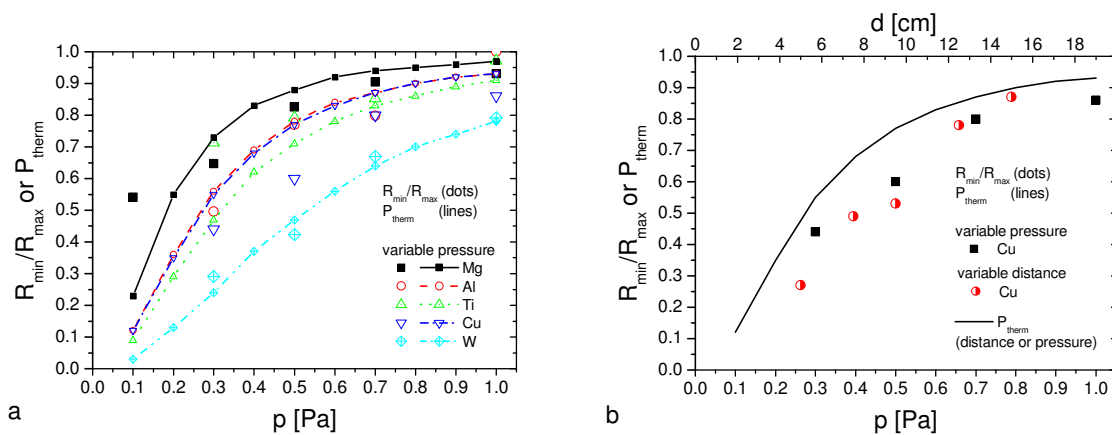


Figure 6.4: Comparison between R_{min}/R_{max} (observed) and P_{therm} (calculated) for all investigated target materials at a) different deposition pressures and materials and b) for Cu with variable distances or pressures. The magnetron had a diameter of 100 mm.

In some experiments, artifacts could be observed, whose origin remains unknown. These artifacts are ring shaped areas of lower density (see figure 6.5). The center of the ring is somewhat eccentric to the center of the angular distribution. These artifacts just occurred with the 100 mm Cu target. Their occurrences and position was erratical. It is unknown to the author which physical effects may cause these artifacts.

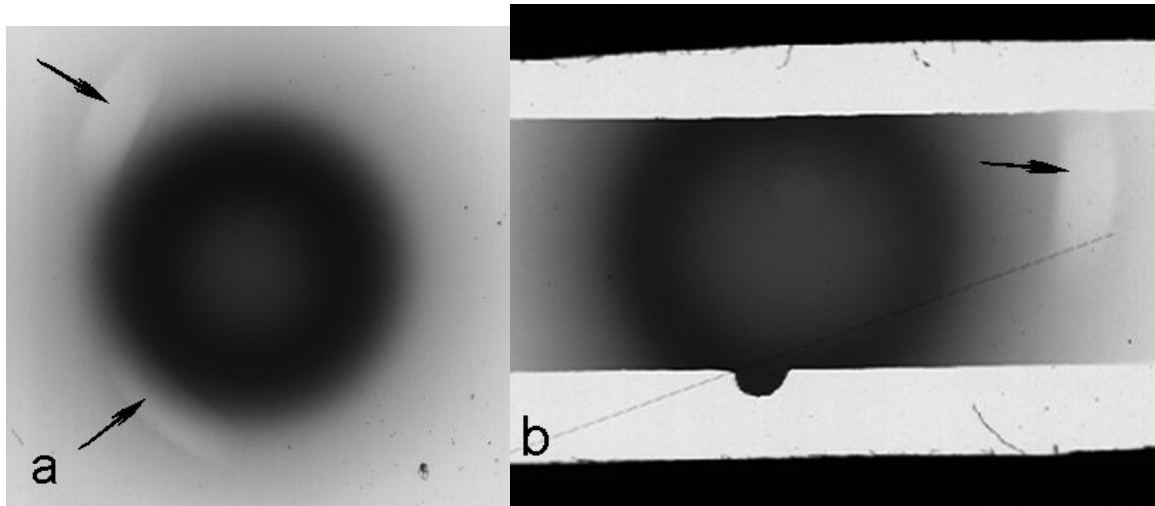


Figure 6.5 Ring shaped artifacts (indicated by arrows) on some coated substrates. These artifacts occurred just for Cu.

6.1.2 2" Magnetron

Another test series for the angular distribution of the metal flux was carried out with the 2" unbalanced magnetron in LAB II. It is basically the same as the 100 mm magnetron described in the previous section (section 6.1.1), beside that the magnetron is smaller (thus different $E(R)$) and unbalanced. As discussed in section 4.2.2, the angular distribution can than be approximated according to Eq. 4.2

$$\Phi_p(\varphi) \propto E(R = z \tan(\varphi)) \cdot Y(\theta = \varphi) \cdot \cos^{-1}(\varphi) \approx E(z \tan(\varphi)) \quad \text{Eq. 4.2}$$

The discharge current was increased to 0.9 A to allow a higher experimental throughput, and the MFM was centered ($x = 0$ mm). The experiments were performed with Cu at different distances ($z = 25$ mm, 50 mm, 100 mm) and different pressures ($p = 0.3$ Pa, 0.5 Pa, 0.7 Pa, 1 Pa). In addition to the experiments, test results were simulated with SIMTRA. Again a good match was found (*Figures 6.6 a-c*). The match of the ratio R_{min}/R_{max} is remarkably good. A slight mismatch is observed at higher angles. SIMTRA predicts here a higher amount of scattered particles. It is obvious that the pressure has only a slight influence at the distance of 25 mm.

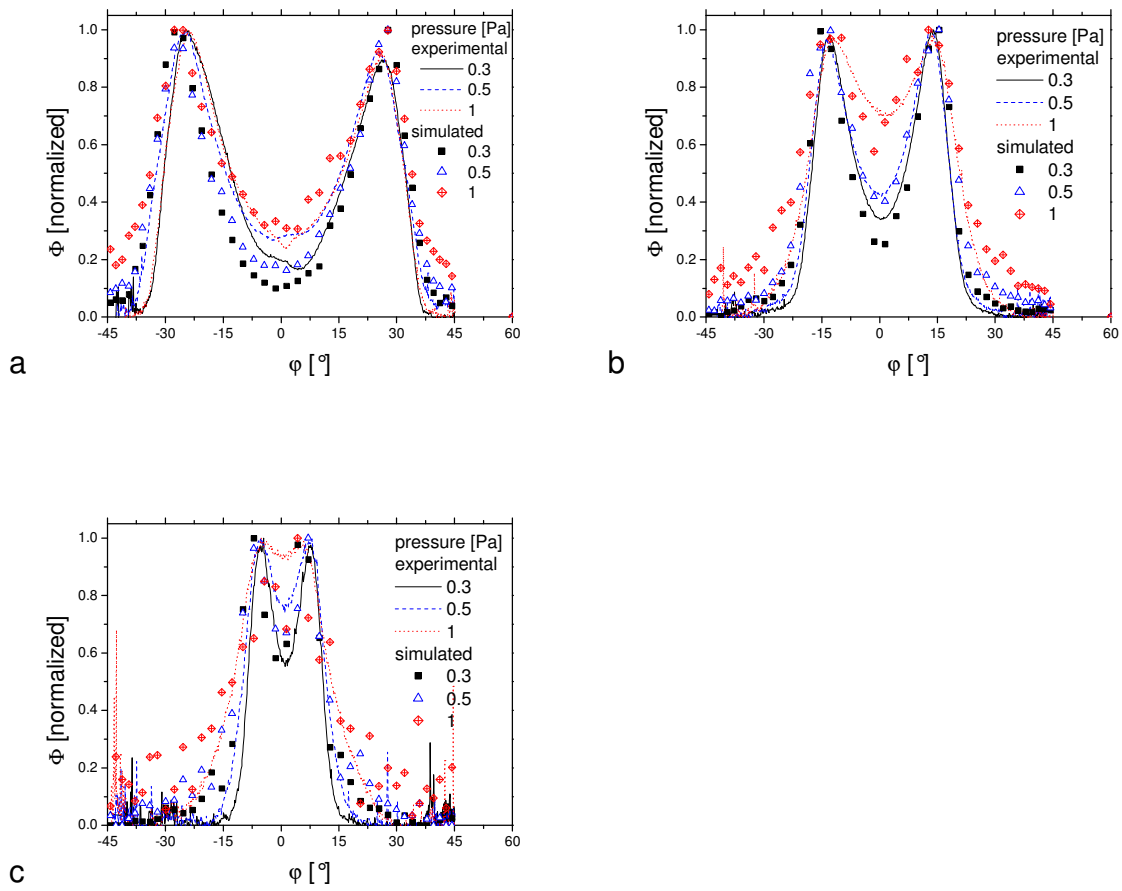


Figure 6.6: Angular distribution $\Phi(\varphi)$ of the metal flux from a 2 inch Cu target as function of the working gas pressure for different distances a) 25 mm, b) 50 mm, c) 100 mm.

As introduced in the previous section (6.1.1), the ratio R_{min}/R_{max} was compared (figure 6.7) to the calculated value P_{therm} (according to Eq. 2.20). Again a good match was found, especially for greater distances. At smaller distances the matches are not as good, which can be explained by the few collisions a metal particle undergoes (25 mm is in the range of the mean free path) and the relatively simple analytical model used for P_{therm} .

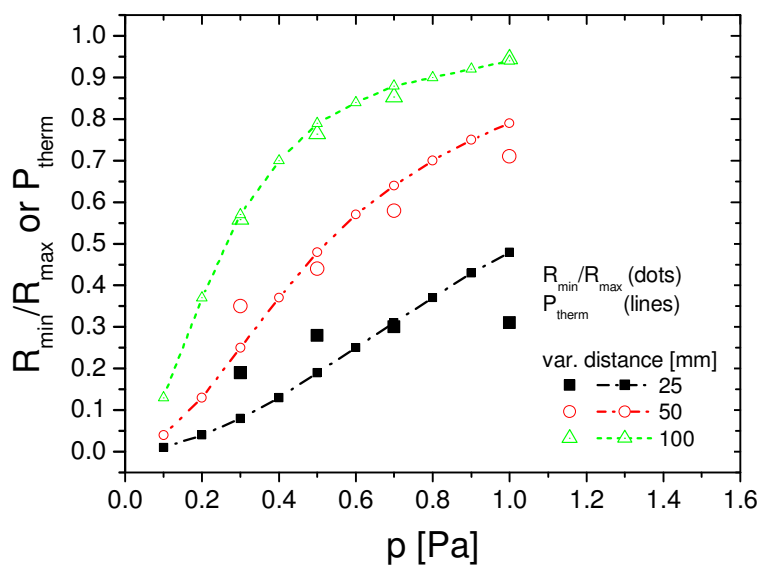


Figure 6.7: Comparison between R_{\min}/R_{\max} (observed) and P_{therm} (calculated) for Cu (2" magnetron) with variable distances and pressures.

6.1.3 Cylindrical Magnetron

As mentioned in section 4.2, the angular distribution of the metal flux from a planar magnetron is determined by the ejection probability on the target surface (which is equal to the profile of the erosion zone), the scattering in the gas phase, and the nascent angular distribution (which has just a minor impact). In contrast, a cylindrical magnetron has the advantage, that the ejection probability is equal at every position of the target. The angular distribution of fluxes is therefore only influenced by the nascent angular distribution and by gas phase scattering. If one assumes a cosine shaped nascent angular distribution, one would obtain in a first approximation (e.g. neglecting scattering), a rectangular shaped angular distribution. The measurement of the angular distribution of the flux from a cylindrical magnetron gives therefore information on the nascent angular distribution. It should be noted, that the angular distributions of the flux from a planar and from a cylindrical magnetron have similar shapes, but are mainly influenced by different parameters, i. e. the ejection probability for a planar magnetron, (*figure 4.3*), and the nascent angular distribution for a cylindrical magnetron, (*figure 4.4*).

The experiments were performed in LAB III with the MFMZ. The position of the pinhole was centered horizontally, but vertically it was positioned in the upper third of the cylindrical target. As only the horizontal angular distribution was of interest, this had just a minor influence. Experiments with a Cu target at distances of 25, 50 and 100 mm were conducted (0.15 Pa *figure 6.8a*; 0.29 Pa *figure 6.8b*). The results for the experiments with a distance of 25 mm were discarded, since the Cu oxidized due to the high thermal exposure. The reproducibility of the experiments showed an interesting behavior. Three experiments were conducted with the same parameters. Looking at the normalized distribution, they were merely identical. But when the total layer thicknesses were compared, a difference of a factor up to 2 could be observed, although the parameters were identical. The reason for this effect is unknown. A possible explanation would be that the size of the pinhole changes over time. On the other hand this would lead to a steady decrease of the deposition rate, which could not be observed.

With the Al target, experiments were conducted at 0.15 Pa and at distances of 25 and 50 mm (*Figure 6.8c*). The difference between experiments and simulation can be

explained by the insufficient roughness of the target surface, as the experiments were conducted with a new target that was not yet strongly utilized. As explained in [31], surface roughness has a distinct impact on the nascent angular distribution, and SIMTRA uses the nascent angular distributions of rough surfaces. The experiments with Ti as target material were conducted at 0.15 Pa at distances of 25, 50 and 100 mm (*Figure 6.8d*). Ti is of great interest, as it is the material with a nascent angular distribution which diverges strongly from the cosine shape. The pd product of these experiments ranges from 0.27 Pa cm to 2.9 Pa cm and is therefore in the low and intermediate pressure regime. The low pd product is of importance, as the nascent angular distribution is of greater interest than the gas phase transport, which was investigated in the experiments before.

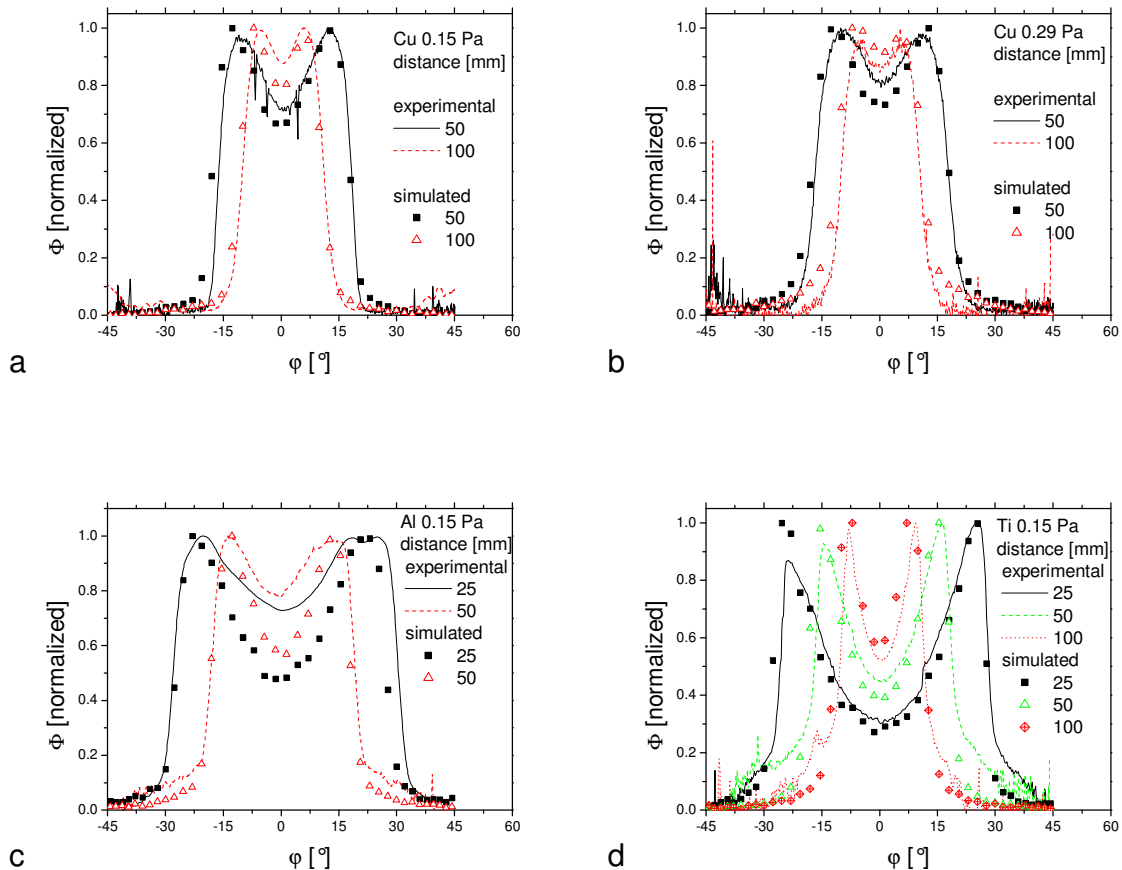


Figure 6.8: Angular distribution $\Phi(\varphi)$ of the metal flux from a cylindrical magnetron as function of the distance for different materials a) Cu (at 0.15 Pa; 450 V); b) Cu (at 0.29 Pa, 390 V); c) Al (at 0.15 Pa; 412 V) and d) Ti (at 0.15 Pa 364V). The shape of the angular distribution reflects the heart like shape of the nascent angular distribution, since the values at the edges are higher than the value in the center.

As shown in section 4.2.3, the angular distribution can also be compared to a numerical model given by Eq. 4.9

$$\Phi_{cps} = \Phi_{c,pin} \otimes u_s = \Phi_c \otimes (u_{pin} \otimes u_s) = \Phi_c \otimes u_{s+p} \quad \text{Eq 4.9}$$

where the analytical angular distribution from a cylindrical magnetron Φ_c is convolved with the point spread function of the pinhole (u_{pin}) and the point spread function from gas scattering (u_s).

The standard deviation of the Gaussian distribution, which reflects gas phase scattering, was found to be 3° for all investigated distances and materials. This is surprising, as distance changes by a factor of 4 and the materials should have different scattering characteristics, but may be explained by the low number of collisions that take place at this pd product.

In *figure 6.9 a,b* and *figure 6.10 a,b* the comparison between experiments and calculations are shown for Ti and Cu, the two materials where a good match between simulation and experimental result could be observed. Also a comparison between the two different models, c_i fit and β fit are shown, and it is obvious, that the differences between these two models are diminishing as the results are more and more convolved and thus smoothed.

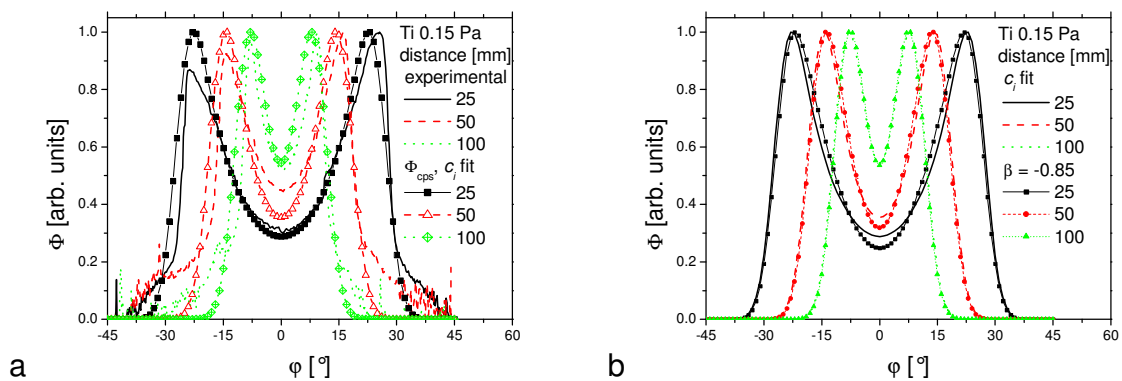


Figure 6.9 a) Comparison of the experimental and numerically calculated angular distribution (Ti at $p = 0.15$ Pa). The match between the simulation and the calculation using the c_i fit is very good. b) Comparison of the calculated results using the c_i fit and the β fit. The difference between both calculation methods is minor.

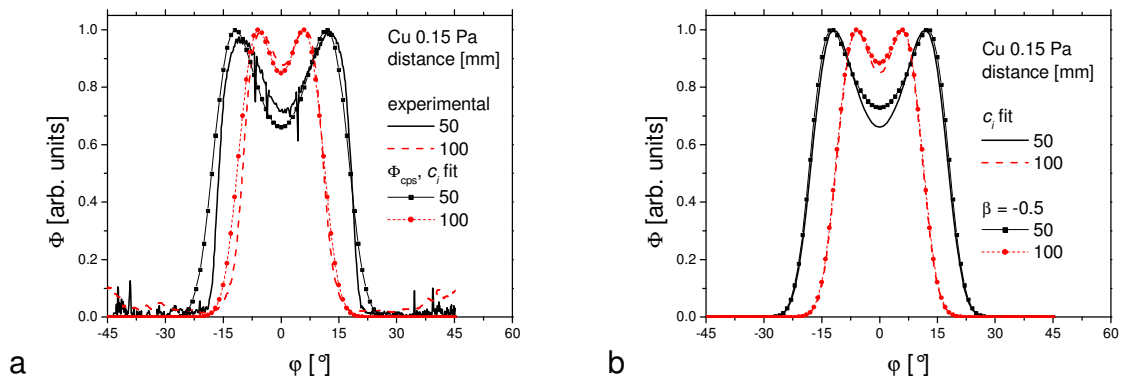


Figure 6.10 a) Comparison of the experimental and analytically calculated angular distribution (Cu at $p = 0.15$ Pa). The match between the simulation and the calculation using the c_i fit is very good. b) Comparison of the calculated results using the c_i fit and the β fit. The two fits deviate more in the case of Cu, the difference is larger when compared to Ti, but still minor.

As $\Phi(\varphi)$ from a cylindrical target can easily be calculated by the model described in section 4.2.3 quite accurately, it can be used to derive an unknown β from an experimentally determined $\Phi(\varphi)$, by fitting Φ_{csp} to it. This will be demonstrated with the experiments conducted with an Al target, where the simulated results do not match the experimentally obtained. First, it is shown in *figure 6.11a*, that Φ_{csp} using the c_i fit has a very good match with the results obtained by SIMTRA, which is using a nascent angular distribution according to the c_i fit (The corresponding β value to the c_i fit for Al would be -0.65). This proves that the model and the chosen parameters are also valid in this case. By adjusting β until Φ_{csp} matches the experimental result (*figure 11.b*), the true β value of this experiment can be determined, which is $\beta = -0.43$. Therefore, the nascent angular distribution, described by the β -fit, can be derived from the angular distribution of the metal flux from a cylindrical target by an elegant method.

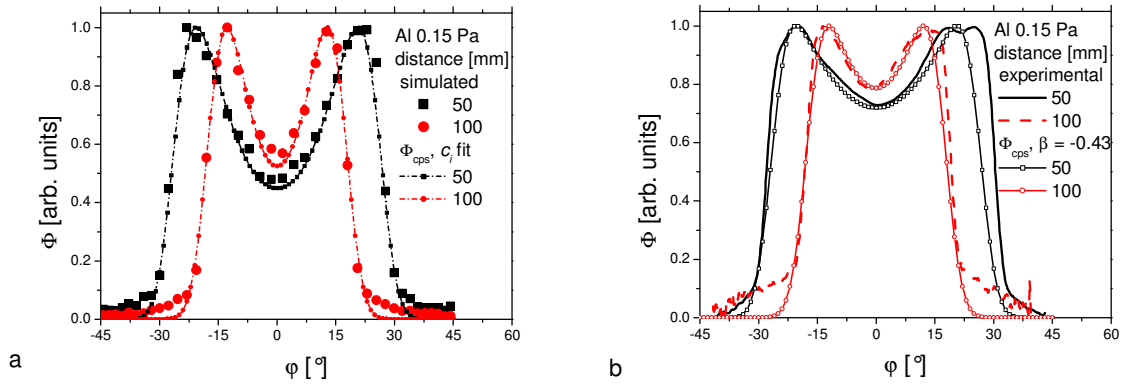


Figure 6.11 Comparison of the angular distribution for a cylindrical Al target. a) The simulated distribution and the calculated distribution using the same $Y(\theta)$ as the simulation are in a good match, thus proving the validity of the used analytical model. b) Experimental results match the calculated results when using the β -fit with β being -0.43 .

According to Eq. 2.3,

$$\beta = B \ln \left(\frac{m_t E_0}{m_g U_s} \right) - B_c \quad \text{Eq. 2.3}$$

the β value can be calculated for smooth surfaces. A comparison of the β value calculated by Eq. 2.3, the β value derived from the c_i fit, and the β value determined by the experiments is shown in table 6.2. As E_0 , 75% of the discharge voltage is used. The β value obtained from the Al experiments matches the calculated β from a smooth surface, thus substantiating the assumption that the deviation between experiments and simulation was caused by the use of a virgin and thus weakly roughened target. A comparison of the Ti and the Al cylindrical targets are presented in figure 6.12.

β from	Ti ($E_0 = 273$ eV)	Cu ($E_0 = 338$ eV)	Al ($E_0 = 309$ eV)
c_i fit	-0.85	-0.5	-0.65
experiments	-0.85	-0.5	-0.43
Eq. 2.3	-0.388	0.008	-0.425

Table 6.2: Comparison of the different β values.

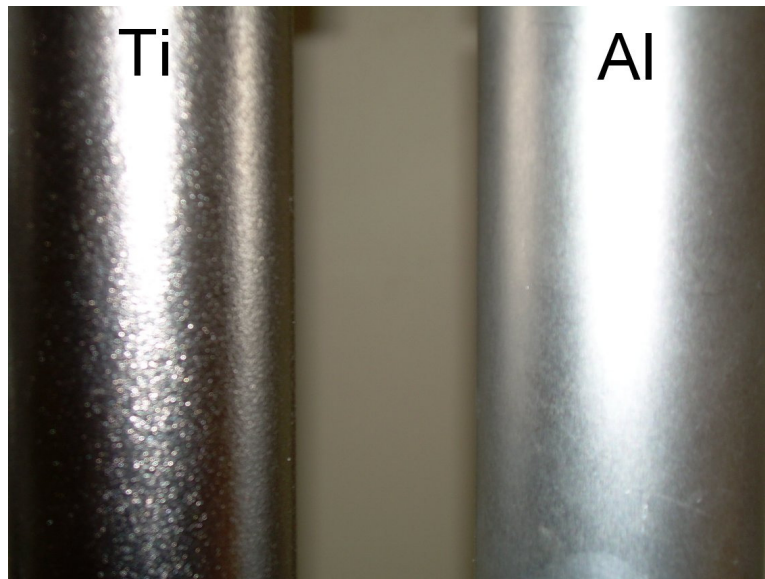


Figure 6.12 Comparison of the surface of the Ti and the Al cylindrical targets. The Ti target surface is obviously rough, while the Al target surface is still very smooth.

This shows that the determination of the angular distribution of the arriving flux can be used to directly determine an important parameter of the sputter deposition process like the nascent angular distribution. The method described above can be used to measure the nascent angular distribution of a real sputter deposition in just one measurement without the use of complex and time-consuming programs and fitting algorithms. The only prerequisite is a homogeneously sputtered target.

6.1.4 Rotatable Magnetron

Another test series was carried out with the rotatable magnetron (diameter 50 mm) by the staff of the Ghent University. The rotatable magnetron is similar to the cylindrical one, with the difference that the magnetic system is static and the target itself is rotating (*figure 6.13 a*). Its angular distribution is therefore primarily determined by the local emission intensity (*figure 6.13 b*).

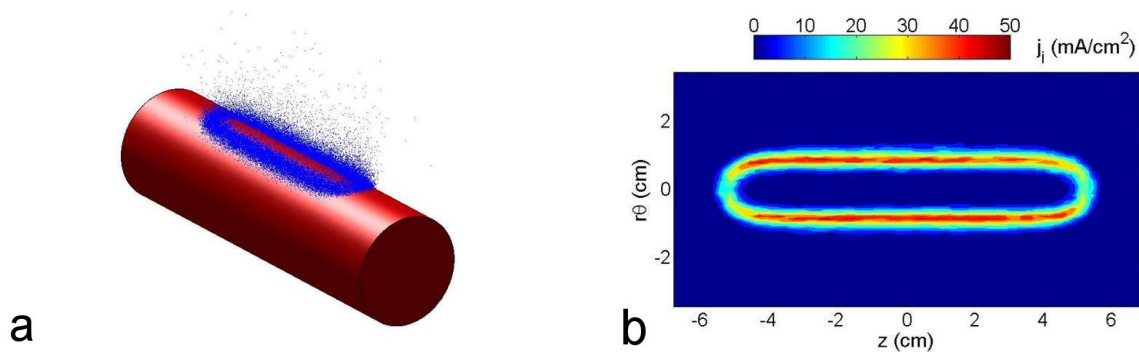


Figure 6.13 a) sketch of a rotatable magnetron. The magnetic system is static with the target being rotated. b) Distribution of the local ion current which is proportional to the local emission intensity $E(R)$. Most of the particles originate from the two parallel lines.

The discharge current I was usually set to 0.5 A (except one series with variable I). Series were carried out for different materials, pressures, z -distances, discharge currents, and orientation of the magnets (parameters given in *table 6.3*).

Material	p [Pa] ($z = 100$ mm)	z -distance [mm] ($p = 0,3$ Pa)
Cu	0.1; 0.3; 0.5; 0.7; 1; 1.2	15; 30; 50; 70; 90; 100; 150
Al	0.15; 0.3; 0.5; 0.7; 1; 1.2	15; 30; 50; 100; 150
Ti	0.15; 0.3; 0.5; 0.7; 1	30; 50; 100; 150
	z -distance[mm] ($p = 0,5$ Pa)	
Cu	15; 40; 65; 90; 100; 140	
	orientation of magnets [$^\circ$] ($p = 0.3$ Pa; $z = 100$ mm)	
Cu	0; 10; 20; 30; 40; 50; 70; 90	
	discharge current I [A]	
Cu	0.3; 0.5; 0.7; 0.9	

Table 6.3 Parameters of the experiments with the rotatable magnetron

The result of the experiments is very similar to those described in section 6.1.1 and 6.1.2 (planar magnetrons), e. g. more broadening of the angular distribution of the arriving flux with increased pd product or lighter material. The series with variable discharge current showed that the discharge current has no influence on the angular distribution $\Phi(\varphi)$. Therefore just selected experiments will be presented here. All experiments were compared to simulations by SIMTRA. Although the match is reasonably good, it is not as good the match for the planar or cylindrical magnetron.

One possible explanation is that it is harder to measure the ejection probability $E(R)$ from a rotatable magnetron.

Figure 6.14 presents the influence of the distance z on the angular distribution $\Phi(\varphi)$ of Cu for a rotatable magnetron ($p = 0.3 \text{ Pa}$; $I = 0.5 \text{ A}$; $U = 380\text{-}390 \text{ V}$). Experiments were conducted in LAB III. The results were normalized by the area beneath the curves. The angular distribution looks similar to those from a 2" planar magnetron.

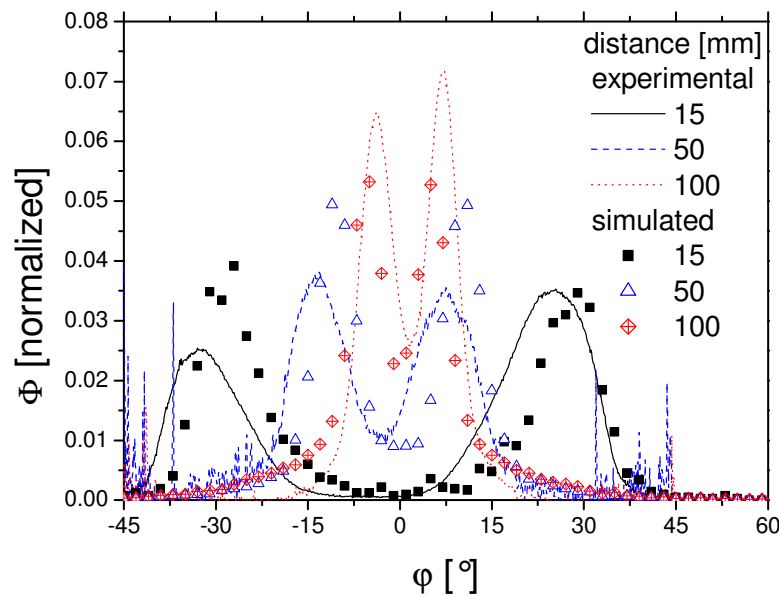


Figure 6.14: Angular distribution $\Phi(\varphi)$ of the metal flux as a function of the z distance for Cu sputtered at a pressure of 0.5 Pa.

An interesting feature of the rotatable magnetron geometry is that a part of the racetrack can be covered when the magnetic system inside the magnetron is tilted. This has the advantage that the angular spread of the arriving metal flux can be minimized when the correct tilting angle is used, thus one line of the racetrack is masked by the target itself since it is curved. A further increase of the tilting angle will decrease the angular spread, but at the cost of a significantly decreased deposition rate. The influence of the tilting angle of the magnets on the angular distribution $\Phi(\varphi)$ is shown in figure 6.15 for Cu as target material. At a tilting angle of 0° (the magnetic system, and therefore the racetrack, is pointing towards the pinhole) the angular distribution $\Phi(\varphi)$ is similar to a planar magnetron with two peaks of equal height. At 30° the peak of the line facing towards the pinhole is dominant, but the second one is still visible. At 40° , the minor peak is covered by the dominant one and just one peak

with a shoulder is visible. At 50° there is no trace of the minor peak anymore. The arriving particles are primarily originating from just one line. This is not achievable with a planar target, as a curved target is needed to mask the second line of the racetrack.

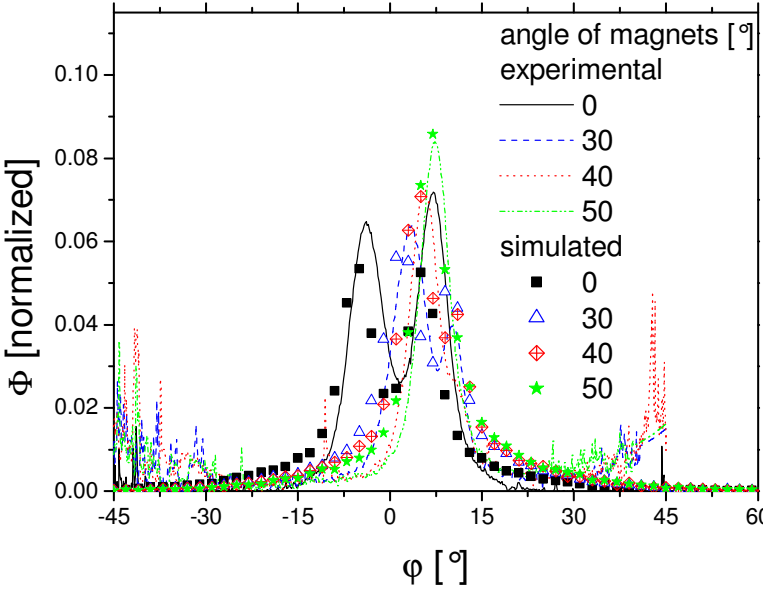


Figure 6.15: Angular distribution $\Phi(\phi)$ of the metal flux as function of the tilting angle of the magnets for Cu as target material $p = 0.5$ Pa; $z = 100$ mm; $I = 0.5$ A.

6.2 Influence of a reactive atmosphere on the angular distribution of the metal flux

Following the systematic test series conducted in a pure argon atmosphere, selected tests were carried out with a controlled addition of oxygen as reactant to the argon, in order to observe the effects of a reactive atmosphere on the angular distribution of the metal flux. Reactive sputtering creates the following major difficulties for the MFM:

- considerably reduced deposition rates,
- considerable fluctuation of the deposition rate,
- need for reconditioning of the targets after each experiment,
- need for removal of the insulating layer on the front plate of the MFM, either by polishing it away or by alternating reactive with non reactive experiments to create a new conducting layer on it,
- possible prevention of experiments with short target MFM distance owing to the insulating nature of the oxide film (like Al_2O_3) deposited on the front plate of the MFM,
- occasionally, insulating layers inside the MFM had to be removed.

The experiments were carried out with the three types of magnetrons from Vienna University of Technology described above. In addition a 2" planar magnetron and the rotatable of Ghent University were used.

When varying the oxygen flow, one can either use a constant total pressure (constant p_{tot} mode) or constant Argon pressure (constant p_{Ar} mode). The constant p_{tot} mode has the advantage that effects like gas phase scattering are determined by the total pressure. On the other hand it is cumbersome, as the Ar flow and the O_2 flow have to be changed simultaneously. Additionally, the hysteresis curve is usually measured in constant p_{Ar} mode, thus results obtained in constant p_{tot} mode can not be easily compared to the hysteresis curve.

The first series of experiments were conducted in the constant p_{tot} mode, to investigate the influences on $\Phi(\varphi)$ when the Argon in the working gas is systematically replaced by oxygen. The experiments of this series were conducted in LAB II.

Figure 6.16 presents the results of measurements with oxygen addition to the discharge when using the 2" planar magnetron of Ghent University for Ti and Al at constant total pressure but with varying oxygen partial pressures (constant p_{tot} mode). Distance MFM to target was 100 mm and discharge current was kept constant at 0.9 A. More intensive peaks develop in the angular distribution of the metal flux, as the sputtering process changes from metallic sputtering to reactive sputtering. With further increase of the oxygen partial pressure, however, this effect tends to diminish again. A small eccentricity also occurs at these measurements. At constant currents, changes of the discharge voltage clearly indicated that the adding of oxygen poisons the target. Figure 6.17 shows the hysteresis behavior of these two materials. Since the reproducibility of experiments conducted under reactive atmosphere can be problematic, each experiment was repeated three times. The repeated experiments were always in good agreement if proper care was taken of creating equal initial conditions for the MFM- experiments (see previous points).

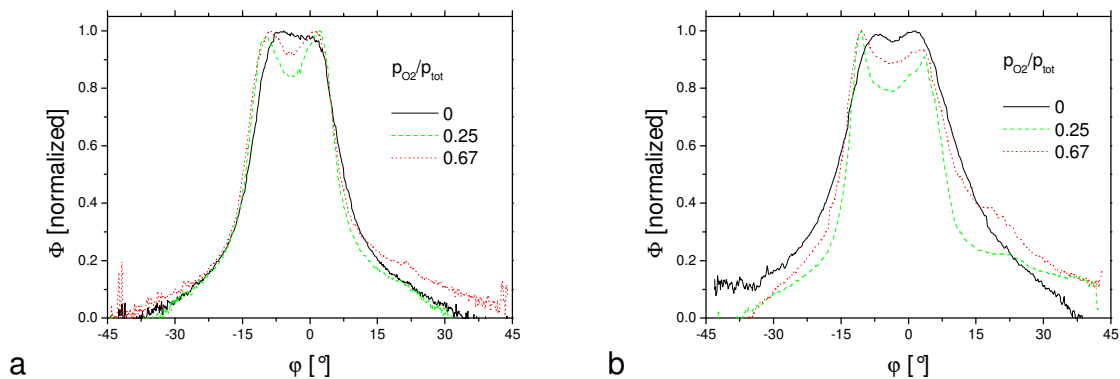


Figure 6.16 Angular distribution of Ti (left) and Al (right) at different oxygen partial pressures, but constant total pressure. Total pressure: Ti 0.65 Pa; Al 0.67 Pa. The discharge voltages for Ti were 355V ($p_{O_2}/p_{tot} = 0$); 432V ($p_{O_2}/p_{tot} = 0.25$); 406V ($p_{O_2}/p_{tot} = 0.68$). The discharge voltages for Al were 418V ($p_{O_2}/p_{tot} = 0$); 270V ($p_{O_2}/p_{tot} = 0.25$); 275V ($p_{O_2}/p_{tot} = 0.68$).

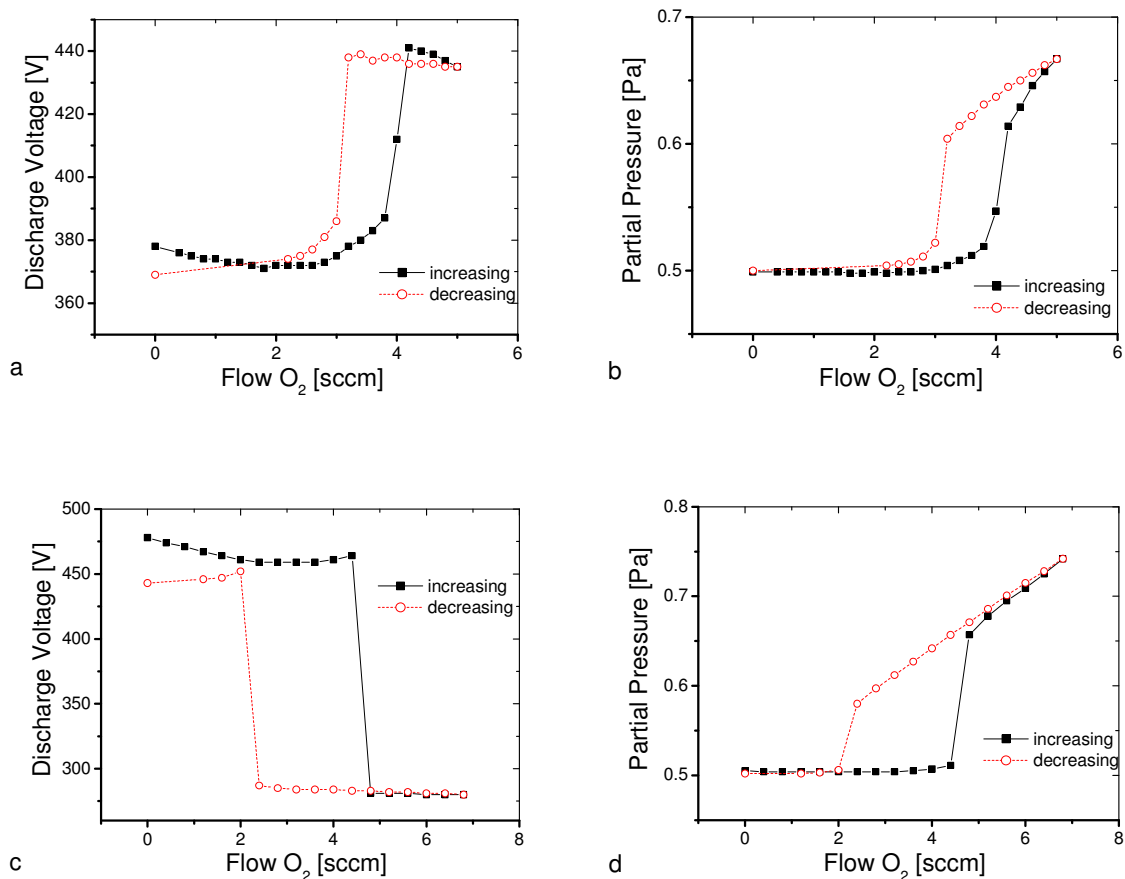


Figure 6.17 Hysteresis of discharge voltage a) Ti; c) Al; and partial pressure of oxygen b) Ti; d) Al.

As described in section 6.1.1, the parameter R_{min}/R_{max} is a useful parameter to characterize the shape of the angular distribution of the arriving flux, as it is correlated to the amount of gas scattering in the case of a planar magnetron (0 \rightarrow no scattering; 1 \rightarrow isotropic flux). R_{min}/R_{max} is plotted in figure 6.18 with p_{O_2}/p_{tot} being the x-axis. Although two different materials were investigated (Al and Ti) their behavior is similar, i.e. a distinct drop of R_{min}/R_{max} after switching from metallic mode to reactive mode, followed by an increase of R_{min}/R_{max} when Ar is further replaced by O_2 . For the experiments conducted with Ti the standard deviation of R_{min}/R_{max} of the three experiments conducted with the same parameters could be determined. The standard deviation was 0.008 ($p_{O_2}/p_{tot} = 0$); 0.027 ($p_{O_2}/p_{tot} = 0.25$); and 0.018 ($p_{O_2}/p_{tot} = 0.68$).

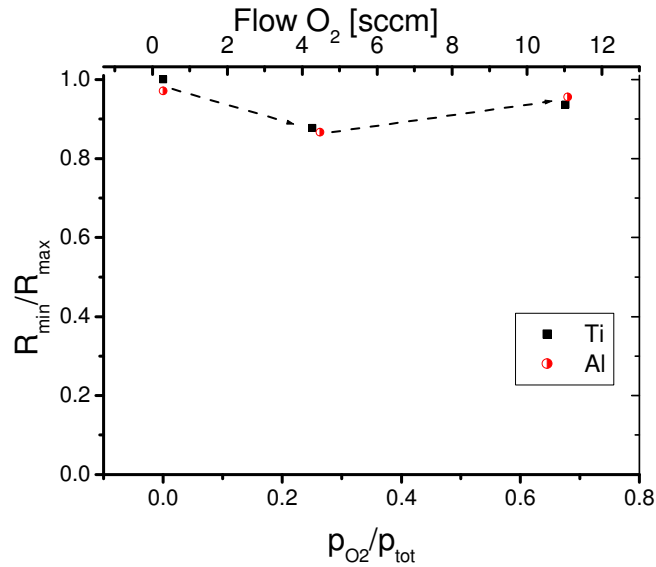


Figure 6.18 R_{min}/R_{max} for the experiments with Ti and Al in a reactive atmosphere. The value drops when switching from metallic to poisoned mode and rises when p_{O_2}/p_{tot} is further increased. This behavior (indicated by dashed arrow) for Ti and Al is similar.

Measurements with the 100 mm diameter magnetron and Al as target material in constant p_{tot} mode (discharge current kept constant at 0.9 A; total pressure: 0.5 Pa; distance MFM target: 95 mm), however, showed no distinct changes (beside a small decrease of R_{min}/R_{max} from 0.81 to 0.77 when switching from metallic to reactive mode, value remains constant with further replacement of Ar by O₂) in the angular distribution of the flux (figure 6.19 a,b), which is contradictory to the measurements with the 2" magnetron of Ghent University. The deposition rate and discharge voltage clearly indicate, that the target was poisoned by the sputtering in a reactive atmosphere (behavior similar to that shown in figure 6.17 c,d).

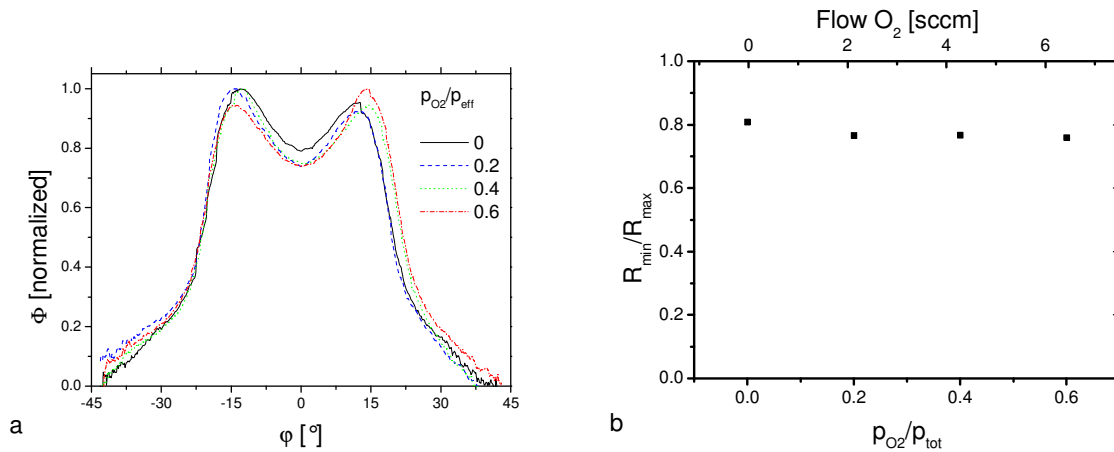


Figure 6.19: a) Angular distribution of Al (target diameter 100 mm) at different oxygen partial pressures, but constant total pressure. The discharge voltages were 560V ($p_{O_2}/p_{tot} = 0$); 330V ($p_{O_2}/p_{tot} = 0.2$); 312V ($p_{O_2}/p_{tot} = 0.4$); 286V ($p_{O_2}/p_{tot} = 0.6$). b) Slight difference in R_{min}/R_{max} between non-reactive and reactive mode.

To solve the question, if the effects observed in figure 6.16 originate from target poisoning, which reduces the sputtered area, or from gas phase scattering, a measurement series was carried out with the 2" planar magnetron of Vienna University of Technology and with variable target distances ($z = 25$ mm, 50 mm, and 100 mm). Al was selected as target material. However, this choice proved to be problematic, since the deposited Al_2O_3 layer on the cover plate disturbed the plasma discharge at shorter distances (25 mm and 50 mm). Still, the experiments with a distance of 100 mm (figure 6.20; discharge current kept constant at 0.9 A; total pressure 0.5 Pa) worked well, and coincided with the pattern of the experiments with the magnetron of the Ghent University (figure 6.16). One interesting observable effect is that in addition to the change in R_{min}/R_{max} , the shape of the maximum at the racetracks is becoming sharper when sputtering in a reactive atmosphere. Due to the problems experienced with the use of Al (which forms an insulating Al_2O_3), it was decided to continue the experiments on reactive sputtering with Ti as target material, since Ti-oxide is semi conductive.

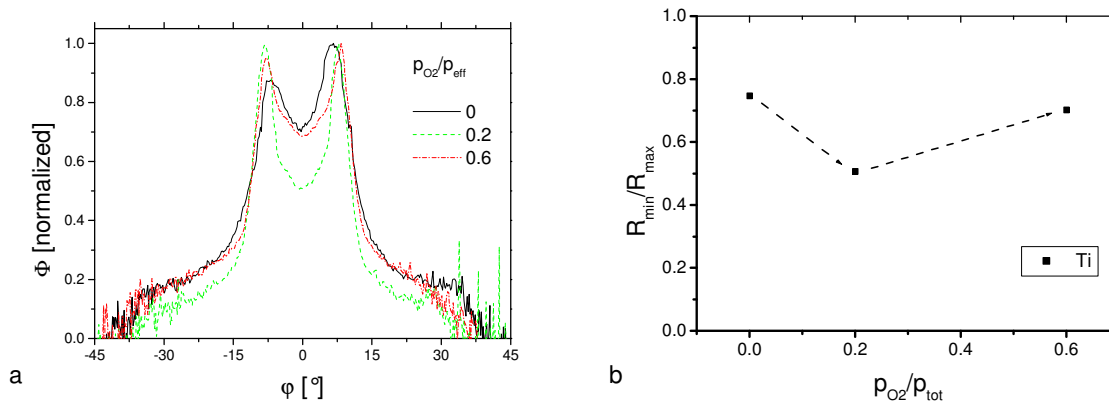


Figure 6.20: Angular distribution of Al (target diameter 2") at different oxygen partial pressures, but constant total pressure. Discharge voltages: 510V ($p_{O_2}/p_{tot} = 0$); 298V ($p_{O_2}/p_{tot} = 0.2$); 270V ($p_{O_2}/p_{tot} = 0.6$). b) R_{min}/R_{max} behavior similar to figure 6.16. For $p_{O_2}/p_{tot} = 0$ and $p_{O_2}/p_{tot} = 0.6$ (Flow: 4 sccm Ar; 7.8 sccm O₂) the pumping speed was throttled, while for $p_{O_2}/p_{tot} = 0.2$ (Flow: 34.3 sccm Ar; 8 sccm O₂) it was un-throttled. Therefore R_{min}/R_{max} can not be shown as a function of the O₂ flow.

In the next test series, the experiments were conducted in the constant p_{Ar} mode, since the results can be better linked and compared to the hysteresis curve and its critical point. Additionally, Ti was chosen as target material, since its oxide is to some extent semi conductive. The aim of this series was to distinguish, if the effects observed above originate from the target or the gas phase transport.

In this test series the planar 2" magnetron of Vienna University of Technology was used for a Ti Target (Test parameter: p_{Ar} constant 0.3 Pa, discharge current: 0.7 A), the switch from metallic mode to reactive mode occurred at a flow of 5 sccm O₂ (see figure 6.21 for hysteresis), but the hysteresis behavior was not as pronounced as in the other test series. In addition, one measurement was performed with p_{Ar} 0.5 Pa, which is equal to the total pressure of the experiment with 8.7 sccm O₂ (0.3 Pa Ar + 0.2 Pa O₂). The experiments were carried out at distances $z = 50$ mm (figure 6.22a) and $z = 100$ mm (figure 6.22b). It should be noted, that the experiments at 50 mm were problematic due to charging effects and that their reproducibility can not be granted.

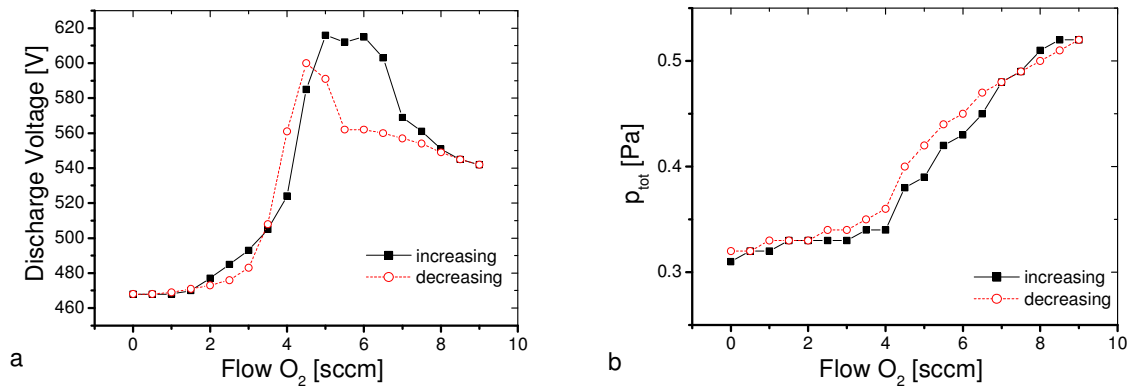


Figure 6.21 Hysteresis of a) discharge voltage and b) total pressure for a 2'' planar Ti target at 0.7 A.

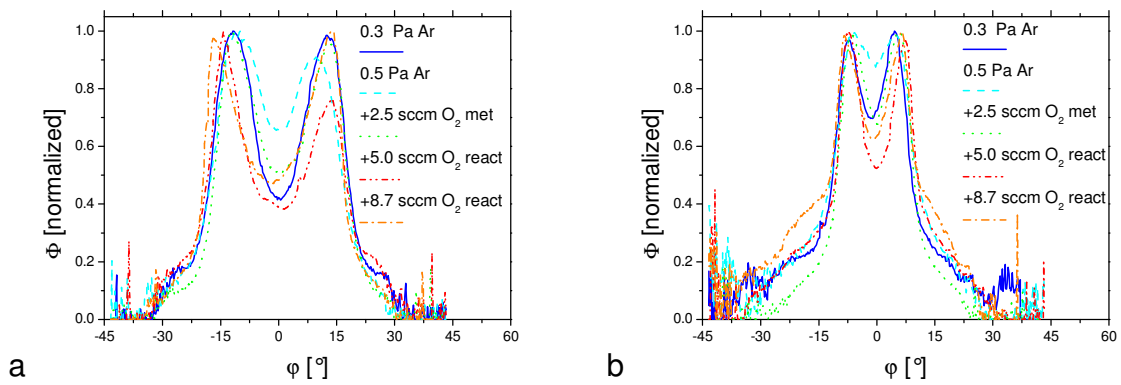


Figure 6.22: Angular distribution obtained from a 2'' planar magnetron with Ti target at different oxygen flows, but with constant Ar pressure. Distance MFM target: a) 50 mm; b) 100 mm. Discharge voltages for $z = 50$ mm: 402V (only 0.3 Pa Ar); 386V (only 0.5 Pa Ar); 409 (+2.5 sccm O_2 metallic); 520V (+5.0 sccm O_2 reactive); 482V (+8.7 sccm O_2 reactive). Discharge voltages for $z = 100$ mm: 446V (only 0.3 Pa Ar); 437V (only 0.5 Pa Ar); 458 (+2.5 sccm O_2 metallic); 525V (+5.0 sccm O_2 reactive); 485V (+8.7 sccm O_2 reactive).

It is interesting to note that the ratio R_{min}/R_{max} does not change significantly with increasing oxygen partial pressures, when the distance amounts to $z = 50$ mm (figure 6.23a). For the experiments with $z = 100$ mm (figure 6.23b), this ratio decreases with increasing oxygen partial pressure.

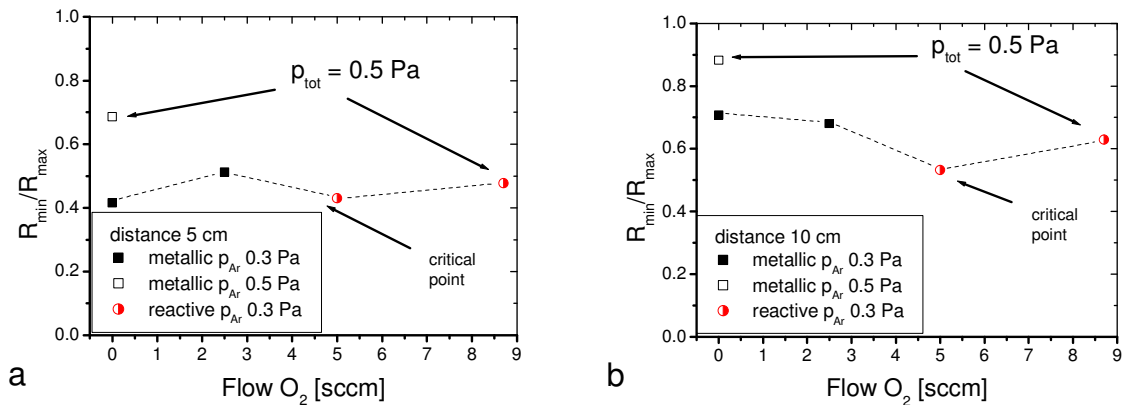


Figure 6.23: The ratio R_{min}/R_{max} displayed over the oxygen flow for a) $z = 50$ mm and b) $z = 100$ mm. Results with $p_{Ar} = 0.3$ Pa are connected by dashed lines. Critical point and the two experiments with $p_{tot} = 0.5$ Pa are indicated by arrows.

While R_{min}/R_{max} of the experiments conducted under reactive atmosphere are of the same magnitude as those conducted in metallic mode at close distance, the ratio of the reactive experiments is distinctly smaller than those conducted in metallic mode for $z = 100$ mm. This effect is even more visible when the ratio R_{min}/R_{max} is plotted over the total pressure (figure 6.24). R_{min}/R_{max} should increase as p_{tot} (and thus the pd product) increases, but instead it stays constant at $z = 50$ mm and even decreases at $z = 100$ mm, when switching from metallic to reactive mode. When doubling the distance, the ratio for metallic mode increases significantly, while the ratio of the reactive mode increases just a little. In the end the ratio of the reactive mode is below those in the metallic mode at $z = 100$ mm, although the total pressure is significantly higher. This effect has three possible origins. A change in $E(R)$, gas phase transport or nascent angular distribution. When the effect is caused by a change in $E(R)$, the observed change would be most pronounced at close distances, which isn't the case, therefore it can be concluded that there are no or only minor changes in $E(R)$. The nascent angular distribution has only a minor effect on the angular distribution of the arriving metal flux when sputtering from a planar target. Therefore a change in the nascent angular distribution can not be solely responsible for the observed changes. Therefore, these effects can only be caused by changes in the gas phase transport mechanism, as the angular distribution of the metal flux is less smeared out when the experiment is conducted under reactive atmosphere, although the total pressure is increasing (p_{Ar} is always 0.3 Pa), and this effect is more pronounced when the distance is getting larger.

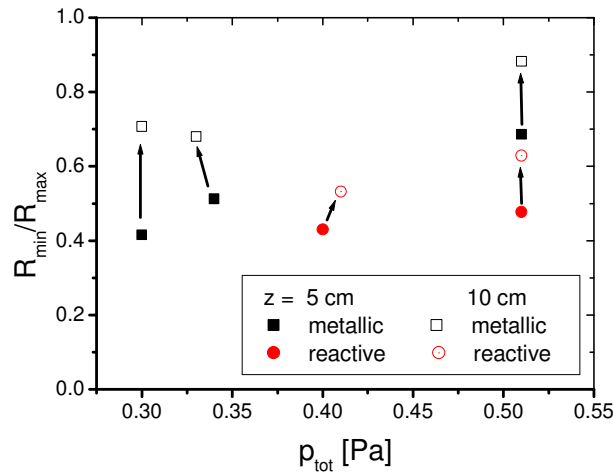


Figure 6.24: The ratio R_{min}/R_{max} in dependence on p_{tot} . The shift of each point when distance is doubled is indicated by an arrow.

To determine the influence of oxygen addition on the nascent angular distribution, experiments were performed on Ti targets with the cylindrical magnetron in LAB III. As mentioned in section 6.1.3, the angular distribution of the arriving flux $\Phi(\varphi)$ is dominated by the nascent angular distribution $Y(\theta)$, when the deposition pressure is low, hence gas phase scattering has only a minor impact on the angular distribution of the arriving flux, and $E(R)$ is constant for a cylindrical target anyway. The experiments (of which selected results are presented in figure 6.25; discharge current kept constant at 0.9 A; p_{Ar} was 0.3 Pa; distance MFM target was 50 mm) exhibit a clear correlation between the nascent angular distribution and the addition of oxygen during reactive sputtering (figure 6.26). A low pd product was used to limit the influence of the gas phase transport. With no oxygen addition R_{min}/R_{max} is about 0.5, with additional oxygen but in metallic mode it decreases but stays constant with the oxygen flow. At reactive mode this value increases to about 0.7. One measurement was performed with an Ar pressure of 0.36 Pa, which is equal to the total pressure of the experiment with an O_2 flow of 2.5 sccm (0.3 Pa Ar + 0.06 Pa O_2), to show that the effect is not induced by the change of total pressure. Experiments were randomly repeated to check repeatability which was found to be satisfactory.

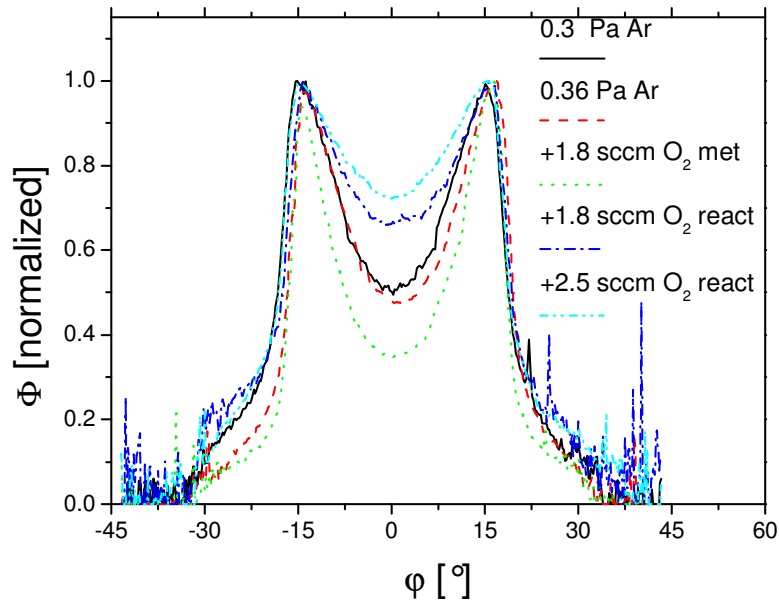


Figure 6.25: Angular distribution from a Ti cylindrical magnetron at different oxygen flows, but constant Ar pressure. The discharge voltages were 317V (only 0.3 Pa Ar); 303V (only 0.36 Pa Ar); 303V (+1.8 sccm O₂ metallic); 369V (+1.8 sccm O₂ reactive); 366V (+2.5 sccm O₂ reactive).

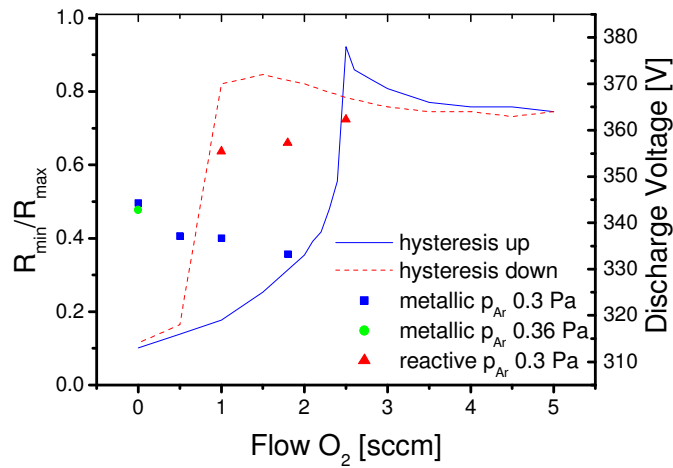


Figure 6.26 Ratio R_{min}/R_{max} and the hysteresis of the discharge voltage as a function of the oxygen flow.

By assuming equal scattering behavior for reactive and non-reactive sputtering at equal pressures and gas compositions, β can be determined by the method presented in chapter 6.1.3. As the pressure was 0.3 Pa instead of 0.15 Pa, a higher σ of 3.5° was found to be suitable for u_s as the slope of the flanks are reproduced by

this value. A comparison of selected experiments with Φ_{cps} and its corresponding β is shown in *figure 6.27*.

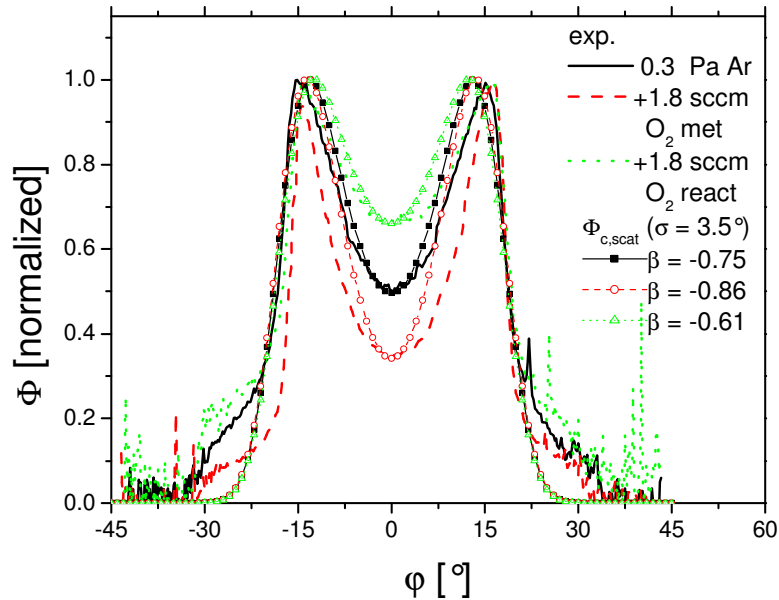


Figure 6.27 Comparison of selected experimental results to Φ_{cps} with $\sigma = 3.5^\circ$ and the β values representing best fit to the experimental data.

When varying the oxygen flow, the discharge voltage varies significantly, which has a known impact on the nascent angular distribution parameter β , given by Eq. 2.3. *Figure 6.28* gives a comparison of the calculated β according to Eq. 2.3 with E_0 being 75% of the discharge voltage, and β obtained by fitting Φ_{cps} with the experimental results. The fitted β values are smaller than the calculated ones, since the sputtered target area is considerably rougher, an effect that has been observed before. The step when switching from metallic mode to reactive mode can be partially explained by the change of the discharge voltage. When approaching the critical point from the metallic mode β decreases ($|\beta|$ increases), although it should increase. The same effect can be observed for β in reactive mode. It decreases as it approaches the transition point. As the amount of oxygen in the atmosphere is rather small in comparison to the total pressure (just 0.01 Pa p_{O_2} to 0.31 Pa p_{tot}) this effect must have its origin in the plasma surface interaction.

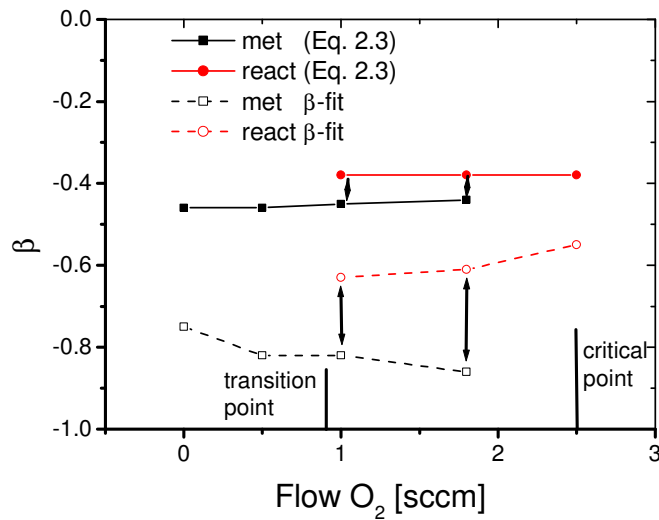


Figure 6.28 Comparison of β calculated by Eq. 2.3 (only accounting for the change in discharge voltage) and β obtained by fitting Φ_{cps} to experimental results.

The last test series using the rotatable magnetron of the Ghent University with an Al Target (Test parameter: p_{Ar} constant 0.3 Pa, discharge current: 0.9 A), the switch from metallic mode to reactive mode occurred at a flow of 3 sccm O_2 (see figure 6.29 for hysteresis). The experiments were carried out at distances $z = 50$ mm (figure 6.30a) and $z = 100$ mm (figure 6.30b), just like the series with the planar Ti target. As the experiments were conducted during a visit of staff from University Ghent, only few experiments and no repetitions were conducted, due to the tight time schedule. The results were normalized to unity.

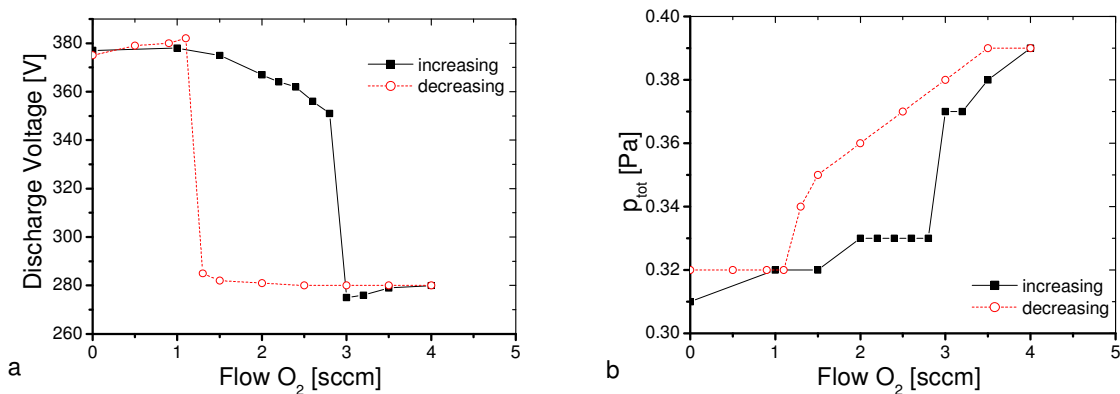


Figure 6.29 Hysteresis of a) discharge voltage and b) total pressure for the rotatable magnetron with an Al target at 0.9 A. (rotation speed 5 turns/min; pumping speed 60l/s)

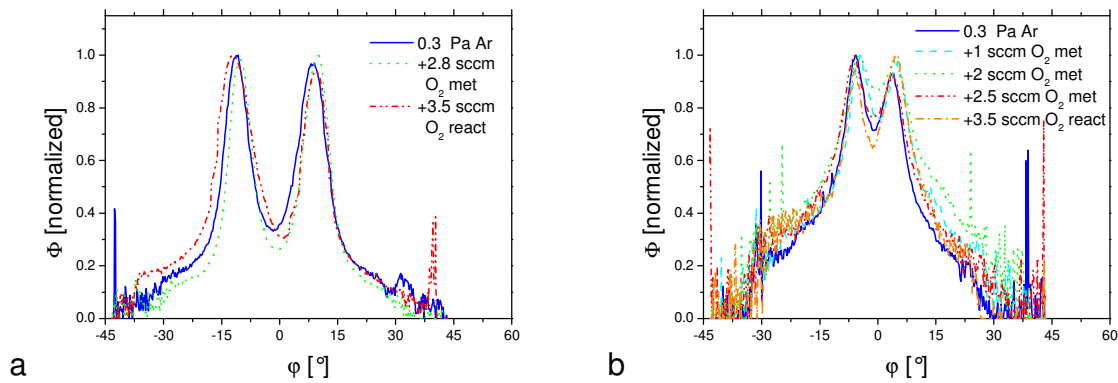


Figure 6.30: Angular distribution obtained from a rotatable magnetron with Al target at different oxygen flows, but with constant Ar pressure. Distance MFM target: a) 50 mm; b) 100 mm. Discharge voltages for $z = 50$ mm: 385V (only 0.3 Pa Ar); 388 (+2.8 sccm O_2 metallic); 268V (+3.5 sccm O_2 reactive). Discharge voltages for $z = 100$ mm: 277V (only 0.3 Pa Ar); 381 (+1 sccm O_2 metallic); 384 (+2 sccm O_2 metallic); 382V (+2.8 sccm O_2 metallic); 270V (+3.5 sccm O_2 reactive).

The ratio R_{min}/R_{max} does not change significantly with increasing oxygen partial pressures, when the distance amounts to $z = 50$ mm (figure 6.31a). For the experiments with $z = 100$ mm (figure 6.31b), this ratio decreases when switching from metallic to reactive mode at the critical point. This behavior is similar to the experiments with the planar Ti target at constant p_{Ar} mode.

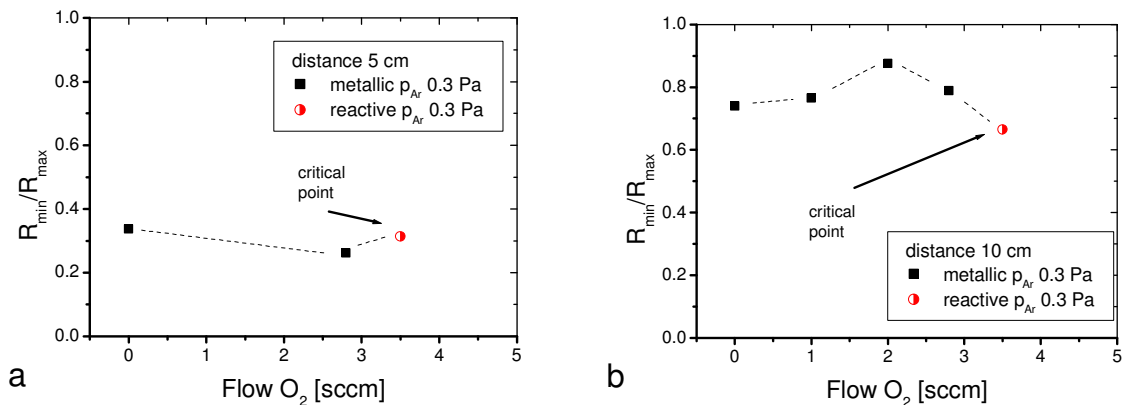


Figure 6.31: The ratio R_{min}/R_{max} displayed over the oxygen flow for a) $z = 50$ mm and b) $z = 100$ mm. Results with $p_{Ar} = 0.3$ Pa are connected by dashed lines. Critical point is indicated by an arrow.

When the ratio R_{min}/R_{max} is plotted over the total pressure (figure 6.32), its similarities to the experiments with the planar Ti target are well visible. When doubling the distance, the ratios for metallic mode increases significantly, while the ratio of the reactive mode increases just a little. In the end the ratio of the reactive mode is below

those in the metallic mode at $z = 100$ mm, although the total pressure is significantly higher. This again indicates changes in the gas phase transport mechanism.

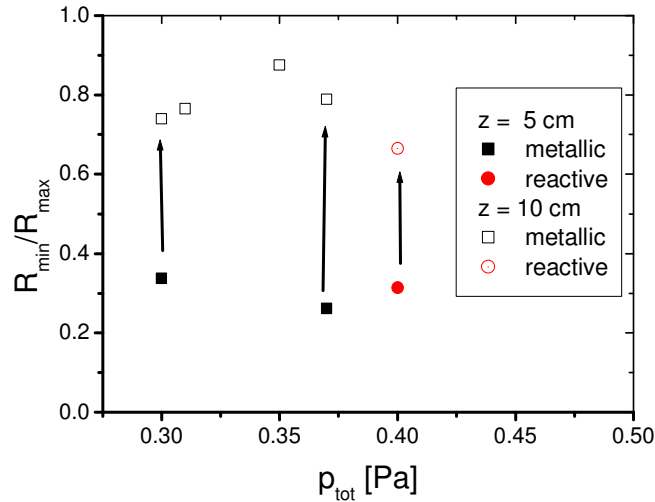


Figure 6.32: The ratio R_{min}/R_{max} displayed over p_{tot} . The shift of each point when distance is doubled is indicated by an arrow.

The influence of the addition of oxygen to the working gas on the angular distribution of the metal flux can be summarized as followed.

When looking at the experiments conducted in constant p_{tot} mode, the test series with the 100 mm magnetron showed no distinct difference between reactive and non reactive sputtering, beside the known changes in deposition rate and deposition parameters (e.g. discharge voltage). On the other hand, the test series with the 2" planar magnetrons exhibited a changed shape of the angular distribution of the metal flux, with a drop of R_{min}/R_{max} at the critical point (switching from metallic to reactive mode) with a small increase. When Ar is further replaced by O_2 . The angular distribution in reactive mode exhibits a more pronounced maximum at the race track. Additionally, the peaks at the racetrack have a sharper more peak like shape.

The experiments that were conducted with a constant p_{Ar} (the 2" magnetron with Ti and the rotatable magnetron with Al) showed similar results. At the closer distance ($z = 50$ mm) the change of R_{min}/R_{max} was smaller than at the larger distance ($z = 100$ mm). At $z = 100$ mm, the R_{min}/R_{max} of the reactive experiment was even lower than the one obtained with just $0.3 p_{Ar}$, although p_{tot} (and thus the pd product) was higher. The only explanation is that the gas phase transport has a smaller effect on the angular distribution of the arriving flux. This could be the case, when the surface

binding Energy U_s is increased due to the formation of an oxide layer on the target, as this would increase, according to the Thompson formula Eq. 2.4, the energy of the ejected particles, which would lower their collision cross section.

A change of the local emission rate $E(R)$ as explained in section 2.2, can be excluded as explanation for the observed effects, as these effects would be more pronounced at closer distances.

Different scattering potentials for Ar and O₂ should influence all experiments conducted in a reactive atmosphere, and the influence should increase when Ar is subsequently replaced by O₂. As this is not the case, this can also be excluded to cause the observed effects. This is also the case for a change in the scattering behavior of TiO_x or AlO_x clusters compared to single Ti and Al atoms, which should be observable in all experiments.

The influence of the addition of O₂ to the working gas on the nascent angular distribution is well observable. When switching from metallic to reactive mode an increase of R_{min}/R_{max} and thus of β occurs. The change of the discharge voltage can explain part of the trend, but the change of the target composition (and thus the binding energy and other parameters) definitely has an effect.

It should be noted that the change of R_{min}/R_{max} when switching from metallic to reactive mode is in opposite direction when comparing a planar target (R_{min}/R_{max} decreases) with a cylindrical one (where R_{min}/R_{max} increases). This can be explained by the fact that $\Phi(\varphi)$ for these two target types is determined by different parameters. $\Phi(\varphi)$ of a planar target is generally determined by $E(R)$ and gas phase scattering, with $Y(\theta)$ having only little influence. As a change of $E(R)$ can be excluded, a change of $\Phi(\varphi)$ can only be explained by a change in the gas phase transport. $\Phi(\varphi)$ of a cylindrical target on the other hand is generally determined by $Y(\theta)$ and gas phase scattering. When the pd product is low, which was the case, a change in the gas phase transport is of only minor influence on $\Phi(\varphi)$.

An interesting effect that is probably caused by ions can be observed in *figure 6.33* (Ti at 100 mm from a 2" magnetron). When compared to the experiment in pure Ar atmosphere (*figure 6.33a*), the experiments in reactive atmosphere (*figure 6.33b*) exhibit two streams reaching out from the middle. This effect can be observed for all

other experiment of this test series conducted at $z = 100$ mm. This indicates that the ratio ions to neutrals increases for reactive sputtering. For the test series at $z = 50$ mm (with 2" magnetron and Ti as target material) these effects could be observed for all experiments, even those conducted under pure Ar atmosphere.

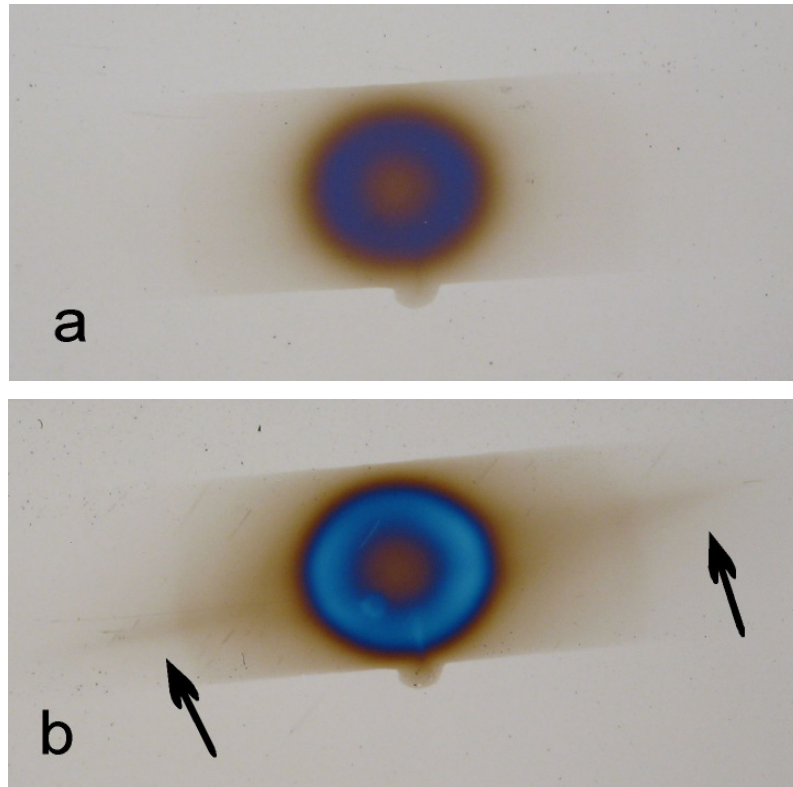


Figure 6.33 Image of two Si substrates coated with TiO_2 inside the MFM. $z = 5$ cm. a) 0.3 Pa Ar; b) 0.3 Pa Ar + 0.1 Pa O_2 . Two streams (indicated by arrows) are good visible, which may not be explained by the usual gas phase transport mechanism of uncharged particles.

7 Conclusions and Outlook

Metal Flux Monitors were constructed, which allow the measurement of the angular distribution of the metal flux at an arbitrary position during magnetron sputtering. These metal flux monitors can be inserted via a load lock system and they are capable of being differentially pumped. The use of these Metal Flux Monitors is not limited to magnetron sputtering, but they can be employed in other PVD processes, e.g. thermal or electron beam evaporation, as well. Additionally, optical methods were developed to determine the thickness profile for metallic and dielectric films with good lateral and vertical resolution at a lateral range of several cm.

A systematic study of the metal flux from different materials (W, Cu, Ti, Al, Mg) and at different magnetron geometries (planar: diameter 2" and 100 mm; cylindrical; rotatable) was carried out with varying parameters (pressure, distance, lateral position) in a pure Ar atmosphere. The comparison of the experimental results with simulations performed by SIMTRA, resulted in good matches, proving that the used models are valid. The angular distribution $\Phi(\varphi)$ of a planar and a rotatable magnetron is generally determined by the shape of the local emission intensity $E(R)$ which is proportional to the shape of the erosion zone. For the cylindrical magnetron, $\Phi(\varphi)$ is generally determined by the nascent angular distribution $Y(\theta)$. Gas phase scattering is blurring $\Phi(\varphi)$ with increasing pd product, with lighter elements being generally more affected by gas phase scattering.

As a parameter suitable for a simple quantification of the angular distribution of the arriving flux the ratio R_{min}/R_{max} , being the ratio of the minimum in the center and the maximum at the racetracks, could be identified. A correlation between this parameter and the amount of gas phase scattering could be observed for planar magnetrons, showing that the shape of the angular distribution of the arriving flux and the amount of gas phase scattering are closely related.

For special target geometry, i.e. a cylindrical magnetron, the shape of the nascent angular distribution, characterized by the parameter β , can be measured directly by comparing the experimentally determined angular distribution of the arriving metal flux with an analytical/numerical model.

In addition, the influence of controlled oxygen addition to the argon atmosphere on the angular distribution of metal fluxes during reactive sputtering was investigated. To investigate the influence of oxygen, two different methods were used to change the working gas composition. With a constant total pressure (Ar replaced subsequently by O₂, called constant p_{tot} mode), the effect of high oxygen partial pressures on $\Phi(\varphi)$ was investigated. With a constant Ar pressure (O₂ added to Ar, called constant p_{Ar} mode), the changes of $\Phi(\varphi)$ close to the point where the deposition process switches from metallic to reactive mode were investigated.

In constant p_{tot} mode (conducted with Al and Ti for different planar magnetrons) the behavior of R_{min}/R_{max} with increasing p_{O_2}/p_{tot} exhibits a similar behavior for most experiments. When switching from metallic to reactive mode R_{min}/R_{max} decreases distinctly. A further replacement of Ar by O₂ slightly increases R_{min}/R_{max} again. This could be interpreted as a distinct change when switching from metallic to reactive mode, while the further replacement of Ar by O₂ has only little effect.

The results of the experiments conducted under p_{Ar} mode (conducted with Ti for a planar magnetron and Al for a rotatable magnetron) also showed a coherent behavior. As soon as the deposition process switches from metallic to reactive mode a decrease in R_{min}/R_{max} occurs, although it should increase due to the increased total pressure. This effect is even more pronounced at larger distances ($z = 100$ mm). Further increase of the p_{O_2} increases R_{min}/R_{max} again. As the effect is more pronounced at a higher pd product, its origins will be in the gas phase transport.

The most probable explanation would be an increase of the mean energy of the sputtered particles due to an increase of the surface binding energy U_s of the oxidized target. Higher particle energies would cause a smaller collisional cross section, thus decreasing the influence of gas phase scattering on $\Phi(\varphi)$, which would explain a decrease of R_{min}/R_{max} when switching from metallic to reactive mode. As the gas phase transport during reactive magnetron deposition is not well researched today, a further investigation in this topic is suggested by the author. Especially an investigation of the mean energy of the sputtered particles would be interesting to sustain or falsify the assumption made above.

The influence of the addition of O₂ to the working gas on the nascent angular distribution is well observable (experiment conducted with a cylindrical Ti target and

low pd product to reduce influence of gas phase scattering). When switching from metallic to reactive mode an increase of R_{min}/R_{max} and thus of β occurs. The change of the discharge voltage can explain part of the trend, but the change of the target composition (and thus the binding energy and other parameters) definitely has an effect. It should be noted, that an increase of U_s as assumed above would have an opposite effect on the nascent angular distribution. Because of this discrepancy and the fact that the experiments were only conducted with Ti, further research in this topic is needed with e.g. different target materials.

In conclusion, it was shown that with the Metal Flux Monitor a versatile tool to determine the angular distribution of the arriving flux and that simulations with the SIMTRA program are suitable for forecasting the results of metallic sputtering in pure argon atmospheres. Concerning reactive sputtering, certain correlations were observed, but the processes are more complex and further investigations are needed before the effects can be fully explained.

References

- [1] S. Mahieu, P. Ghekiere, G. De Winter, R. De Gryse, D. Depla, O.I., Lebedev, *Sol. State Phenom.* **105** (2005) 447-452
- [2] S. Mahieu, P. Ghekiere, G. De Winter, S. Heirwegh, D. Depla, R. De Gryse, O.I. Lebedev, G. Van Tendeloo, *J. Cryst. Growth* **279** (2005) 100-109
- [3] S. Mahieu, P. Ghekiere, D. Depla, R. De Gryse, *Thin Solid Films* **515** (2006) 1229–1249
- [4] P. Ghekiere, S. Mahieu, R. De Gryse, D. Depla, *Thin Solid Films* **515** (2006) 485–488
- [5] G.K. Kiema, M.J. Colgan, M.J. Brett, *Sol. En. Mat. & Sol. Cells* **85** (2005) 321-331
- [6] Y.S. Song, J.K. Park, T.W. Kim, C.W. Chung, *Thin Solid Films* **467** (2004) p.117-120
- [7] A.F. Dericioglu, A.R. Boccaccini, I. Dlouhy, Y. Kagawa, *Mat. Trans.* **46** (2005) 996-1003
- [8] K. Ellmer *J. Phys. D : Appl. Phys.* **33** (2000) R17-R32
- [9] Y. Wu, J. Du, K.L. Choy, L.L. Hench, J.K Guo, *Thin Solid Films* **472** (2005) p.150
- [10] D.Y. Sung Kim I, M.G. Lee, N.J. Park, B. Yang, J.M. Yang, J.K Ko, *Mat. Sci. Forum* **495** (2005) 1371-1375
- [11] P. Muralt, T. Maeder, L. Sagalowicz, S. Hiboux, S. Scalese, D. Naumovic, R.G. Agostino, N. Xanthopoulos, H.J. Mathieu, L. Patthey, E.L. Bullock, *J. Appl. Phys.* **83(7)** (1998) 3835-3841
- [12] G.J. Fang, D. Li, X. Zhao, *phys. stat. sol. (a)* **200, No. 2**, (2003) 361–368
- [13] Y. Kim, J. Oh, T.G. Kim, B. Park. *Appl. Phys. Lett.* **78(16)** (2001) 2363-2365
- [14] H. Ljungcrantz, M. Oden, L. Hultman, J.E. Greene, J.E. Sundgren, *J. Appl. Phys.* **80(12)** (1996) 6725-6733
- [15] J.E. Greene, J.E. Sundgren, L. Hultman, I. Petrov, D.B. Bergstrom, *Appl. Phys. Lett.* **67** (1995) 2928-2930
- [16] G. Pari, A. Mookerjee, A.K. Bhattacharya *Phys. B* **353** (2004) 192-200
- [17] J. Cai, H. Gong, *J. Appl. Phys.* **98** (2005) 033707
- [18] A.F. Dericioglu, A.R Boccaccini, I. Dlouhy, Y. Kagawa, *Mat. Trans.* **46** (2005) 996-1003
- [19] S. Mahieu, G. Buyle, D. Depla, S. Heirwegh, P. Ghekiere, R. De Gryse, *Nucl. Instr. and Meth. in Phys. Res. B* **243** (2006) 313–319
- [20] C. Eisenmenger-Sittner, A. Bergauer, H. Bangert, W. Bauer, *J. Vac. Sci. Technol.* **A12(2)** (1994) 536-541
- [21] C. Eisenmenger-Sittner, R. Beyerknecht, A. Bergauer, W. Bauer, G. Betz, *J. Vac. Sci. Technol.* **A13(5)** (1995) 2435-2443
- [22] J. A. Thornton, *J. Vac. Sci. Technol.* **11(4)** (1974) 666-670
- [23] G.S. Bales, R. Bruinsma, E. A. Eklund, R. P. U Karunasiri, J. Rudnick, A. Zangwill, *Science* **249** (1990) 264-268
- [24] G. S. Bales, A. Zangwill *J. Vac. Sci. Technol. A* **9 (1)** (1991) 145-149

- [25] M. Pelliccione, T. Karabacak, C. Gaire, G. C. Wang, T. M. Lu, *Phys. Rev. B* **74** (2006) 125420
- [26] K. Robbie, M. J. Brett, *J. Vac. Sci. Technol. A* **15(3)** (1997) 1460-1465
- [27] J. A. Thornton, D. W. Hoffman, *J. Vac. Sci. Technol.* **18(2)** (1981) 203-207
- [28] S. Swan, *J. Vac. Sci. Technol. A* **5 (4)** (1987). 1750-54
- [29] B. Feddes, J. G. C. Wolke, J. A. Jansen, A. M. Vredenberg, *J. Appl. Phys.* **93 (1)** (2003) 662-670
- [30] M. Panjan, R. Cremer, H. G. Fuss, P. Panjan, M. Cekada, *Vacuum* **84** (2010) 45–48
- [31] K. Van Aeken, S. Mahieu, D. Depla, *J. Phys. D: Appl. Phys.* **41** (2008) 205307
- [32] R.F. Bunshah, *Deposition Technologies for Films and Coatings*, (Noyes Publication, New Jersey 1982) 170
- [33] M. J. Goekner; J. A. Goree, T. E. Sheridan, *IEEE Transactions on Plasma Science.* **19(2)** (1991) 301-308
- [34] R. Wendt, K. Ellmer, K. Wiesemann, *J. Appl. Phys.*, **82(5)** (1997) 2115-2122
- [35] S. D. Ekpe, S. K. Dew, *J. Vac. Sci. Technol. A* **20(6)** (2002) 1877-1885
- [36] S. D. Ekpe, S. K. Dew, *J. Vac. Sci. Technol. A* **21(2)** (2003) 476-483
- [37] J. Musschoot, D. Depla, g. Buyle, J. Haemers, R. De Gryse, *J. Phys. D: Appl. Phys.* **39** (2006) 3989–93
- [38] J. Musschoot, D. Depla, g. Buyle, J. Haemers, R. De Gryse, *J. Phys. D: Appl. Phys.*. **D41** (2008) 015209
- [39] P. Sigmund, *Physical Review* **184(2)** (1969) 383-416
- [40] G. K. Wehner, D. Rosenberg, *J. Appl. Phys.* **31** (1960) 177
- [41] J. Roth, J. Bohdansky, W. Ottenberger, *Max-Planck-Institut für Plasmaphysik*, **IPP 9/26**, (1979)
- [42] Y. Yamamura, *Ioniimukogaku*, (Uchida Rokakuho, Tokyo 1995) 239
- [43] H. H. Andersen, B. Stenum, T. Sorensen, H. J. Whitlow, *Nucl. Instr. Methods B* **6** (1985) 459
- [44] Y. Yamamura, K. Murakao, *Nucl. Instr. Methods B* **42** (1989) 175
- [45] Y. Yamamura, C. Mössner, H. Oeschner, *Radiat. Eff.* **105** (1987) 31
- [46] Y. Yamamura, T. Takiguchi, M. Ishida, *Rad. Eff. Def. Solids* **118** (1991) 237
- [47] S.D. Ekpe, L. W. Bezuidenhout, S.K. Dew, *Thin Solid Films* **474** (2005) 330-336
- [48] Y. Yamamura, M. Ishida, *J. Vac. Sci. Technol. A* **13(1)** (1995) 101-112
- [49] Z.L. Zhang, L. Zhang, *Radiation Effects & Defects in Solids* **159** (2004) 301-307
- [50] M. W. Thompson, *Philos. Mag.* **18** (1968) 377
- [51] W. Eckstein, *Nucl. Instrum. Methods* **B18** (1987) 344
- [52] H. L. Bay, W. Berres, E. Hintz, *Nucl. Instr. Methods* **194** (1984) 555

- [53] H. L. Bay, W. Berres, *Nucl. Instr. Methods B* **2** (1984) 606
- [54] H. L. Bay, *Nucl. Instr. Methods B* **18** (1987) 430
- [55] A. Goehlich, N. Niemöller, H. F. Döbele, *J. Nucl. Mater.* **266-269** (1999) 501
- [56] J. Dembowski, H. Oechsner, Y. Yamamura, M. Urbassek, *Nucl. Instr. Methods B* **18** (1987) 464
- [57] R. V. Stuart, G. K. Wehner, *J. Appl. Phys.* **35** (1964) 1819
- [58] H. Oechsner, L. Reichert, *Phys. Lett.* **23** (1966) 90
- [59] H. Oechsner, *Phys. Rev. Lett.* **24** (1970) 583
- [60] R. A. Brizzolara, C. B. Cooper, *Nucl. Instr. Methods B* **43** (1989) 136
- [61] A. Goehlich, D. Gillmann, H. F. Döbele, *Nucl. Instr. Methods B* **164-165** (2000) 834-839
- [62] W. D. Westwood, *J. Vac. Sci. Technol.* **15(1)** (1978) 1-9
- [63] A. Gras-Marti, J. A. Valles-Abarca *J. Appl. Phys.* **54(2)** (1983) 1071-75
- [64] L.T. Ball, I. S. Falconer, D.R. McKenzie, J. M. Smelt *J. Appl. Phys.* **59(3)** (1986) 720-724
- [65] G. M. Turner, I. S. Falconer, B. W. James, D. R. McKenzie, *J. Appl. Phys.* **65(9)** (1989) 3671-79
- [66] A. M. Myers, J. R. Doyle, D. N. Ruzic, *J. Appl. Phys.* **72(7)** (1992) 3064-71
- [67] T. P. Drüsedau, T. Bock, T. M. John, F. Klabunde, W. Eckstein, *J. Vac. Sci. Technol. A* **17(5)** (1999) 2896-2905
- [68] S. M. Rosnagel, *IEEE, Trans. on Plasma Science* **18(6)** (1990) 878-882
- [69] E. W. McDaniel, *Collisional Phenomena in Ionized Gases*, Wiley series in plasma physics (Wiley, New York, 1964)
- [70] K. Macak, P. Macak, U. Helmersson, *Comput. Phys. Commun.* **120** (1999) 238
- [71] W. Eckstein, *Computer Simulation of Ion–Solid Interactions*, ISBN: 3-540-19057-0, (Springer, Berlin, 1991) 296 pp.
- [72] A. A. Abrahamson, *Phys. Rev.* **178(1)** (1969) 76
- [73] K. T. Kuwata, R. I. Erickson, J. R. Doyle, *Nucl. Instrum. Meth. Phys. Res. B.* **201** (2003) 566
- [74] J. H. Keller, R.G. Simmons, *IBM J. Res. Dev.* **23** (1979) 24
- [75] A. Palmero, H. Rudolph, F. H. P. M. Habraken, *Appl. Phys. Lett.* **89** (2006) 211501
- [76] A. Palmero, H. Rudolph, F. H. P. M. Habraken, *J. Appl. Phys.* **101** (2007) 083307
- [77] S. Berg, T. Nyberg, H. O. Blom, C. Nender, *Handbook of Thin Film Process Technology* (Institute of Physics Publishing, Bristol, UK, 1998)
- [78] S. Berg, T. Nyberg, *Thin Solid Films* **476**, (2005) 215
- [79] S. Berg, H. O. Blom, T. Larsson, C. Nender, *J. Vac. Sci. Technol. A* **5** (1987) 202
- [80] S. Berg, T. Larsson, C. Nender, H. O. Blom, *J. Appl. Phys.* **63** (1988) 887

- [81] H. Bartzsch, P. Frach, *Surf. Coat. Technol.* **142-144** (2001) 192
- [82] V. A. Koss, J. L. Vossen, *J. Vac. Sci. Technol. A: Vac. Surf. Films* **8** (1990) 3791
- [83] H. Ofner, R. Zarwasch, E. Rille, H. K. Pulker, *J. Vac. Sci. Technol. A: Vac. Surf. Films* **9** (1991) 2795
- [84] H. Sekiguchi, T. Murakami, A. Kanzawa, T. Imai, T. Honda, *J. Vac. Sci. Technol. A: Vac. Surf. Films* **14** (1996) 2231
- [85] J. Schulte, G. Sobe, *Thin Solid Films* **324** (1998) 19
- [86] S. Zhu, F. Wang, W. Wu, L. Xin, C. Hu, S. Yang, S. Geng, M. Li, Y. Xiong, K. Chen, *International Journal of Materials and Product Technology* (Inderscience Enterprises, Guilin, China, 2001) 101
- [87] S. Kadlec, J. Musil, J. Vyskocil, *Vacuum* **37** (1987) 729
- [88] T. Nyberg, S. Berg, U. Helmersson, K. Hartig, *Appl. Phys. Lett.* **86** (2005) 164106
- [89] D. Depla, S. Mahieu, *Reactive Sputter Deposition* (Springer-Verlag, Berlin Heidelberg, Germany, 2008) pp 189; ISBN 978-3540766629
- [90] R. Snyders, M. Wautelet, R. Gouttebaron, J.P. Dauchot, M. Hecq, *Thin Solid Films* **423** (2003) 125–130
- [91] R. Snyders, R. Gouttebaron, J. P. Dauchot and M. Hecq, *J. Anal. At. Spectrom.* **18** (2003) 618–623
- [92] R. Snyders, M. Wautelet, R. Gouttebaron, J.P. Dauchot, M. Hecq, *Surface and Coatings Technology* **174 –175** (2003) 1282–1286
- [93] R. Snyders, R. Gouttebaron, J.P. Dauchot, M. Hecq, *Surface & Coatings Technology* **200** (2005) 448–452
- [94] T. Kubart, O. Kappertrz, T. Nyberg, S. Berg, *Thin Solid Films* **515** (2006) 421-424
- [95] T. Kubart, S. Zhao, G. Wingqvist, T. Nyberg, E. Wäckelgard, S. Berg, *Journal of physics: Conference Series* **100** (2008) 082024
- [96] T. Kubart, T. Nyberg, S. Berg, *J. Phys. D: Appl. Phys* **43** (2010) 205204
- [97] T. Kubart, T. Nyberg, A. Pflug, M. Siemers, M. Austgen, D. Koehl, M. Wuttig, S. Berg, *Surf & Coat. Technol.* **204** (2010) 3882-86
- [98] D. Rosen, I. Katardjiev, S. Berg, W. Möller, *Nuc. Instr. and Meth. In Phys Res. B* **228** (2005) 193-197
- [99] W. Möller, D. Güttler, *Journ. of Appl. Phys.* **102** (2007) 094501
- [100] Leroy W P, Mahieu S, Persoons R, Depla D, *Plasma Processes and Polymers* **6(1)** (2009) 342-346
- [101] Leroy W P, Mahieu S, Persoons R, Depla D, *Thin Solid Films* **518(5)** (2009) 1527-1531
- [102] S. Mahieu, D. Depla, *Surf. & Coat. Technol.* **204** (2010) 2085-88
- [103] F. Boydens, S. Mahieu, J. Haemers, D. Depla *Phys. Status Solidi A* **207** (2010) 124-128
- [104] D. Depla, X. Y. Li, S. Mahieu, K. Van Aeken, W. P. Leroy, J. Haemers, R. De Gryse, A. Bogaerts, *Journ. of Appl. Phys.* **107** (2010) 113307

- [105] M. Saraiva, V. Georgieva, S. Mahieu, K. Van Aeken, A. Bogearts, D. Depla, *Journ. of Appl. Phys.* **107** (2010) 034902
- [106] X. W. Zhou, H. N. G. Wadley, *Surf. Sci.* **431** (1999) 58-73
- [107] L. Maissel, R. Glang *Handbook of Thin Film Technology* (McGraw-Hill, New York, 1970) pp 1-21; ISBN 978-0070397422
- [108] K. Jousten, *Wutz Handbuch Vacuumtechnik 8. Auflage* (Vieweg & Sohn Verlag, Wiesbaden, Germany 2004) p. 119
- [109] W. Demtröder, *Experimentalphysik 2, Elektrizität und Optik. 3. Edition* (Springer Verlag, Berlin Heidelberg New York 2006) p. 221
- [110] J. H. Weaver, C. Krafka, D. W. Lynch, E. E. Koch, *Physik Daten / Physics Data 18-1* (Fachinformationszentrum Energie-Physik-Mathematik GmbH Karlsruhe 1981)
- [111] B. Šantić, D. Gracin, K. Juraić, *Applied Optics* **48(22)** (2009) 4430-36
- [112] B. Šantić, *Thin Solid Films* **518(14)** (2010) 3619-24
- [113] *The Stopping and Range of Ions in Matter* (2006), available at <http://www.srim.org/>
- [114] D. Czekaĳ, B. Goranchev, E. K. Hollmann, V. A. Volpyas, A. G. Zaytsev, *Vacuum* **42** (1991) 43
- [115] R. Ramos, G. Cunge, M. Touzeau, N. Sadeghi, *J. Phys. D: Appl. Phys.* **41** (2008) 152003
- [116] A. Goehlich, D. Gillman, H. F. Döbele *Nucl. Instrum. Methods Phys. Res. B* **179** (2001) 351
- [117] Y. Yamamura, *Nucl. Instrum. Methods* **194** (1982) 515
- [118] T. Tondou, *PhD Thesis SUPAERO Engineering School, Toulouse, France* (2005)
- [119] D. Depla, S. Mahieu, *Reactive Sputter Deposition* (Springer-Verlag, Berlin Heidelberg, Germany, 2008) pp 120; ISBN 978-3540766629
- [120] M. Horkel, K. Van Aeken, C. Eisenmenger-Sittner, D. Depla, S. Mahieu W. P. Leroy, *J. Phys. D: Appl. Phys* **43** (2010) 075302

Acknowledgements

First the author deeply acknowledges the financial support from the Institute for the promotion of Innovation by Science and Technology in Flanders (IWT; Contract No. IWT 060030), which enabled to author to conduct the research in this very interesting field. Further the author is deeply grateful for their support and guidance during the thesis of Prof. Eisenmenger-Sittner and Prof. Depla. The author wants to thank the other people involved in the project "Growth of complex oxides" for their good cooperation, especially Koen Van Aeken for providing the Monte Carlo code SIMTRA, and Stijn Mahieu and Wouter Leroy for their help and scientific feedback.

The author further wants to thank the members of the group of Prof. Eisenmenger-Sittner, especially Wolfgang Vollnhofer, Johannes Hell, Harald Mahr, Thomas Kölbl and Michelle Kräuter for their help during the experiments and fruitful discussion about important topics of the thesis, like the analytical simulation. Further the help of Robert Zawrel, Jörg Mathé, Martin Quirchmair, Andreas Eder, Ilgar Beniaminov and Daniel Halwidl is deeply acknowledged.

The author also wants to thank the staff of the workshop of the institute of solid state physics, especially Andreas Lahner, Josef Sicherl, and Friedrich Faszt for the construction of the MFM.

Further the author wants to thank his family and Isabella Pree for the moral support during the thesis.

Appendix

Derivation Vignetting

To convert the thickness profile $T(x)$ on the substrate into the angular flux $\Phi(\varphi)$ of impinging particles at the pinhole site, one has to take into account the geometry of the pinhole. The effective area of the pinhole decreases with increasing angle, an effect called vignetting ($V(\varphi)$) (figure A.1), thus also decreasing the number of passing particles.

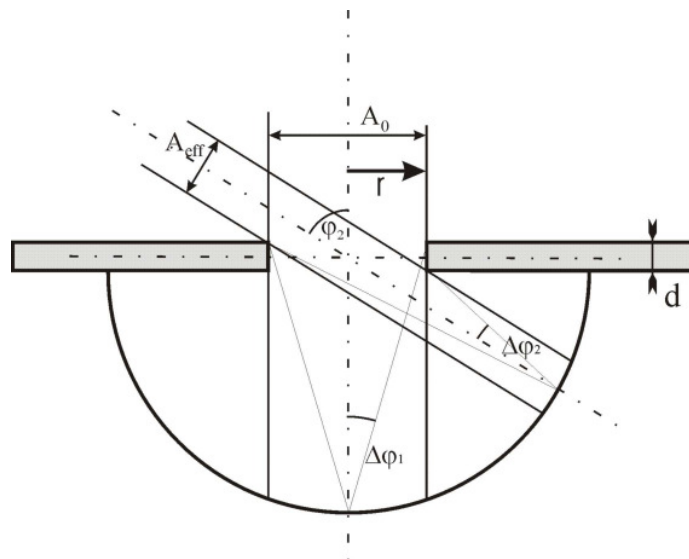


Figure A.1: Vignetting: Two particles are entering the MFM at different angles φ ; one perpendicular ($\varphi_1 = 0^\circ$; aperture A_0 of $r^2\pi$) and the second one at an angle φ_2 with a smaller aperture of A_{eff} . The angular error $\Delta\varphi$ decreases at higher angles because of the decreasing aperture.

For a cylindrical pinhole (length d ; radius r) $V(\varphi)$ is described as the ratio of the effective area A_{eff} seen by the tilted beam to the area of the pinhole A_0 . A_0 can be expressed as $r^2\pi$. The effective area of the cylindrical pinhole approached by a particle with an incident angle φ is sketched in figure A.2.

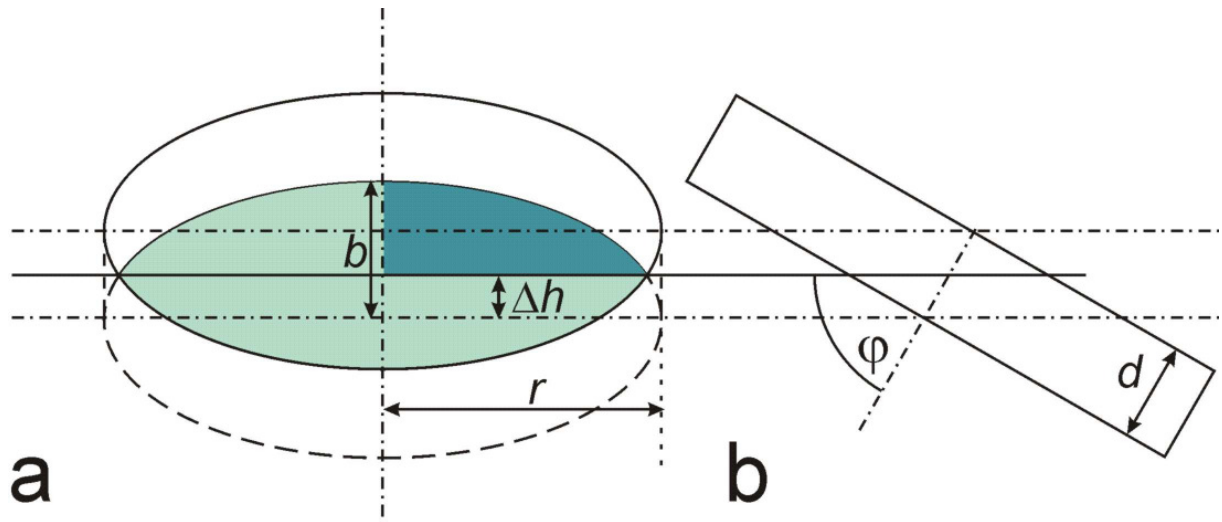


Figure A.2: The effective area A_{eff} of a cylindrical pinhole (length d ; radius r) seen by a particle with an incidence angle of φ (a: top view; b: side view). It can be described as the cross-section (highlighted by light blue) of two ellipses shifted by $2\Delta h = d \cdot \sin \varphi$. The length of the major-axis is r and the length of the minor-axis is $b = r \cdot \cos \varphi$. The effective area consists of 4 equal parts (highlighted by dark blue).

To start the calculation we need the ellipse equation for the given ellipse:

$$\frac{x^2}{r^2} + \frac{y^2}{r^2 \cos^2 \varphi} = 1 \quad \text{Eq. A.1}$$

$$x = \sqrt{r^2 - \frac{y^2}{\cos^2 \varphi}} \quad \text{Eq. A.2}$$

with x being a function of y we can now calculate the area:

$$A_{eff} = 4 \times \int_{\Delta h}^b \int_0^x dx \cdot dy = 4 \times \int_{\Delta h}^b \sqrt{r^2 - \frac{y^2}{\cos^2 \varphi}} dy = 4r \times \int_{\frac{d \sin \varphi}{2}}^{\frac{b}{2}} \sqrt{1 - \frac{y^2}{r^2 \cos^2 \varphi}} \quad \text{Eq. A.3}$$

To solve the integral we have to substitute with:

$$\begin{aligned} \sin \Theta &= \frac{y}{r \cos \varphi} \\ \Theta &= \arcsin\left(\frac{y}{r \cos \varphi}\right) \\ dy &= d\Theta \cdot \cos \Theta \cdot r \cos \varphi \end{aligned} \quad \text{Eq. A.4}$$

Inserting the substitution of Eq. A.4 into Eq. A.3 gives:

$$\begin{aligned}
 A_{eff} &= 4r^2 \cos \varphi \int \sqrt{1 - \sin^2 \Theta} \cdot \cos \Theta \cdot d\Theta = \\
 &= 4r^2 \cos \varphi \int \cos^2 \Theta \cdot d\Theta = 2r^2 \cos \varphi (\sin \Theta \cdot \cos \Theta + \Theta) \Big|_{-\Theta}^{+\Theta}
 \end{aligned}
 \tag{Eq. A.5}$$

Now substituting back Θ by y again gives:

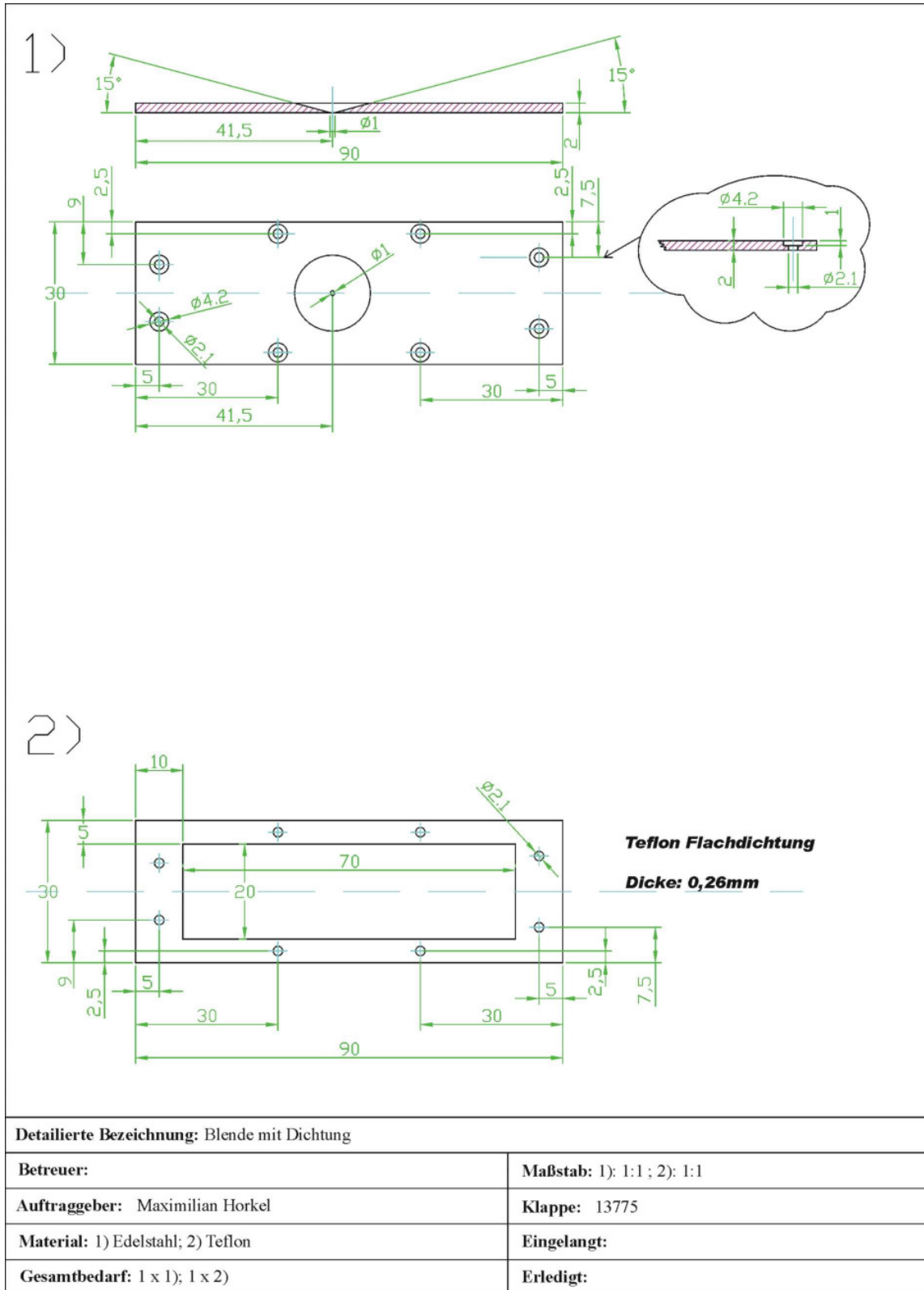
$$\begin{aligned}
 A_{eff} &= 2r^2 \cos \varphi \cdot \left[\frac{y}{r \cos \varphi} \cdot \cos \left(\arcsin \left(\frac{y}{r \cos \varphi} \right) \right) + \arcsin \left(\frac{y}{r \cos \varphi} \right) \right] \Bigg|_{\frac{d \sin \varphi}{2}}^{r \cos \varphi} = \\
 &\text{with } \rightarrow \cos \left(\arcsin \left(\frac{y}{r \cos \varphi} \right) \right) = \sqrt{1 - \frac{y^2}{r^2 \cos^2 \varphi}} \Rightarrow \\
 &= 2r^2 \cos \varphi \left[1 \cdot \sqrt{1-1} + \arcsin(1) - \left(\frac{d}{2r} \tan \varphi \cdot \sqrt{1 - \left(\frac{d \tan \varphi}{2r} \right)^2} + \arcsin \left(\frac{d \tan \varphi}{2r} \right) \right) \right] = \\
 A_{eff} &= 2r^2 \cos \varphi \left[\frac{\pi}{2} - \arcsin \left(\frac{d \tan \varphi}{2r} \right) - \left(\frac{d}{2r} \tan \varphi \cdot \sqrt{1 - \left(\frac{d \tan \varphi}{2r} \right)^2} \right) \right]
 \end{aligned}
 \tag{Eq. A.6}$$

Taking into account that this equation is only valid for the absolute value of φ , $V(\varphi)$ can be expressed as

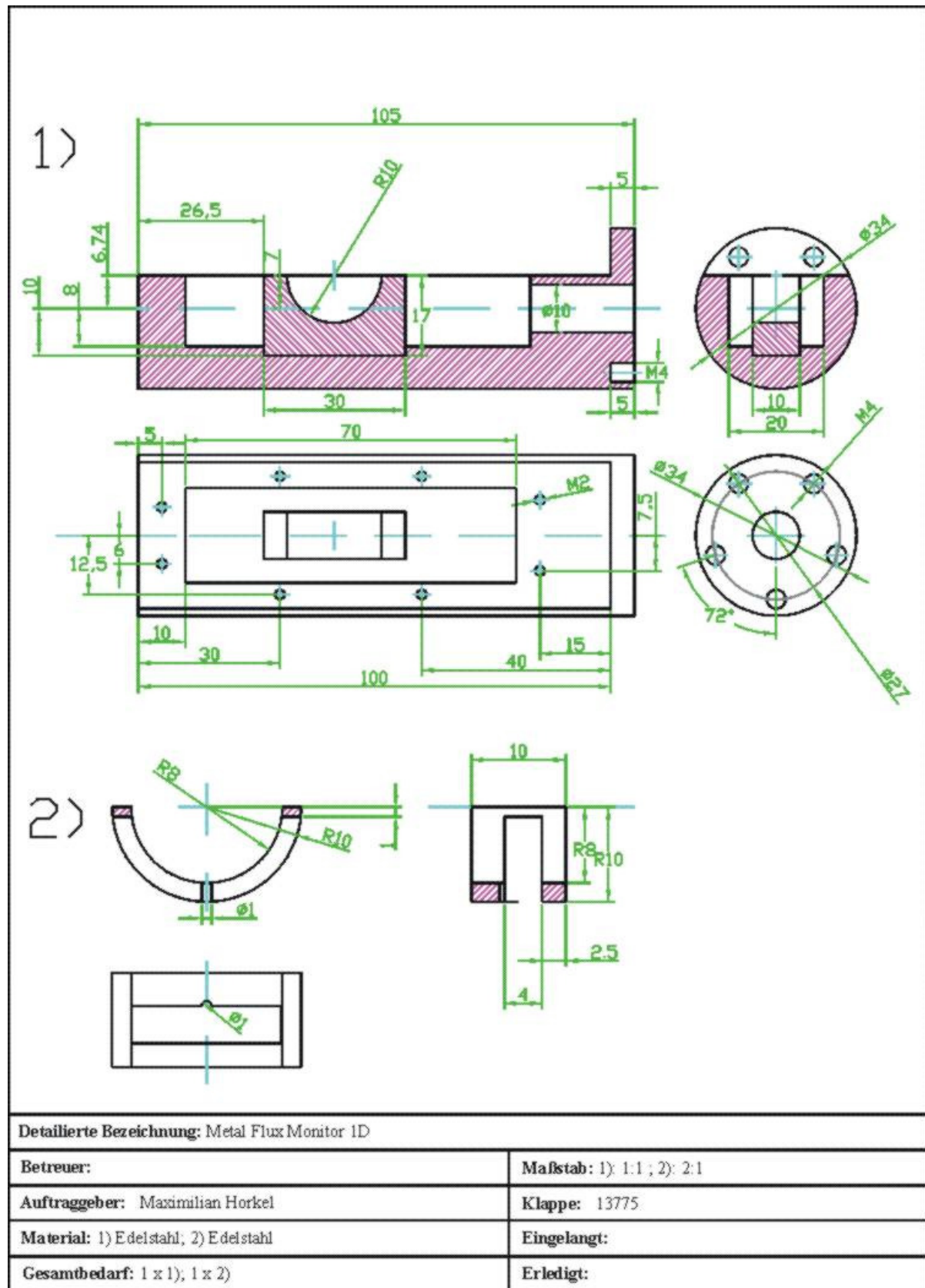
$$V(\varphi) = \frac{A_{eff}}{A_0} = \frac{2 \cos(\varphi)}{\pi} \left[\frac{\pi}{2} - \arcsin \left(\frac{d \tan(|\varphi|)}{2r} \right) - \left(\frac{d \tan(|\varphi|)}{2r} \sqrt{1 - \left(\frac{d \tan(|\varphi|)}{2r} \right)^2} \right) \right]
 \tag{Eq. A.7}$$

Technical Drawings

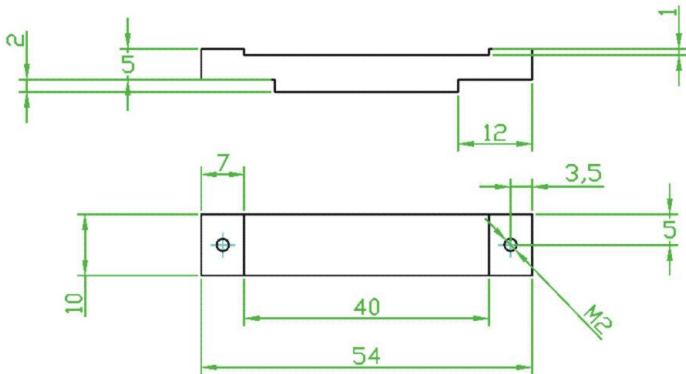
Cover plate with orifice



MFM1D



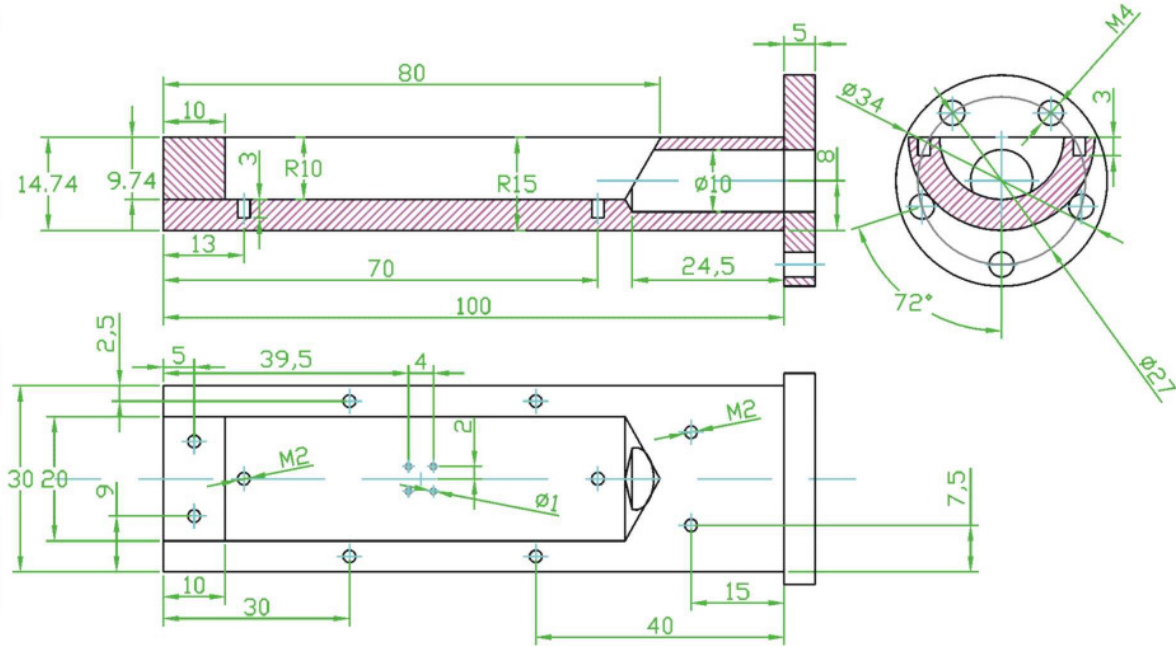
MFMplan



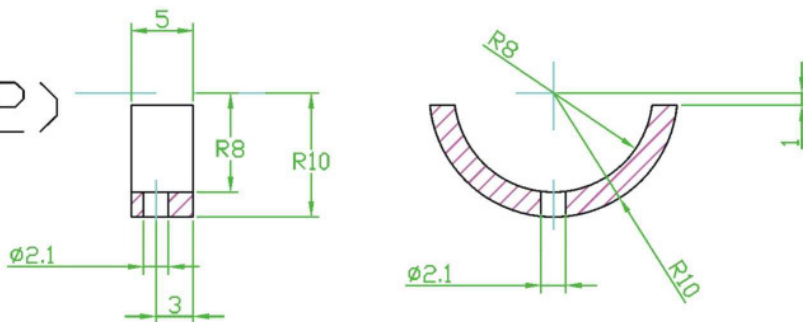
Detaillierte Bezeichnung: Planer Einsatz MFM 1D	
Betreuer:	Maßstab: 1:1
Auftraggeber: Maximilian Horkel	Klappe: 13775
Material: Edelstahl	Eingelangt:
Gesamtbedarf: 1	Erledigt:

MFM2D

1)



2)



Detaillierte Bezeichnung: Metal Flux Monitor 2D

Betreuer:

Maßstab: 1): 1:1 ; 2): 2:1

Auftraggeber: Maximilian Horkel

Klappe: 13775

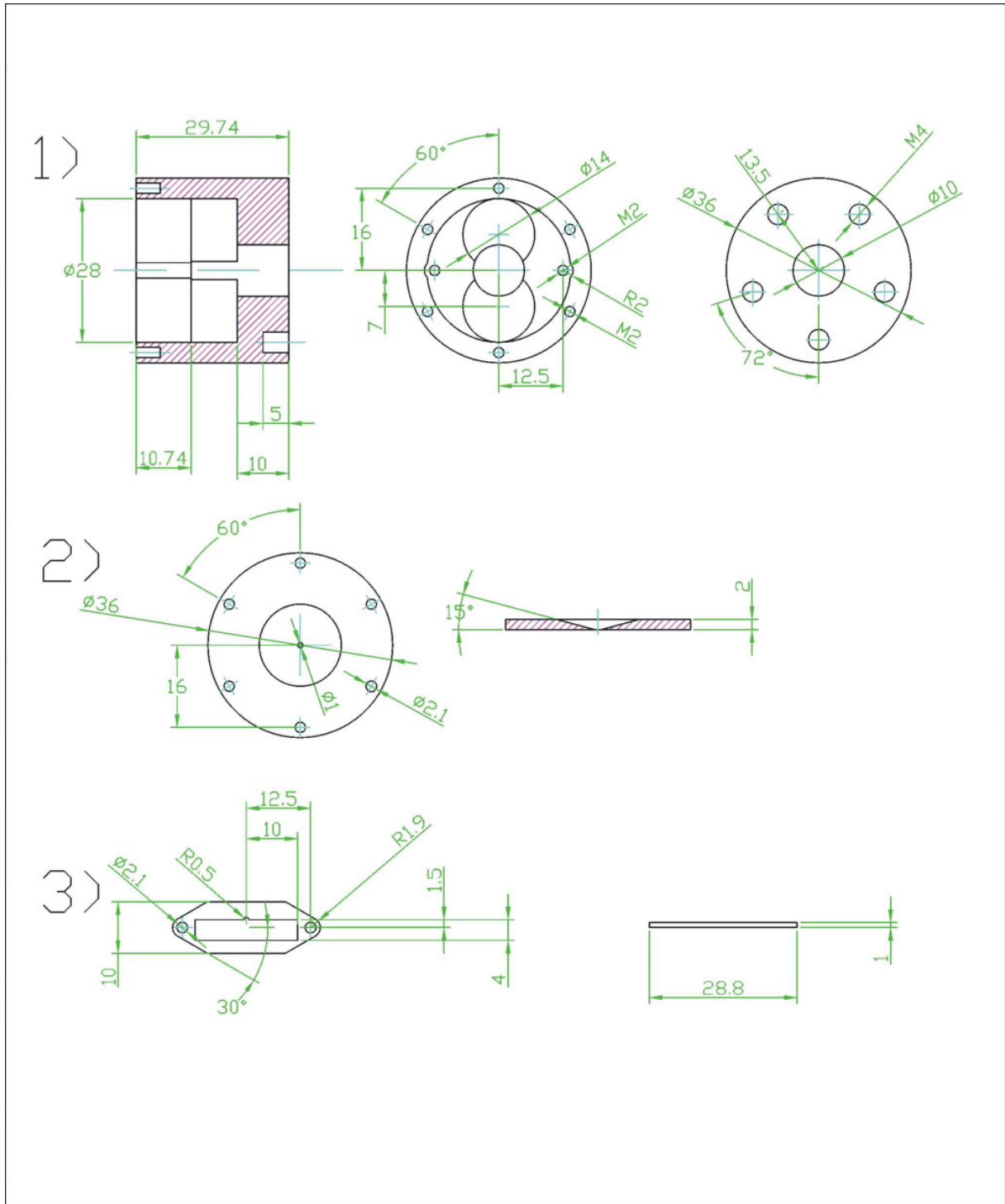
Material: 1) Edelstahl; 2) Edelstahl

Eingelangt:

Gesamtbedarf: 1 x 1); 2 x 2)

Erledigt:

MFMZ



Detaillierte Bezeichnung: 1)MFM Z; 2)Blende Z; 3) Einsatz Z

Betreuer:

Maßstab: 1-3) 1:1

Auftraggeber: Maximilian Horkel

Klappe: 13775

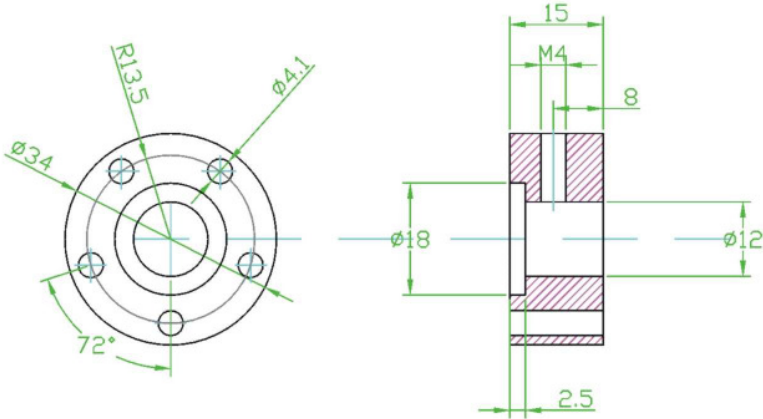
Material: 1-3)Edelstahl

Eingelangt:

Gesamtbedarf: 1-3) 1x

Erledigt:

Connection between MFM and pipe



Detaillierte Bezeichnung: Metal Flux Monitor Flansch abnehmbar

Betreuer:

Maßstab: 1:1

Auftraggeber: Maximilian Horkel

Klappe: 13775

Material: Edelstahl

Eingelangt:

Gesamtbedarf: 1 x 1

Erledigt:

List of experiments

Name	Date	Subs. Mat. MFM type	Targ. Mat.	p_v/p_n [mbar]	p_{spu} [Pa]	I_{spu} [A]	P_{spu} [W]	U_{spu} [V]	t_{spu} [min]	t_{evac}	Notes
MFM1	28.09.07	F/plan	Cu	E-6/3E-6	0.421		200	760	0.5	20min	R[nm/s]=0.927 30nm dicke
MFM2	28.09.07	F/MFM1D	Cu	5E-7/5E-6	0.426		200	763-757	90	1h	x=0
MFM3	01.10.07	F/MFM1D	Cu	5E-7/7E-6	0.431		400	837-847	90	>24h	x=0
MFM4	01.10.07	F/MFM1D	Cu	2E-6/4E-6	0.433		400	828-802	90	20min	x=-2cm
MFM5	02.10.07	F/MFM1D	Cu	1E-6/3E-6	0.43		400	790	90	20min	x=0
MFM6	02.10.07	F/plan	Cu	1E-6/2E-6	0.42		200	677	31s	30min	wie MFM1
MFM7	03.10.07	F/MFM1D	Cu	1E-7/5E-7	0.424		200	672-663	90	12h	wie MFM2
MFM8	03.10.07	F/MFM1D	Cu	1E-7/5E-7	0.85		200	583-573	90	30min	
MFM9	04.10.07	F/MFM1D	Cu	5E-7/1E-6	1.68		200	529	90	30min	
MFM10	08.10.07	F/MFM1D	Cu	1E-7/1E-6	3.5		200	445-455	90	30min	
MFM11	09.10.07	F/MFM2D	Cu	5E-7/1E-6	0.425		200	620-630	105	>24h	
MFM12	10.10.07	F/MFM2D	Cu	1E-7/1E-6	0.87		200	546-565	90	2h	
MFM13	11.10.07	F/MFM2D	Cu	5E-7/5E-6	0.425		200	615	90	12h	
MFM14	12.10.07	F/MFM2D	Cu	1E-6/2E-6	0.86-0.78		200	538-552	90	18h	Magnetron wurde ausgeschaltet
MFM15	12.10.07	F/MFM2D	Cu	1E-6/5E-6	1.61-1.69		200	501	90	45min	
MFM16	16.10.07	F/MFM1D	Cu	1E-6/2E-6	0.5		170	558	90	30min	
MFM17	17.10.07	F/MFM1D	Cu	5E-7/2E-6	0.5		170-160	546-560	90	20min	Wie MFM16 nur ohne Abdeckung
MFM18	17.10.07	F/MFM1D	Cu	5E-7/2E-6	0.3		180	590	90	20h	
MFM19	18.10.07	F/MFM1D	Cu	7E-7/1E-6	0.3		150-160	503-524	90	30min	
MFM20	18.10.07	F/MFM1D	Cu	7E-6/5E-7	0.3		140	480-487			

Name	Date	Subs. Mat. MFM type	Targ. Mat.	p_v/p_n [mbar]	p_{spu} [Pa]	I_{spu} [A]	P_{spu} [W]	U_{spu} [V]	t_{spu} [min]	t_{evac}	Notes
MFM21	19.10.07	F/MFM1D	Cu	5E-7/5E-7	3	0.3	130	430	90	25min	
MFM22	19.10.07	F/MFM1D	Cu	5E-7/	0.52-0.46	0.3	160	512-529	90	20min	Cu von Blende entfernt
MFM23	22.10.07	F/MFM1D	Cu	5E-7/5E-7	0.52-0.46	0.3	160	512-528	90	30min	x=-1.1cm
MFM24	22.10.07	F/MFM1D	Cu	5E-7/1E-7	0.52-0.45	0.3	150-160	508-522	90	20min	x=-2.3cm
MFM25	23.10.07	F/MFM1D	Cu	5E-7/1E-7	0.52-0.45	0.3	150-160	505-522	90	20min	x=-3.5cm
MFM26	23.10.07	F/MFM1D	Cu	5E-7/1E-7	0.53-0.45	0.3	150-160	499-518	90	20min	x=0
MFM27	24.10.07	F/MFM1D	Cu	1E-7/1E-7	0.53-0.45	0.3	150-160	499-516	90	3h	x=0 wie MFM26
MFM28	25.10.07	F/MFM1D	Cu	5E-7/1E-7	0.52-0.45	0.3	150-160	497-513	90	25min	x=+1.1cm
MFM29	25.10.07	F/MFM1D	Cu	1E-7/1E-7	0.52-0.45	0.3	150	494-505	90	1h	x=+2.3cm
MFM30	29.10.07	F/MFM1D	Al	5E-7/1E-7	0.53-0.46	0.3	140-150	490-504	90	20min	x=+3.5cm
MFM31	30.10.07	G/MFM1D	Al	5E-7/1E-7	0.53-0.45	0.3	110-130	384-400	40.5	90min	für profilometer
MFM32	30.10.07	F/MFM1D	Al	1E-6/5E-7	0.53-0.45	0.3	110-120	384-400	10s	50min	5nm
MFM33	30.10.07	F/MFM1D	Al	1E-6/5E-7	0.53-0.45	0.3	110-120	387-400	19s	50min	10nm
MFM34	31.10.07	F/MFM1D	Al	1E-7/5E-7	0.53-0.46	0.3	110-120	385-400	29s	18min	15nm
MFM35	31.10.07	F/MFM1D	Al	7E-7/1E-7	0.53-0.45	0.3	110-120	385-400	38s	25min	20nm
MFM36	31.10.07	F/MFM1D	Al	2E-7/1E-7	0.52-0.45	0.3	110-120	385-400	48s	30min	25nm
MFM37	31.10.07	F/MFM1D	Al	5E-7/1E-7	0.53-0.45	0.3	110-120	384-398	30	90min	
MFM38	05.11.07	F/MFM1D	Al	1E-7/1E-7	0.52-0.45	0.3	110-120	384-400	90	>24h	
MFM39	05.11.07	F/MFM1D	Al	1E-7/5E-7	0.52-0.45	0.6	250-260	420-448	90	20min	
MFM39II	07.11.07	*/plan	Al	1E-7/1E-7	0.52-0.45	0.3	110-120	386-402	10s	140min	MFM39 zusätzlich mit 5nm Al
MFM40	08.11.07	F/MFM1D	Al	1E-7/1E-7	0.52-0.45	0.6	250-270	424-448	90	18h	Blende aufgeweitet
MFM40II	09.11.07	*/plan	Al	1E-6/5E-7	0.52-0.45	0.3	110-120	399-418	10s	110min	MFM40 zusätzlich mit 5nm Al

Name	Date	Subs. Mat. MFM type	Targ. Mat.	p_v/p_n [mbar]	p_{spu} [Pa]	I_{spu} [A]	P_{spu} [W]	U_{spu} [V]	t_{spu} [min]	t_{evac}	Notes
MFM41	13.11.07	F/MFM1D	W	1E-7/1E-7	0.5	0.3	120	401-422	90	22h	
MFM42	14.11.07	F/MFM1D	W	1E-7/1E-7	0.3	0.3	120	417-424	90	16h	
MFM43	14.11.07	F/MFM1D	W	1E-7/1E-7	0.7	0.3	105	361-370	90	90min	
MFM44	15.11.07	F/MFM1D	W	1E-7/1E-7	1	0.3	100	342-352	90	150min	
MFM45	16.11.07	F/MFM1D	W	1E-7/1E-7	3	0.3	80	277-285	90	40min	
MFM46	19.11.07	G/plan	W	5-7/1E-7	0.5	0.3	115	400	40		abgeplatzt
MFM47	21.11.07	G/plan	W	1E-7/1E-7	0.5	0.3	115	381-395	10	>24h	
MFM48	21.11.07	F/plan	W	1E-7/1E-7	0.5	0.3	120	400	13.3s	30min	5nm W
MFM49	21.11.07	F/plan	W	1E-7/1E-7	0.5	0.3	120	400	27.3s	40min	10nm
MFM50	21.11.07	F/plan	W	1E-7/1E-7	0.5	0.3	115	394	41s	90min	15nm
MFM51	21.11.07	F/plan	W	1E-7/1E-7	0.5	0.3	115	395	54.4s	75min	20nm
MFM52	21.11.07	F/plan	W	1E-7/	0.5	0.3	115	397	68s90	40min	25nm
MFM53	10.12.07	F/MFM1D	Cu	1E-7/1E-6	0.5	0.3	140	480	60	>24h	referenz
MFM54	10.12.07	F/MFM1D	Cu	2E-7/1E-6	0.5	0.3	140	477	60	50min	tantal blende
MFM55	14.12.07	G/plan	Cu	1E-7/5E-7	0.5	0.3	140	477	60	18h	
MFM56	21.01.08	F/MFM1D	Cu	1E-7/1E-6	0.5	0.3	140	469	90	150min	diff pumping
MFM57	22.01.08	F/MFM1D	Al	5E-7/	0.5	0.3	110	390	90	3h	dp erosion depth 4.2mm
MFM58	23.01.08	F/MFM1D	Al	1E-7/5E-7	0.5	0.3	260	432	90	17h	dp
MFM59	24.01.08	G/1Dplan	Al	5E-7/1E-7	0.5	0.3	115	394	90	1h	dp
MFM60	29.01.08	G/1Dplan	Al	1E-7/1E-7	0.5	0.3	115	393	90	3h	dp Ti pump
MFM61	30.01.08	Si/1Dplan	Al	1E-7/1E-7	0.5	0.3	120	394	90	75min	
MFM62	05.02.08	Si/1Dplan	Al	1E-7/1E-7	0.5	0.3	120	395	90	2h	

Name	Date	Subs. Mat. MFM type	Targ. Mat.	p_v/p_n [mbar]	p_{spu} [Pa]	I_{spu} [A]	P_{spu} [W]	U_{spu} [V]	t_{spu} [min]	t_{evac} [h]	Notes
MFM63	0602.08	Si/1Dpl	Al	2E-7/1E-7	0.5	0.3	115	393	180	1.25	
MFM64	11.02.08	Si/1Dpl	Al	1E-7/1E-7	0.3	0.3	120	409	90	2	
MFM65	12.02.08	Si/1Dpl	Al	1E-7/1E-7	0.7	0.3	110	377	90	1	erosion depth 4.8mm
MFM66	13.02.08	Si/1Dpl	Al	5E-7/5E-7	1	0.3	110	360	180	2.5	
MFM67	21.02.08	Si/1Dpl	Al	1E-7/5E-7	0.5	0.3	110	385	90	2.5	x=1.1cm
MFM68	22.02.08	Si/1Dpl	Al	5E-7/1E-7	0.5	0.3	110	384	90	3	x=2.3cm
MFM69	25.02.08	Si/1Dpl	Al	5E-7/1E-7	0.5	0.3	110	383	90	0.66	x=3.5cm
MFM70	03.03.08	G/plan	Ti	5E-7/1E-7	0.5	0.3	100	357	1000s	1.5	
MFM71	05.03.08	F/1Dpl	Ti	1E-7/1E-7	0.5	0.3	100	354	90	3.5	
MFM72	06.03.08	Si/1Dpl	Ti	1E-7/1E-7	0.5	0.3	100	352	90	1.5	
MFM73	10.03.08	Si/1Dpl	Ti	1E-7/1E-7	0.5	0.3	100	352	135	2	
MFM74	11.03.08	G/1Dpl	Ti	1E-7/1E-7	0.5	0.3	100	351	135	2.5	
MFM75	12.03.08	G/1Dpl	Ti	1E-7/1E-7	0.5	0.6	230	385	90	4.5	
MFM76	13.03.08	G/1Dpl	Ti	1E-7/1E-7	0.5	0.3	110	345	135	3.5	
MFM77	17.03.08	G/1Dpl	Ti	1E-7/1E-7	0.5	0.6	230	384	90	4.25	
MFM78	18.03.08	G/1Dpl	Ti	1E-7/1E-7	0.5	0.6	220	382	90	3	
MFM79	19.03.08	G/1Dpl	Ti	1E-7/1E-7	0.5	0.6	220	378	90	21.5	
MFM80	20.03.08	G/1Dpl	Ti	1E-7/1E-7	0.5	0.3	100	347	135	20	
MFM81	03.04.08	G/planl	Mg	5E-7/5E-7	0.5	0.3	110	373	2000s	1.75	
MFM82	04.04.08	G/1Dpl	Mg	5E-7/1E-7	0.5	0.3	110	269	90	2	
MFM83	28.04.08	G/1Dpl	Mg	1E-7/1E-7	0.5	0.3	115	361	90	2.5	zu dick
MFM84	29.04.08	Si/1Dpl	Mg	1E-7/1E-7	0.5	0.3	100	350	90	2.75	

Name	Date	Subs. Mat. MFM type	Targ. Mat.	p_v/p_n [mbar]	p_{spu} [Pa]	I_{spu} [A]	P_{spu} [W]	U_{spu} [V]	t_{spu} [min]	t_{evac} [h]	Notes
MFM85	30.04.08	Si/1Dpl	Mg	1E-7/1E-7	0.5	0.3	100	346	45	1.75	
MFM86	05.05.08	Si/1Dpl	Mg	1E-7/1E-7	0.3	0.3	110	372	45	1.5	
MFM87	06.05.08	Si/1Dpl	Mg	1E-7/5E-7	0.1	0.3	110	383	45	1.75	
MFM88	06.05.08	Si/1Dpl	Mg	1E-7/1E-7	0.7	0.3	90	320	60	2	zu dünn
MFM89	07.05.08	Si/1Dpl	Mg	1E-7/1E-7	0.7	0.3	90	315	90	1.25	
MFM90	13.05.08	Si/1Dpl	Mg	1E-7/1E-7	1	0.3	90	295	120	3.75	
MFM91	21.05.08	Si/1Dpl	Mg	1E-7/5E-7	0.5	0.3	100	337	45	2	
MFM92	23.05.08	Si/1Dpl	Mg	5E-7/5E-7	0.5	0.3	100	335	60	1	x=1.1cm
MFM93	26.05.08	Si/1Dpl	Mg	5E-7/5E-7	0.5	0.3	100	332	60	1.25	x=2.3cm
MFM94	28.05.08	Si/1Dpl	Mg	1E-7/1E-7	0.5	0.3	90	328	60	0.75	x=3.5cm
MFM95	08.07.08	G/MFMZ	Cu	1E-7/1E-6	0.5	0.3	170	503	90	1.25	z=10cm
MFM96	09.07.08	G/MFMZ	Cu	1E-7/1E-6	0.5	0.3	160	502	90	2.25	z=10cm
MFM97	10.07.08	G/MFMZ	Cu	1E-7/1E-6	0.5	0.3	160	502	90	2	z=10cm
MFM98	14.07.08	G/MFMZ	Cu	1E-7/	0.5	0.3	160	498	90	3	z=9.5cm
MFM99	15.07.08	G/MFMZ	Cu	1E-7/1E-6	0.5	0.3	160	494	90	1.5	z=9.5cm
MFM100	17.07.08	G/MFMZ	Cu	1E-7/1E-6	0.5	0.3	160	490	45	2	z=11.5cm
MFM101	18.07.08	G/MFMZ	Cu	1E-7/1E-6	0.5	0.3	160	487	30	1.5	z=14cm
MFM102	21.07.08	G/MFMZ	Cu	1E-7/1E-6	0.5	0.3	160	485	90	2	z=9.5cm
MFM103	23.07.08	G/MFMZ	Cu	1E-7/1E-6	0.5	0.3	160	482	45	1	z=75mm
MFM104	23.07.08	G/MFMZ	Cu	1E-7/1E-6	0.5	0.3	160	480	45	1	z=50mm
MFM105	24.07.08	G/MFMZ	Cu	1E-7/1E-6	0.5	0.3	160	477	90	2	z=125mm
MFM106	25.07.08	G/MFMZ	Cu	1E-7/1E-6	0.5	0.3	160	472	90	19	z=150mm

Name	Date	Subs. Mat. MFM type	Targ. Mat.	p_v/p_n [mbar]	p_{spu} [Pa]	I_{spu} [A]	P_{spu} [W]	U_{spu} [V]	t_{spu} [min]	t_{evac} [h]	Notes
MFM107	31.07.08	G/1Dpl	Ti	1E-7/5E-7	0.5	0.3	100	347	90	20	dp keinO2
MFM108	01.08.08	G/1Dpl	Ti	1E-7/1E-7	0.5	0.3	100	343	90	21	wie MFM107
MFM109	04.08.08	Si/1dpl	Ti	5E-7/1E-7	0.5	0.3	100	341	90	2.3	O2 zugeführt
MFM110	05.08.08	Si/1dpl	Ti	1E-7/1E-7	0.5	0.3	100	343	60	2.75	wie 109 nur kürzer
MFM111	11.08.08	Si/1dpl	Ti	5E-7/1E-7	0.3	0.3	100	350	60	2.6	
MFM112	12.08.08	Si/1dpl	Ti	5E-7/1E-7	0.7	0.3	95	330	60	1.5	zu dünn
MFM113	13.08.08	Si/1dpl	Ti	1E-7/1E-7	0.7	0.3	90	327	90	2.9	
MFM114	14.08.08	Si/1dpl	Ti	1E-7/1E-7	1	0.3	90	312	90	1.5	
MFM115	19.08.08	Si/1dpl	Ti	1E-7/1E-7	0.5	0.3	100	333	60	20	
MFM116	20.08.08	Si/1dpl	Ti	1E-7/1E-7	0.5	0.3	100	332	60	16.5	x=1.1cm
MFM117	20.08.08	Si/1dpl	Ti	1E-7/1E-7	0.5	0.3	100	331	60	2	x=2.3cm
MFM118	21.08.08	Si/1dpl	Ti	1E-7/1E-7	0.5	0.3	95	330	60	18	x=3.5cm
MFM119		Si/1dpl	Ti	3E-6/1E-5	0.5	0.9	370	415-386	30		
MFM120		Si/1dpl	Ti	7E-7/3E-6	0.5	0.9	370	382	13		
MFM121		Si/1dpl	Ti	4E-6/	0.676	0.9	420	433	66		
MFM122		Si/1dpl	Ti	5E-7/1E-6	0.665	0.9	350	364	15		
MFM123		Si/1dpl	Ti	5E-7/1E-6	0.67	0.9	410	432	40		FIAr 10.3 sccm FIO2 4.6 sccm
MFM124		Si/1dpl	Ti	5E-7/1E-6	0.677	0.9	410	433	40		FIAr 10.3 sccm FIO2 4.6 sccm
MFM125		Si/1dpl	Ti	5E-7/1E-6	0.677	0.9	410	433	40		FIAr 10.3 sccm FIO2 4.6 sccm
MFM126		Si/1dpl	Ti	5E-7/1E-6	0.67	0.9	340	360	23		
MFM127		Si/1dpl	Ti	5E-7/1E-6	0.67	0.9	340	353	23		
MFM128		Si/1dpl	Ti	5E-7/1E-6	0.67	0.9	330	350	23		

Name	Date	Subs. Mat. MFM type	Targ. Mat.	p_v/p_n [mbar]	p_{spu} [Pa]	I_{spu} [A]	P_{spu} [W]	U_{spu} [V]	t_{spu} [min]	t_{evac} [h]	Notes
MFM129		Si/1dpl	Ti	5E-7/1E-6	0.67	0.9	380	405	50		FIAr 4 sccm FIO2 17 sccm
MFM130		Si/1dpl	Ti	5E-7/1E-6	0.67	0.9	380	406	33		FIAr 4 sccm FIO2 17 sccm
MFM131		Si/1dpl	Ti	5E-7/1E-6	0.67	0.9	380	406	39		FIAr 4 sccm FIO2 17 sccm
MFM132		Si/1dpl	Ti	5E-7/1E-6	0.67	0.9	380	406	39		FIAr 4 sccm FIO2 17 sccm
MFM133		Si/1dpl	Al	5E-7/1E-6	0.67	0.9	420	435	35		
MFM134		Si/1dpl	Al	5E-7/1E-6	0.67	0.9	410	425	30		
MFM135		Si/1dpl	Al	5E-7/1E-6	0.67	0.9	390	415	20		
MFM136		Si/1dpl	Al	5E-7/1E-6	0.67	0.9	390	400	30		
MFM139		Si/1dpl	Al	5E-7/1E-6	0.69	0.9	260	270	90		FIAr 10.1 sccm FIO2 5.2 sccm
MFM140		Si/1dpl	Al	5E-7/1E-6	0.69	0.9	260	270	60		FIAr 10.1 sccm FIO2 5.2 sccm
MFM141		Si/1dpl	Al	5E-7/1E-6	0.69	0.9	260	275	50		FIAr 10.1 sccm FIO2 5.2 sccm
MFM142		Si/1dpl	Al	5E-7/1E-6	0.69	0.9	260	275	50		FIAr 4 sccm FIO2 10.6 sccm
MFM143		Si/1dpl	Al	5E-7/1E-6	0.69	0.9	260	275	50		FIAr 4 sccm FIO2 10.6 sccm
MFM144		Si/1dpl	Al	5E-7/1E-6	0.69	0.9	260	275	50		FIAr 4 sccm FIO2 10.6 sccm
MFM145		Si/1dpl	Al	5E-7/1E-6	0.69	0.9	260	275	50		FIAr 4 sccm FIO2 10.6 sccm
MFM146	17.09.08	Si/1dpl	Al		0.5	0.9	360-580	618-642	30	3	
MFM147	18.09.08	Si/1dpl	Al		0.5	0.9	550	610	15	1.5	
MFM148	18.09.08	Si/1dpl	Al		0.5	0.9	540	600	20	0.6	Abdeckung Kante
MFM149	25.09.08	Si/1dpl	Al		0.66	0.9	490	545	15	2	
MFM150	25.09.08	Si/1dpl	Al		0.66	0.9	490	538	30	0.5	
MFM151	25.09.08	Si/1dpl	Al		0.66	0.9	480	532	30	0.5	Kante Abdecken
MFM152	29.09.08	Si/1dpl	Al	1E-6/5E-6	0.66	0.9	270	297	30	3	pAr 0.5Pa pO2 0.16 Pa

Name	Date	Subs. Mat. MFM type	Targ. Mat.	p_v/p_n [mbar]	p_{spu} [Pa]	I_{spu} [A]	P_{spu} [W]	U_{spu} [V]	t_{spu} [min]	t_{evac} [h]	Notes
MFM153	30.09.08	Si/1dpl	Al	2E-6/5E-6	0.66	0.9	265	300	120	0.6	pAr 0.5Pa pO2 0.16 Pa
MFM154	01.10.08	Si/1dpl	Al	2E-6/1E-6	0.5	0.9	285	311-330	180	0.6	pAr 0.4Pa pO2 0.1 Pa
MFM155	02.10.08	Si/1dpl	Al	1E-6/1E-6	0.5	0.9	290	325	90	1	pAr 0.4Pa pO2 0.1 Pa
MFM156	02.10.08	Si/1dpl	Al	1E-6/1E-6	0.5	0.9	295	330	120	1	pAr 0.4Pa pO2 0.1 Pa
MFM157	03.10.08	Si/1dpl	Al	1E-6/1E-6	0.5	0.9	275	304-320	120	1	pAr 0.3Pa pO2 0.2 Pa
MFM158	06.10.08	Si/1dpl	Al	1E-6/1E-6	0.5	0.9	510	570	20	1.5	pAr 0.5Pa
MFM159	06.10.08	Si/1dpl	Al	1E-6/1E-6	0.5	0.9	510	566	25	0.5	pAr 0.5Pa
MFM160	07.10.08	Si/1dpl	Al	1E-6/1E-6	0.5	0.9	245	270-284	105	0.6	pAr 0.2Pa pO2 0.3 Pa
MFM161	08.10.08	Si/1dpl	Al	1E-6/1E-6	0.5	0.9	255	281-292	150	0.6	pAr 0.2Pa pO2 0.3 Pa
MFM162	09.10.08	Si/1dpl	Al	1E-6/1E-6	0.5	0.9	250	560	35	1,5	pAr 0.5Pa
MFM163	27.11.08										
MFM164	01.12.08	G/MFMZ	Cu	1E-6/	0.3	0.92	300	549	10	0.5	z=50mm
MFM165	01.12.08	G/MFMZ	Cu	1E-6/3E-6	0.3	0.92	300	552	10	1.7	z=100mm
MFM166	09.12.08	G/MFMZ	Cu	1E-6/5E-6	0.3	0.92	300	545	10	0.7	z=50mm
MFM167	10.12.08	G/MFMZ	Cu	1E-6/3E-6	0.3	0.9	290	541	10	0.5	z=50mm
MFM168	10.12.08	G/MFMZ	Cu	1E-6/5E-6	0.3	0.9	290	540	10	0.7	z=50mm
MFM169	10.12.08	G/MFMZ	Cu	1E-6/5E-6	0.5	0.9	290	546	10	0.5	z=50mm
MFM170	10.12.08	G/MFMZ	Cu	1E-6/5E-6	0.7	0.9	290	542	10	0.9	z=50mm
MFM171	10.12.08	G/MFMZ	Cu	1E-6/5E-6	1	0.9	280	526	10	1.75	z=50mm
MFM172	11.12.08	G/MFMZ	Cu	1E-6/5E-6	0.5	0.9	290	549	5	0.9	z=25mm
MFM173	13.01.09	G/MFMZ	Cu	2E-6/5E-6	0.3	0.9	290	540	5	1	z=25mm
MFM174	13.01.08	G/MFMZ	Cu	1E-6/5E-6	0.7	0.9	290	545	5	1.25	z=25mm

Name	Date	Subs. Mat. MFM type	Targ. Mat.	p_v/p_n [mbar]	p_{spu} [Pa]	I_{spu} [A]	P_{spu} [W]	U_{spu} [V]	t_{spu} [min]	t_{evac} [h]	Notes
MFM175	15.01.09	G/MFMZ	Cu	1E-6/5E-6	1	0.9	280	526	5	0.25	z=25cm
MFM176	27.01.09	G/MFMZ	Cu	2E-6/5E-6	0.5	0.9	290	538	10	3	z=100mm
MFM177	28.01.09	G/MFMZ	Cu	2E-6/5E-6	0.3	0.9	280	525	10	1	z=100mm
MFM178	28.01.09	G/MFMZ	Cu	1E-6/2E-6	0.7	0.9	280	531	10	1	z=100mm
MFM179	15.04.09	G/MFMZ	Cu	1E-6/5E-6	1	0.9	270	510	15	2	z=100mm
MFM180	15.04.09	Si/MFMZ	Al	1E-6/	0.3	0.9	540	568-583	30	0.5	z=25cm
MFM181	15.04.09	Si/MFMZ	Al	5E-7/5E-6	0.3	0.9	530	555	10	1	z=25cm wie MFM180
MFM182	17.04.09	Si/MFMZ	Al	1E-6/1E-5	0.3	0.9	540	573	12	0.75	z=25cm
MFM183	17.04.09	Si/MFMZ	Al	1E-6/1E-6	0.3	0.9	530	56	12	1	z=25c; 0.28Pa Ar; 0.02Pa O2
MFM184	20.04.09	Si/MFMZ	Al	5E-7/5E-6	0.3	0.9	330-390	320-350	30	1	z=25cm
MFM185	21.04.09	Si/MFMZ	Al	5E-7/5E-6	0.3	0.9	330		30	0.5	z=25cm: 7sccm O2
MFM186	21.04.09	Si/MFMZ	Al	5E-7/1E-6	0.3	0.9	540	570	15	0.7	z=50mm
MFM187	21.04.09	Si/MFMZ	Al	5E-7/5E-6	0.3	0.9	540	575	15	1	z=50mm; 24.4sccm Ar; 5.5sc O2
MFM188	22.04.09	Si/MFMZ	Al	1E-6/5E-7	0.3	0.9	300-330	326-345	30	4	z=50mm
MFM189	23.04.09	Si/MFMZ	Al	5E-7/1E-6	0.5	0.9	300	300320	30	1	z=50mm; 20%O2
MFM190	23.04.09	Si/MFMZ	Al	1E-7/2E-6	0.5	0.9	300	320	45	0.5	z=50mm wie MFM189
MFM191	27.04.09	Si/MFMZ	Al	5E-7/1E-5	0.5	0.9	520	550	15	0.9	z=50mm; nur Ar
MFM192	28.04.09	Si/MFMZ	Al	5E-7/	0.5	0.9	290	303	45	4	z=50mm; wie MFM190
MFM193	29.04.09	Si/MFMZ	Al	5E-7/1E-6	0.5	0.9	290	308	60	3.5	z=50mm; wie MFM190
MFM194	30.04.09	Si/MFMZ	Al	5E-7/3E-6	0.5	0.9	290	300	90	15	z=50mm; wie MFM190
MFM195	30.04.09	Si/MFMZ	Al	1E-6/5E-6	0.5	0.9	270	274	90	0.45	z=50mm; 60%O2
MFM196	30.04.09	Si/MFMZ	Al	1E-6/	0.5	0.9	500	525	20	0.5	100mm

Name	Date	Subs. Mat. MFM type	Targ. Mat.	p_v/p_n [mbar]	p_{spu} [Pa]	I_{spu} [A]	P_{spu} [W]	U_{spu} [V]	t_{spu} [min]	t_{evac} [h]	Notes
MFM197	04.05.09	Si/MFMZ	Al	2E-6/2E-6	0.5	0.9	200	270	90	4	wie 195
MFM198	04.05.09	Si/MFMZ	Al	2E-6/2E-6	0.5	0.9	480	510	20	0.5	nur Ar 100mm
MFM199	04.05.09	Si/MFMZ	Al	1E-6/	0.5	0.9	285	300	90	0.5	100mm; 34.3sccmAr; 8sccmO2
MFM200	09.05.09	Si/MFMZ	Ti(cyl)	3E-6/1E-6	0.5	0.9				1.5	
MFM201	10.05.09	Si/MFMZ	Ti(cyl)	5E-6/3E-6	0.5	0.9	270	300	30	4	z=50mm
MFM202	13.05.09	Si/MFMZ	Ti(cyl)	5E-6/3E-6	0.15	0.9	317	357	1	0.75	z=50mm
MFM203	13.05.09	Si/MFMZ	Ti(cyl)	5E-6/3E-6	0.15	0.9	324	360	90	0.5	z=50mm
MFM204	15.05.09	Si/MFMZ	Ti(cyl)	3E-6/3E-6	0.15	0.9	364	327	120	0.5	z=50mm
MFM205	15.07.09	Si/MFMZ	Ti(cyl)	5E-6/1E-6	0.15	0.9	364	327	90	0.5	z=25mm
MFM206	23.07.09	Si/MFMZ	Ti(cyl)	3E-6/2E-6	0.15	0.9	361	325	90	0.5	z=100mm
MFM207	23.07.09	Si/MFMZ	Ti(cyl)	5E-6/1E-6	0.3	0.9	317	285	120	0.5	z=50mm zu dünn
MFM208	23.07.09	Si/MFMZ	Ti(cyl)	5E-6/1E-6	0.3	0.9	317	285	180	0.5	wie 207
MFM209	24.07.09	Si/MFMZ	Ti(cyl)	5E-6/1E-6	0.31	0.9	321	288	180	0.5	wie 208 +1sccm O2
MFM210	27.07.09	Si/MFMZ	Ti(cyl)	5E-6/2E-6	0.31	0.9	318	286	180	0.5	wie 209
MFM211	28.07.09	Si/MFMZ	Ti(cyl)	5E-6/5E-6	0.36	0.9	321-338	356-376	420	0.75	0.3Pa Ar, +2.5 sccm O2; react
MFM212	04.08.09	Si/MFMZ	Ti(cyl)	3E-7/4E-6	0.36	0.9	273	303	180	0.75	0.36Pa Ar
MFM213	05.08.09	Si/MFMZ	Ti(cyl)	5E-6/4E-6	0.34	0.9	329	369	240	0.5	0.3Pa Ar, +1.8 sccm O2; react
MFM214	06.08.09	Si/MFMZ	Ti(cyl)	3E-6/4E-6	0.31	0.9	290	322	180	1.5	0.3Pa Ar, +1.8 sccm O2; met
MFM215	07.08.09	Si/MFMZ	Ti(cyl)	3E-6/2E-6	0.3	0.9	282	313	180	0.7	0.3Pa Ar, +0.5 sccm O2; met
MFM216	10.08.09	Si/MFMZ	Ti(cyl)	4E-6/2E-6	0.33	0.9	343	380	240	1	0.3Pa Ar, +1 sccm O2; react
MFM217	21.08.09	Si/MFMZ	Ti	3E-6/4E-6	0.3	0.7	321	458	15	1	z= 50mm; nicht mittig
MFM218	21.08.09	Si/MFMZ	Ti	5E-6/3E-6	0.3	0.7	313	446	16	1.25	

Name	Date	Subs. Mat. MFM type	Targ. Mat.	p_v/p_n [mbar]	p_{spu} [Pa]	I_{spu} [A]	P_{spu} [W]	U_{spu} [V]	t_{spu} [min]	t_{evac} [h]	Notes
MFM219	26.08.09	Si/MFMZ	Ti	4E-6/4E-5	0.41	0.7	419	597	15	1	+5sccm O2
MFM220	02.09.09	Si/MFMZ	Ti	4E-6/2E-6	0.3	0.3	120	398	30	0.7	zu dünn
MFM221	03.09.09	Si/MFMZ	Ti	5E-6/3E-5	0.42	0.7	398	568	30	0.7	wie MFM219
MFM222	03.09.09	Si/MFMZ	Ti	2E-6/1E-6	0.42	0.7	309	440	20	1	
MFM223	04.09.09	Si/MFMZ	Ti	3E-6/3E-5	0.51	0.7	374	533	30	1	+8.7sccm O2
MFM224	05.09.09	Si/MFMZ	Ti	2E-6/1E-6	0.5	0.7	312	445	20	1	
MFM225	08.09.09	Si/MFMZ	Ti	3E-6/1E-5	0.33	0.7	340	485	20	0.75	+2.5sccm O2
MFM226	08.09.09	Si/MFMZ	Ti	2E-6/3E-5	0.5	0.7	364	520	45	1.5	+8.7sccm O2
MFM227	10.09.09	Si/MFMZ	Ti	1E-6/1E-6	0.3	0.7	329	470	30	1.5	zu dick
MFM228	11.09.09	Si/MFMZ	Ti	2E-6/2E-5	0.41	0.7	308	525	45	0.75	+5sccm O2
MFM229	11.09.09	Si/MFMZ	Ti	2E-6/3E-6	0.33	0.7	321	458	30	0.75	+2.5sccm O2
MFM230	17.09.09	Si/MFMZ	Ti	3E-6/2E-5	0.51	0.7	343	489	45	0.75	+8.7sccm O2; zu dünn
MFM231	21.09.09	Si/MFMZ	Ti	3E-6/1E-6	0.3	0.7	313	446	20	1	
MFM232	22.09.09	Si/MFMZ	Ti	3E-6/2E-5	0.52	0.7	341	485	60	1	+8.7sccm O2
MFM233	22.09.09	Si/MFMZ	Ti	2E-6/7E-7	0.5	0.7	306	437	25	0.7	
MFM234	23.09.09	Si/MFMZ	Ti	4E-6/1E-6	0.5	0.7	297	424	45	0.5	wie MFM233
MFM235	28.09.09	Si/MFMZ	Ti	3E-6/2E-6	0.3	0.7	292	417	15	0.5	wie MFM218, zu dünn
MFM236	28.09.09	Si/MFMZ	Ti	3E-6/1E-6	0.3	0.7	290	414	20	0.5	wie MFM 235
MFM237	06.10.09	Si/MFMZ	Ti	5E-6/2E-6	0.3	0.7	290	409	25	0.5	wie MFM 236
MFM238	07.10.09	Si/MFMZ	Ti	1E-6/1E-6	0.3	0.7	284	405	25	4	oxid entfernt
MFM239	08.10.09	Si/MFMZ	Ti	2E-6/1E-6	0.3	0.7	282	402	15	1	
MFM240	08.10.09	Si/MFMZ	Ti	3E-6/5E-5	0.39	0.7	352	506	30	0.5	+5 sccm O2

Name	Date	Subs. Mat. MFM type	Targ. Mat.	p_v/p_n [mbar]	p_{spu} [Pa]	I_{spu} [A]	P_{spu} [W]	U_{spu} [V]	t_{spu} [min]	t_{evac} [h]	Notes
MFM241	08.10.09	Si/MFMZ	Ti	1E-6/1E-5	0.34	0.7	287	409	20	1.25	+2.5sccm O2
MFM242	09.10.09	Si/MFMZ	Ti	2E-6/2E-5	0.51	0.7	337	482	25	1.25	+8.7sccm O2
MFM243	12.10.09	Si/MFMZ	Ti	3E-6/1E-6	0.51	0.7	270	386	25	1	
MFM244	14.10.09	Si/MFMZ	Ti	3E-6/2E-5	0.4	0.7	364	520	20	0.75	+5sccm O2
MFM245	canceled										canceled
MFM246	21.10.09	Si/MFMZ	Ti	2E-6/2E-7	0.3	0.7	340	482	20	1.5	frisches target; thermoprobleme

Name Name of the sample
 Date Date of the experiment
 Subs. Mat/MFM type Substrate material/Type of the substrate holder MFM (MFM1D; MFM2D; MFMpl; MFMZ) or planar
 Targ. Mat. Target material
 p_v/p_n [mbar] Base pressure before and after deposition
 p_{spu} [Pa] Deposition pressure
 I_{spu} [A] Deposition current
 P_{spu} [W] Deposition power
 U_{spu} [V] Deposition Voltage
 t_{spu} [min] Deposition time
 t_{evac} [h] Evacuation time
 Notes Additional Notes

Bibliography

Publications in refereed journals

M. HORKEL, H. MAHR, J. HELL, C. EISENMENGER-SITTNER, E. NEUBAUER: Determination of the thickness of metal coatings on granular diamond materials by spatially resolved optical methods.- *Vacuum*, **84 (1)** (2009) 57-60

M HORKEL, K VAN AEKEN, C EISENMENGER-SITTNER, D DEPLA, S MAHIEU AND W P LEROY: Experimental determination and simulation of the angular distribution of the metal flux during magnetron sputter deposition.- *J. Phys. D: Appl. Phys.* **43** (2010) 075302

J. HELL, M. HORKEL, E. NEUBAUER, C. EISENMENGER-SITTNER: Construction and characterization of a sputter deposition system for coating granular materials.- *Vacuum (84)* **4** (2009) 453-457

G. SCHMID, C. EISENMENGER-SITTNER, J. HELL, M. HORKEL, M. KEDING, H. MAHR: Optimization of a container design for depositing uniform metal coatings on glass microspheres by magnetron sputtering.- *Surf. and Coat. Technol.*, **205 (7)** (2010) 1929-1936

Oral presentations

M. HORKEL, H. MAHR, J. HELL, C. EISENMENGER-SITTNER, E. NEUBAUER, Spatially resolved thickness determination of metal and oxide coatings using optical consumer electronic components, *ICTF14 & RSD2008 November 17-20*. 2008 Ghent

M. HORKEL, C. EISENMENGER-SITTNER, M. QUIRCHMAIR, K. VAN AEKEN, D. DEPLA, S. MAHIEU, W. P. LEROY, Determination of the nascent angular distribution of sputtered particles during reactive and non-reactive magnetron sputtering, *IVC-18; August 23-27* 2010; Beijing

Poster presentations

M. HORKEL, C. EISENMENGER-SITTNER, J. MATHÉ, A. EDER, I. BENIAMINOV, R. ZAWREL, Determination of the thickness and the refraction index of dielectric thin films with spatial resolution using consumer optical components, *IVC-18; August 23-27* 2010; Beijing (best poster award)

Curriculum Vitae

Dipl.-Ing. Maximilian HORDEL

Geburtsdatum und Geburtsort

11. Juli 1981 in Wien

Nationalität

Österreich

Berufserfahrung

- 10/2007 – 9/2009 Anstellung als Projektassistent an der TU Wien für das Projekt „Growth of Complex Oxides“
- 10/2008 – 1/2009 Tutor an der TU Wien - Übung: Physik für Elektrotechniker
- 7/2007-9/2007 Werkvertrag: Schichtdickenbestimmung auf Diamantgranular mittels Optischer Transmissionsbestimmung und Rasterelektronenmikroskopie am Institut für Festkörperphysik; TU Wien
- 5/2006-6/2007 Diplomarbeit: Anwendung von Beschichtungstechnologien zur Produktinnovation für Fa. M. Schneider Sicherungs-Systeme GmbH, Wien
- 1/2006-4/2006 Projektarbeit: Patentrecherchen und metallographische Probenuntersuchungen für Fa. M. Schneider Sicherungs-Systeme GmbH, Wien

Akademische Laufbahn

- Seit 10/2007 Dissertation über Wachstum komplexer Oxide am Institut für Festkörperphysik; Arbeitsgruppe „Dünne Schichten“ unter Prof. C. Eisenmenger-Sittner, in internationaler Zusammenarbeit mit der Universität Gent, Belgien, finanziert vom IWT Flandern (einem belgischen Forschungsförderungsfond).
- 10/2000 – 6/2007 Diplomstudium der Technischen Physik an der Technischen Universität Wien
Abschluss des Studiums, Akademischer Titel: Dipl. Ing.
Diplomarbeit „Optimierung von Schmelzleitern in NH-Sicherungen mittels Zwischenschichten“, durchgeführt am Institut für Festkörperphysik, TU Wien, Prof. C. Eisenmenger-Sittner, in Zusammenarbeit mit Fa. M. Schneider Sicherungs-Systeme GmbH, Wien

Schulbildung

- 6/1999 Matura
- 1991-1999 Realgymnasium „BRG1 Stubenbastei“, Wien
- 1989-1991 Evangelische Volksschule Karlsplatz, Wien
- 1988-1989 Volksschule Stubenbastei, Wien
- 1987-1988 Volksschule: Privatunterricht in Sumatra, Indonesien